The Nucleus of the Sagittarius Dwarf Spheroidal Galaxy: M54

Mayte Alfaro Cuello
Max-Planck-Institut für Astronomie

Heidelberg 2019

Dissertation in Astronomy
submitted to the
Combined Faculties of the Natural Sciences and Mathematics of the
Ruperto-Carola-University of Heidelberg, Germany,
for the degree of
Doctor of Natural Sciences

put forward by

Mayte Alfaro Cuello
born in La Serena, Chile.
Oral examination: 25 July 2019

The Nucleus of the Sagittarius Dwarf Spheroidal Galaxy: M54

Mayte Alfaro Cuello
Max-Planck-Institut für Astronomie

Referees: Dr. Nadine Neumayer
Prof. Dr. Hans-Walter Rix

Abstract

Nuclear star clusters are the densest stellar systems in the universe, hosted by galaxies across the entire Hubble sequence, including a high fraction of dwarf galaxies. The most massive, chemically complex globular clusters in the Milky Way exhibit similar characteristics as nuclear star clusters in dwarf galaxies. This raised the idea that these globular clusters are actually former nuclei of galaxies accreted by the Milky Way. In this context, M54 – the nuclear star cluster of the Sagittarius dwarf spheroidal galaxy (Sgr dSph) – offers a unique opportunity to understand this presumed direct connection between globular clusters and nuclear star clusters, and low-mass galaxy nucleation. The Sgr dSph is currently being disrupted by the tidal field of the Milky Way, leaving a long stellar stream as evidence of its advanced degree of disruption. M54 still lies at the center of its host, becoming a potential stripped nucleus, and presenting an outstanding example of this class of objects. From its discovery – long before the detection of the Sgr dSph – M54 was classified as a globular cluster, the second most massive in the Milky Way after ω Cen. M54 shows a high spread in iron abundance of its member stars, pointing towards an extended and complex star formation history.

This Thesis presents a large Multi-Unit Spectroscopic Explorer (MUSE) data set covering a region of ~ 2.5 times the effective radius of M54. The single spectra of more than 6 500 member stars extracted from the exceptional data set led to the recovery of the star formation history of this nuclear star cluster through age and metallicity information. This allowed disentangling the presence of – at least – three stellar subpopulations, whose kinematics show clear differences. The chemo-dynamical characterization of these subpopulations suggests that they originated in different star formation events.

This work shows the complexity of M54 which appears to be a nuclear star cluster in a highly disturbed environment rather than a simple globular cluster. The evidence suggests that M54 is the result of the two proposed mechanisms for the formation of nuclear stars clusters, that happen at different stages of M54's evolution: (i) at least two globular clusters are driven to the center of the host and merge to form a single high-mass cluster with a large age and metallicity spread, followed by (ii) in-situ star formation from enriched gas in the nucleus. The unprecedented details of this study help to understand low-mass galaxy nuclei, for which less information is available in contrast to the higher mass regime.

Zusammenfassung

Kernsternhaufen sind die dichtesten Sternsysteme im Universum. Sie sind Teile von Galaxien aller Typen in der Hubble-Sequenz, inklusive einem hohen Anteil an Zwerggalaxien. Die massereichsten, chemisch komplexen Kugelsternhaufen in der Milchstraße zeigen ähnliche Merkmale auf wie Kernsternhaufen in Zwerggalaxien. Daher kam die Idee auf, dass Kugelsternhaufen ehemalige Galaxienkerne sind, welche von der Milchstraße akkretiert wurden. In diesem Zusammenhang bietet M54 – der Kernsterhaufen der elliptischen Zwerggalaxie in Sagittarius (Sgr dSph) – eine einmalige Möglichkeit diesen mutmaßlich direkten Zusammenhang zwischen Kugelsternhaufen und Kernsternhaufen sowie die Kernbildung massearmer Galaxien zu verstehen. Sgr dSph wird gegenwärtig von den Gezeitenkräften der Milchstraße zerrissen. Ein langer Gezeitenstrom von Sternen bezeugt einen fortgeschrittenen Zerreißungsgrad. M54 befindet sich noch immer im Zentrum seiner Heimatgalaxie, sodass dieser möglicherweise ein nackter Kern wird und somit ein außergewöhnliches Beispiel für diese Objektklasse darstellt. Seit seiner Entdeckung, lange bevor Sgr dSph entdeckt wurde, wurde M54 als Kugelsternhaufen klassifiziert und ist nach ω Cen der zweit massereichste Kugelsternhaufen in der Milchstraße. M54 zeigt eine große Spanne im Eisengehalt seiner Sterne, was auf eine ausgedehnte und komplizierte Sternentstehungsgeschichte hindeutet.

Die vorliegende Arbeit präsentiert einen umfangreichen Multi-Unit Spectroscopic Explorer (MUSE) Datensatz, welcher eine Region von ~ 2.5 mal dem Effektivradius von M54 abdeckt. Die einzelnen Spektren von mehr als 6 500 Sternen welche aus dem Datensatz extrahiert wurden führten dazu, dass dessen Entstehungsgeschichte via Alters- und Metallizitätsinformationen nachvollzogen werden konnte. Dies erlaubte die Unterscheidung von mindestens drei stellaren Untergruppen, für welche die kinematischen Eigenschaften klare Unterschiede aufweisen. Die chemo-dynamische Charakterisierung dieser Untergruppen legt nahe, dass diese aus unterschiedlichen Sternentstehungsereignissen hervorgingen.

Diese Arbeit zeigt die Komplexität von M54, welcher eher ein Kernsternhaufen in einer stark gestörten Umgebung als ein einfacher Kugelsternhaufen ist. Die Hinweise legen nahe, dass M54 das Ergebnis der zwei vorgeschlagenen Bildungsmechanismen für Kernsternhaufen ist, welche in verschieden Stadien während der Entwicklung von M54 stattfanden: (i) Mindestens zwei Kugelsternhaufen werden ins Zentrum der Heimatgalaxie getrieben, wo sie zu einem einzigen, massereichen Haufen mit großer Alters- und Metallizitätsverteilung verschmelzen. Diesem folgt (ii) Sternbildung vor Ort aus dem angereicherten Gas im Kern. Die beispiellosen Details dieser Studie helfen dabei massearme Galaxiekerne zu verstehen, für welche im Gegensatz zu massereicheren Bereichen weniger Informationen verfügbar sind.

To the nucleus of my life, my family.

Al núcleo de mi vida, mi familia.

Acknowledgements

These four years at MPIA have been such an enriching experience, not only as a scientist but also as a person. I want to thank my supervisor, Nadine Neumayer, for offering me this opportunity, and for being an amazing supervisor in all aspects. Thank you especially for your time, patience, support and encouragement.

This experience would not have been the same without the members of the "galactic nuclei" group. Many thanks to everyone that has been part of it, especially Nikolay Kacharov (for all of your time and help), Alessandra Mastrobuono-Battisti (for being so amazing), and Iskren Georgiev (for the good discussions and feedback). In addition, I would like to thank my collaborators Anil Seth, Nora Lützgendorf, Torsten Böker, Paolo Bianchini, Sebastian Kamann, Ryan Leaman, Glenn van de Ven, Laura Watkins, and Mariya Lyubenova. Working with all of you has been a wonderful experience! I want to thank the members of the "dynamics" group; it has been great to spend time with you scientifically and personally.

I would like to thank my Thesis committee members Nadine Neumayer, Glenn van de Ven, and Thorsten Lisker, for providing good advice and guidance throughout the Ph.D. Moreover, in this final stage, thanks to Nadine Neumayer and Hans-Walter Rix for agreeing to referee this Thesis, and to the examiners, Eva Grebel and Björn Malte Schäfer.

Being far from home is very difficult, but friends always make the journey easier and better. I cannot mention and thank every awesome person I met during these years as I would need more space for that. However, I want to thank my friends, the old and the new, for your support (even from $\sim 12\,000$ km away), words, and fun times. A special mention to Steffi, who has helped me to make this journey an amazing one. Thanks to every current, former, and honorary member of office 225 (the best office ever!).

Por último pero nunca menos, gracias a mi familia, cuyo infinito e incondicional amor y apoyo ha estado siempre presente. A mis padres, Aldo y María, gracias por apoyarme constantemente en mis decisiones. Gracias a mis hermanos Kathy, Franco, y Juan Pablo, a mis abuelos Mami, Checha, Tata y Luis. Jaime, compañero de vida y aventuras, gracias por siempre estar ahí. Querida familia, gracias por hacerme sentir que nunca importará la distancia entre nosotros.

Contents

Abstract **vii**

Zusammenfassung **ix**

Acknowledgements **xiii**

Contents **xiv**

List of Figures **xix**

List of Tables **xxv**

1 Introduction **1**
- 1.1 Into the Evolution of Galaxies . . . 2
  - 1.1.1 Dwarf Galaxies: The Building Blocks . . . 2
  - 1.1.2 The Role of Minor Mergers/Interactions . . . 3
- 1.2 Globular Clusters . . . 5
  - 1.2.1 Properties of Globular Clusters . . . 5
  - 1.2.2 Multiple Stellar Populations . . . 6
  - 1.2.3 Internal Kinematics of Globular Clusters . . . 7
- 1.3 Nuclear Star Clusters . . . 8
  - 1.3.1 Properties of Nuclear Star Clusters . . . 8
  - 1.3.2 The Coexistence with Massive Black Holes . . . 10
  - 1.3.3 Formation Mechanisms . . . 11
- 1.4 Stripped-off Nuclear Star Clusters . . . 14
  - 1.4.1 Ultracompact Dwarfs . . . 14
  - 1.4.2 High-mass, Metal Complex Globular Clusters . . . 15
- 1.5 A Unique Laboratory: The Nucleated Sagittarius Dwarf Spheroidal Galaxy . . . 16
  - 1.5.1 The Sagittarius Dwarf Spheroidal Galaxy . . . 16
  - 1.5.2 M54 . . . 18
- 1.6 Thesis Outline . . . 21

2 Stellar Population Characterization of M54 **23**
- 2.1 Data . . . 24
  - 2.1.1 Observations and Data Reduction . . . 24

2.1.2 Stellar Spectra Extraction 24
2.2 Analysis 26
2.2.1 Line-of-sight Velocity 26
2.2.2 Sgr dSph NSC Membership 26
2.2.3 Metallicity Estimates 28
2.2.4 Comparison for Multiple Stellar Spectra Measurements 37
2.2.5 Stellar Age Estimates 37
2.2.6 Populations Split by Age and Metallicity 40
2.3 Results 44
2.3.1 Population Analysis 44
2.3.2 Subpopulation Spatial Distributions 46
2.3.3 2D Morphology of Subpopulations 47
2.4 Discussion 48
2.4.1 A Possible Merger Remnant as the Seed of the Sgr dSph NSC 48
2.4.2 In-situ Formation in the Sgr dSph NSC: YMR Subpopulation 49
2.4.3 Sgr dSph Field Stars in Its NSC: IMR Subpopulation 50
2.4.4 The Formation History of the Sgr dSph NSC 51
2.5 Conclusion 52

3 Kinematic Characterization of the Stellar Populations in M54 55
3.1 Analysis 56
3.1.1 Line-of-sight Velocity 56
3.1.2 Rotation and Velocity Dispersion Estimate 56
3.2 Kinematic Extraction 57
3.2.1 Kinematics of all M54 Member Stars 57
3.2.2 Kinematics of M54's Subpopulations 58
3.2.3 V/σ_0 vs. ε 63
3.3 M54 Kinematics with *Gaia DR2* 66
3.3.1 Rotation with *Gaia DR2* 68
3.3.2 Rotation from 3D Kinematics 69
3.4 Comparison with N-body Simulations 71
3.5 Discussion 74
3.5.1 Kinematic Comparison 74
3.5.2 YMR: Evidence of In-situ Formation 76
3.5.3 Kinematic Effects on the OMP Stars by the YMR 76
3.5.4 OMP: Remnant of a Cluster Merger 77
3.5.5 Comparison with ω Cen 78
3.6 Conclusion 79

4 Discrete Dynamical Modeling of M54 81
4.1 Data 83
4.1.1 Stellar Sample 83
4.1.2 Multi-Gaussian Expansion 83
4.2 Maximum-likelihood Analysis 83
4.3 Performing Jeans Models 85
4.4 Discussion and Conclusion 88

5 Conclusions & Outlook 91
5.1 Conclusions 91
5.2 Outlook 94
5.2.1 An IMBH Hosted by M54? 94
5.2.2 Star Formation History from Integrated Spectrum 95
5.2.3 Photo-chemical Evolution Model 97

Bibliography 98

List of Figures

1.1 From left to right: NGC 4395, NGC 1042, NGC 3621, NGC 4178. Examples of bulgeless galaxies hosting an NSC in their center. Figure from Böker (2010). 8

1.2 Galaxy nucleation fraction versus galaxy stellar mass in different cluster environments: Virgo (Côté et al., 2006; Sánchez-Janssen et al., 2018), Fornax (Muñoz et al., 2015) and Coma (den Brok et al., 2014b) clusters as circles, squares, and triangles, respectively. Figure from Sánchez-Janssen et al. (2018) . 9

1.3 Left panel: NSC size vs. host stellar mass relation. Middle panel: NSC size vs. NSC mass relation. Right panel: NSC mass vs. host stellar mass relation. For the three panels red circles and black squares represent late- and early-type galaxies, respectively. Gray circles are for NSCs with uncertainties $> 100\%$. Figures from Georgiev et al. (2016). 10

1.4 Relation between the black hole mass (M_{BH}) and the NSC mass (M_{NC}). Black solid lines show an NSC mass of $3 \times 10^6 M_\odot$ and a ratio of $M_{BH}/M_{NC} = 100$. These lines define a region where the NSC dominates (lower left of both lines), one where the BH dominates the galaxy nuclei (upper left of both lines), an also a transition region (to the right of both lines). Figure from Neumayer & Walcher (2012). 12

1.5 Schematic diagram of the three NSC formation mechanisms. Top: in-situ formation scenario. Middle: GC accretion scenario (or migration scenario). Bottom: accretion of star cluster and gas, followed by in-situ formation. Figure from Guillard et al. (2016). 13

1.6 The masses of UCDs and GCs are plotted against the (predicted) masses of their central black hole. Gray points represent the predictions and upper limits for UCDs from Mieske et al. (2013), which are based on integrated dispersions. Green squares are the measured black holes in GCs ω Cen, G1, and M54 from Lützgendorf et al. (2013). Red triangles show the four known black hole masses in UCDs from Seth et al. (2014); Ahn et al. (2017); Afanasiev et al. (2018). The three black lines mark constant fractions of 1%, 10%, and 20% black hole mass fraction, respectively. Figure from Voggel et al. (2018). 15

1.7 Gaia's sky in colour (Credit: Copyright ESA/Gaia/DPAC). The red rectangle shows the position of the Sgr dSph represented by the isopleth maps from Ibata et al. (1994)*. The zoom in red square shows an image of M54 taken with the *HST* ACS/WFC F814W+F606W. *Image cut from: `http://www.poyntsource.com/Richard/m54_sagittarius_dwarf.htm`. 19

2.1 Color image obtained from the MUSE data of the Sgr dSph NSC, using synthetic i, r, and z filters. The image is a 4×4 mosaic of 16 MUSE pointings, covering $\sim$2.5 $\mathrm{R_{HL}}$ ($\mathrm{R_{HL}} = 0\overset{\prime}{.}82$, Harris 1996, update 2010) of this NSC. The total covered field of view – considering overlaps – is $\sim 3\overset{\prime}{.}5 \times 3\overset{\prime}{.}5$, corresponding to 29 pc×29 pc ($1\overset{\prime}{.}0 = 8.27$ pc). North is up and east is to the left. 25

2.2 Three examples of the fitting performed by ULySS (Koleva et al., 2009) for different types of stars with S/N of 14 (close to minimum of 10), 48, and 100, in the wavelength range of 4701 − 6800Å . Top panels: the best fit is represented in blue, data not considered for the fit in red (both panels), and the multiplicative polynomial in turquoise. Bottom panels: residual of the spectrum fitting (black). Overplotted in dashed and solid green are the mean and the 1σ deviation, respectively. 27

2.3 Top: distribution of the LOS velocities for the extracted stars with S/N$\geq$ 10 from the entire MUSE FOV. Bottom: radius vs. velocity for our stellar sample color-coded by the cluster membership probability ($\mathrm{P_{Membership}}$). We consider as member stars of the Sgr dSph NSC those with probability $\geq 70\%$. 29

2.4 CMD for the total number of extracted spectra with S/N$\geq$ 10. Stellar photometry information in F606W (V) and F814W (I) filters (*HST*/ACS WFC) taken from the M54 catalog (Siegel et al., 2007) of the ACS Survey of Galactic Globular Clusters (Sarajedini et al., 2007). Member stars of the Sgr dSph NSC (probability $\geq 70\%$) are color-coded by the S/N logarithm and nonmembers (probability $< 70\%$) are shown in gray. 30

2.5 Top: metallicity histogram of the member stars of Sgr dSph NSC. Bottom: Radius vs. metallicity plot for the same sample. The stars are color-coded by the uncertainties in the [Fe/H] measurements. 31

2.6 Top panel: CMD for the Sgr dSph NSC members color-coded by metallicity (CMD+metallicity) estimated with ULySS. Bottom panel: Zoom into the TO region. Updated isochrones from the Dartmouth Stellar Evolution Database are overplotted in blue, green, and orange for three stellar populations published by Siegel et al. (2007). 32

2.7 Top: difference in metallicity [Fe/H] between this and other works for stars with $13 \leqslant I \leqslant 17.75$ mag. The 51 red circles show the Δ[Fe/H] between this work and Mucciarelli et al. (2017), and the 36 blue circles are for Carretta et al. (2010b). The mean Δ[Fe/H] between this work and Mucciarelli et al. (2017) is 0.05 ± 0.02 dex, with $\sigma = 0.17$. For Δ[Fe/H] between this work and Carretta et al. (2010b), the mean is 0.15 ± 0.03 dex, with $\sigma = 0.16$. The solid red and blue lines show the mean value of the respective Δ[Fe/H] estimates, while the same color dashed lines show the area confined by the mean error. The dashed black line shows a $\Delta[\mathrm{Fe/H}] = 0$. Bottom: relation between [Fe/H] estimates from this work and those of other works: red circles for Mucciarelli et al. (2017, 51 stars), and blue circles for Carretta et al. (2010b, 36 stars). The gray circles represent the relation of 13 common stars between Carretta et al. (2010b) and Mucciarelli et al. (2017). The eight common stars between the three samples are represented as green circles when comparing this work with Mucciarelli et al. (2017) and green squares when comparing with Carretta et al. (2010b). The dashed black line shows a one-to-one relation. 33

2.8 Fitting examples of Voigt (dashed red line) profiles to the CaII triplet lines for two spectra. Top: Example of high-S/N to noise spectrum ($\mathrm{S/N} = 95$). Bottom: example of low-S/N spectrum ($\mathrm{S/N} = 10$). 35

2.9 Top panel: Equivalent width sum of the three CaII triplet lines versus $V-V_{HB}$. Overplotted in red lines are the metallicity values for the Carrera calibration using the spectral ranges of the CaII triplet lines defined by Armandroff & Zinn (1988). Middle panel: Metallicity histogram of the values obtained with the CaII triplet lines method using the calibration published by Carrera et al. (2013, red) and those obtained performing full spectral fitting using ULySS (Koleva et al., 2009, blue) for the same stellar sample. There are fewer stars in the first method since it is restricted to RGB stars (∼4 000). From left to right the vertical black lines show the average metallicity for the metal-poor and metal-rich stars estimated by Carretta et al. (2010b). Bottom panel: Correlation of the metallicity values obtained with the two methods, for spectra with $S/N > 60$ in blue and $S/N < 60$ in gray. 36

2.10 Top left panel: velocity measurements' correlation of the repeated stars. Middle left panel: correlation between the uncertainties. Bottom left panel: histogram of the difference in the measurements, with $\sigma = 16.25\,\mathrm{km\,s^{-1}}$. Top right panel: shows metallicity measurements' correlation of the repeated stars. Their respective errors' correlation is shown in the middle right panel. Bottom left panel: histogram of the difference in the measurements, with $\sigma = 0.51$ dex. 38

2.11 Top panel: CMD for the Sgr dSph NSC members color-coded by age (CMD+age). Bottom panel: Zoom-in of the TO region. Updated isochrones from the Dartmouth Stellar Evolution Database are overplotted in blue, green, and orange for three stellar populations published by Siegel et al. (2007). 41

2.12 Top: age histogram. Bottom: density plot of the age-metallicity relation. The crosses show the intrinsic spread of the different stellar populations in the Sgr dSph NSC: young metal-rich (YMR) in red, intermediate-age metal-rich (IMR) in orange, and old metal-poor (OMP) in blue. The subpopulations's stellar parameters are summarized in Table 2.2. All the stars included in both panels have age relative errors ⩽40%. The vertical dashed lines show where the probability is equal for the two neighbouring subpopulations. Note: the inclination of the crosses is given by the correlation coefficient obtained from the Gaussian mixture model. 43

2.13 For the two panels: red points represent the YMR subpopulation (2.2 Gyr, $[Fe/H] = -0.04$), orange points for the IMR (4.3 Gyr, $[Fe/H] = -0.29$), and blue points are for the OMP (12.2 Gyr, $[Fe/H] = -1.41$). Gray points show the stars with age relative error greater than 40% or for which age was not estimated. Top panel: CMD. Bottom panel: zoom-in of the top panel showing just the TO region. 45

2.14 Cumulative radial distribution for the three subpopulations for the member stars extracted with $S/N \geqslant 10$ and $I \leqslant 20.5$ mag. YMR subpopulation in shown in red (2.2 Gyr, $[Fe/H] = -0.04$), IMR in orange (4.3 Gyr, $[Fe/H] = -0.29$), and OMP in blue (12.2 Gyr, $[Fe/H] = -1.41$). The magenta dashed line describes a uniform stellar distribution. The vertical black dashed line shows the half-light radius of M54 ($R_{HL} = 0\farcm82$, Harris, 1996, 2010 edition). 47

3.1 Kinematics for all the 6 651 member stars of M54. Top: Velocity map. The median of the best-fit rotation axes at $6.5 \pm 7.5^\circ$ is shown as a solid gray line, and the 1σ uncertainty as dashed gray lines. The dashed circle shows the half-light radius of M54 ($\mathrm{R_{HL}} = 0\overset{\prime}{.}82$, Harris, 1996, 2010 edition). Bottom: Velocity dispersion profile. The median of the best-fit Plummer profiles is shown as a solid gray line, and the $\pm3\sigma$ uncertainty as dashed gray lines. The gray circles show the velocity dispersion estimated in radial bins of $0\overset{\prime}{.}3$. The vertical dashed line shows the half-light radius of M54. 59

3.2 Rotation estimate for all 6 651 M54 member stars. Top: Velocity gradient of M54 with respect to a perpendicular line to the rotation axis. The solid black line shows the median of the best-fit rotation models and the dashed black lines show ±3 times the velocity dispersion. Bottom: Rotation profile. The gray solid line shows the median of the best-fit rotation models, and the dashed gray lines show the 3σ uncertainty. The black circles show the rotation profile obtained for overlapping bins of $0\overset{\prime}{.}6$ along the line perpendicular to the rotation axis. The horizontal and vertical error bars represent the bin size and the uncertainties in the offset of the median velocity, respectively. The vertical dashed lines show the half-light radius of M54 ($\mathrm{R_{HL}} = 0\overset{\prime}{.}82$, Harris, 1996, 2010 edition). 60

3.3 Kinematic extraction for the three subpopulations of M54: YMR in top panels, IMR in middle panels and OMP in bottom panels. Left panels: velocity maps. The gray solid lines show the median of the best-fit rotation axes, and the dashed gray lines the 1σ uncertainty. Dashed circles show the half-light radius of M54 ($\mathrm{R_{HL}} = 0\overset{\prime}{.}82$, Harris, 1996). Right panels: Velocity dispersion profiles. The median of the best-fit Plummer profiles is shown as a solid gray line, and the dashed gray lines show the $\pm3\sigma$ uncertainty. The respective color circles show the velocity dispersion obtained adopting radial bins of $0\overset{\prime}{.}3$. The vertical dashed lines show the half-light radius of M54. 62

3.4 Left panels: Velocity gradients with respect to a line perpendicular to the rotation axis. The solid black line shows the best-fit rotation model, and the dashed black lines correspond to ±3 times the velocity dispersion of the respective population. Right panels: Rotation profiles. The solid gray line represents the median of the best-fit rotation models, and the dashed gray lines represent the $\pm3\sigma$ uncertainty. Respective color circles show the difference between the median velocity and the systemic velocity along the line perpendicular to the rotation axis in overlapping bins of $0\overset{\prime}{.}6$. The horizontal and vertical error bars represent the radial bin size and the uncertainties in the offset of the median velocity, respectively. The vertical dashed lines show the half-light radius of M54 ($\mathrm{R_{HL}} = 0\overset{\prime}{.}82$, Harris, 1996, 2010 edition). 64

3.5 ($V/\sigma_0, \varepsilon$) diagram. We present our estimates for the entire sample of stars (M54), the YMR and OMP subpopulations in gray, red, and blue, respectively. The filled circles show the estimates based on the rotation and ellipticity at the half-light radius ($V_{\mathrm{HL}}/\sigma_0, \varepsilon_{\mathrm{HL}}$), the filled squares, on the rotation amplitude and ellipticity over the entire FOV ($A_{rot}/\sigma_0, \varepsilon$), and the filled triangle two times the rotation amplitude and ellipticity from the Harris (1996, 2010 edition) catalog ($2 \times A_{rot}/\sigma_0, \varepsilon_{\mathrm{H96}}$). The empty symbols show the corrected value for an inclination of 60° using the equation by Cappellari et al. (2007). We include the value from Bellazzini et al. (2008, 2012) for the metal-poor population as a turquoise triangle, whose value was estimated using $2 \times A_{rot}$ and the ellipticity from the Harris (1996, 2010 edition) catalog. For comparison, we include values for GCs from the literature (e.g., Bellazzini et al., 2012; Bianchini et al., 2013; Kacharov et al., 2014) and in green squares the GC sample from Kamann et al. (2018). The solid black line gives the relation for an isotropic oblate rotator presented in Binney (2005). The dashed black lines show the relation for an isotropic oblate rotator and with anisotropy parameters of $\delta = 0.05, 0.1, 0.15, 0.2$, from left to right (Cappellari et al., 2007) 67

3.6 Results of the MCMC sampling of intrinsic 3D rotation of the OMP component (top panel; 108 data points) and of the YMR component (bottom panel; 15 data points). The sampled parameters are the position angle of the rotation axis in the plane of the sky (θ_0), the amplitude of the rotation (A_{rot}), and the inclination angle of the rotation axis with respect to the LOS (i). No rotation is observed for the OMP stars, while clear rotation, mostly in the LOS velocity component, is measured for the YMR stars. The blue lines show the mean of the respective axis parameter. 70

3.7 Result of the fit for the YMR stars shown for the three components of the velocity vector, namely the LOS component, the proper motion component parallel to the rotation axis, and the proper motion component perpendicular to the rotation axis. The red line indicates the result of the MCMC and the grey lines are 100 samples from the chain. 71

3.8 Ellipticity (top panel) and anisotropy parameter β_z (bottom panel) as a function of radius for the whole system M54 (gray), the OMP (blue), and YMR (red) populations at 0 Gyr (dashed lines) and after 2 Gyr of evolution (solid lines) as obtained from the N-body simulation. The angular momentum lost by the YMR population is acquired by the OMP population, that becomes slightly flattened and acquires a small amount of velocity anisotropy along the z axis. Plots are obtained considering the edge-on view of the cluster. 73

3.9 Rotation curves for the whole system M54 (gray), the OMP (blue), and YMR (red) populations at 0 Gyr (dashed lines) and after 2 Gyr of evolution (solid lines) as obtained from the N-body simulation. While the YMR population still rotates significantly, the OMP population has acquired a small ($\sim 1\,\mathrm{km\ s^{-1}}$) rotational speed. The cluster is seen edge-on. 74

3.10 Top: Evolution of the average angular momentum per unit mass perpendicular to the maximum rotation plane for the YMR (red) and OMP (blue) populations. The angular momentum lost by the YMR stars is redistributed among the OMP stars that, consequently, acquire a coherent rotational pattern and settle on a slightly flattened configuration. Bottom: Spatial density profiles of the system, from the N-body simulations, considered as a whole (gray), and of the YMR (red) and OMP (blue) components taken separately as obtained from the N-body simulation. 75

4.1 Surface brightness profile from the MGE model. The blue lines show the individual Gaussian components. The red line represents the total surface brightness, and the black line shows the surface brightness profile from Noyola & Gebhardt (2006). 84

4.2 MCMC distribution for all M54 member stars within a $1'.0$ radius. The scatter plots show the two-dimensional distributions. The histograms represent the one-dimensional distribution for each parameter: mass-to-light ratio and mean velocity. 86

4.3 Top panel: two-dimensional velocity dispersion profile in z predicted by the best model for the sample of all members of M54 within $1'.0$ radius. Bottom panel: one-dimensional velocity dispersion profile. The red solid line shows the velocity dispersion for the predicted model. The blue circles show the velocity dispersion profile estimated in radial bins from the data. The drop in observed velocity dispersion towards the center is due to crowding effects of the stars that limit the spatial resolution of our observations. 87

4.4 MCMC distribution for a subsample of 500 member stars in $1''.0$ radius. The scatter plots show the two-dimensional distributions. The histograms represent the one-dimensional distribution for each parameter: mass-to-light ratio, mean velocity, anisotropy, and rotation. 88

4.5 Top panel: two-dimensional Velocity dispersion profile in z. Bottom panel: one-dimensional velocity dispersion profile from the model for a subsample of 500 member stars of M54 (red line) and the data (blue circles). The drop in observed velocity dispersion towards the center is due to crowding effects of the stars that limit the spatial resolution of our observations. 89

4.6 Top panel: velocity (V_z) map from the best-fitting model for a subsample of 500 member stars of M54 (red line). Bottom panel: rotation profile from the best-fitting model (red line) and from the data (blue circles). 90

5.1 Color images obtained from the MUSE data of M54 using synthetic i, r, and z filters. The images correspond to: the WFM 4×4 mosaic (top panel), the WFM-AO (bottom left panel), and the NFM (bottom right panel). North is up and east is to the left. 96

List of Tables

2.1 Line-of-sight velocity and [Fe/H] spread for repeated stars. 39
2.2 Summary of the stellar Subpopulations in M54. 46

3.1 Summary of the observed properties of M54 and its stellar subpopulations. . . 66
3.2 3D modeling of the intrinsic rotation using the three velocity components. . . . 69

4.1 MGE for M54. 84

“Nothing in life is to be feared, it is only to be understood.
Now is the time to understand more, so that we may fear less.”
– Marie Curie

Chapter 1

Introduction

The zoo of galaxies in the universe covers a vast range of masses and morphologies. Hubble 1936 classified galaxies considering their main characteristics in what we know as the "Hubble sequence", which includes three main galaxy types: elliptical, spiral, and lenticular. Under the belief that this sequence described an evolutionary path, where elliptical galaxies evolve to become spirals, elliptical galaxies were named as "early-type" galaxies and spirals as "late-type" galaxies. Astronomers still keep this naming convention, although the proposed evolutionary sequence is now superseded. Later observations revealed the existence of galaxies with additional different morphology, added to the classification as irregular and dwarf galaxies (e.g., Kormendy & Bender, 2012). Across all types, galaxies consist of three main components in different proportions: stars, gas, and a dark matter halo.

Due to gravitational effects, galaxies are forming structures known as groups, composed of up to 50 galaxies (with 2 to 3 dominating in mass) with diameters of 1 to 3 Mpc and masses of $\sim 10^{12-13} M_{\odot}$. Galaxies are also forming larger structures called clusters consisting of $100 - 1000$ members, diameters of 2 to 10 Mpc and total masses of $\sim 10^{13-15} M_{\odot}$. The Milky Way belongs to the "Local group", which encompasses M31 (Andromeda), M33, the Large and Small Magellanic Cloud (LMC, SMC), and a large number of dwarf galaxies (> 100, McConnachie, 2012) within a diameter of ~ 3 Mpc. The Local group is part of the "Virgo Supercluster", also known as the "Local Supercluster". The fraction of different types of galaxies is not random in clusters but correlates with the density of the environment of the cluster, known as the morphology-density relation (Dressler, 1980). The fraction of spiral galaxies decreases toward higher density environments, while the fraction of lenticular and elliptical galaxies decreases toward lower density environments. Galaxy groups and clusters are dominated by the most massive galaxies, but dwarf galaxies dominate in number above other types. They constitute the base for the assembly of galaxies in the universe: the hierarchical clustering scenario for the formation of large structures (White & Rees, 1978).

1.1 Into the Evolution of Galaxies

In galaxy groups, galaxies are closer to each other than in the field and display low relative velocities (i.e. a low-velocity dispersion), creating an ideal environment for them to interact and/or merge. Galaxy-galaxy interactions drastically affect their structure, e.g., disrupting their disk, severely altering the morphology, changing star formation rates, triggering nuclear activity. Hence, these events are known to strongly affect how galaxies evolve. The degree of the effects on the interacting/merging galaxies is given by their mass ratio. Major mergers occur between two galaxies of a similar mass (mass ratio $\leq 3:1$) and have a strong impact on the involved galaxies. The events involving two galaxies of different masses are known as minor mergers (mass ratio $\geq 4:1$).

Although major mergers are very violent events that effectively shape the evolution of galaxies, they are relatively rare. Minor mergers are expected to occur more often (Fakhouri & Ma, 2008), and are presumed to play an important role in the growth and evolution of galaxies, e.g., contributing to a considerable fraction of galaxy bulges (Hopkins et al., 2010); impacting the stellar kinematics of galaxy disks due to angular momentum redistribution (Di Matteo et al., 2011); contributing to the formation of thick disks (Qu et al., 2011); and triggering star formation episodes (Mihos & Hernquist, 1994).

1.1.1 Dwarf Galaxies: The Building Blocks

Dwarf galaxies belong to the faint end of the luminosity function, with absolute magnitudes fainter than $M_V \sim -18$ mag (Grebel et al., 2003), small sizes and low surface brightnesses. In the last decade, the new instrumental capabilities and the large amount of data released by digital sky surveys triggered an abrupt increase in dwarf galaxy detections inside and outside the Local group. There are over a hundred dwarf galaxies detected in the Local group and its vicinity, and new detections are reported more frequently (e.g., Martin et al., 2015; Drlica-Wagner et al., 2016; Torrealba et al., 2016, 2018a,b; Koposov et al., 2018).

Although all dwarf galaxies belong to the same low-luminosity regime, they show substantial differences in their properties, such as shape, gas content, mass-to-light ratio, and stellar population characteristics reflected in their star formation history (SFH) and also in their color-magnitude diagram (CMD). Dwarf galaxies are classified into two main groups: early-type and late-type dwarf galaxies. Early-type dwarf galaxies are gas-poor, quiescent in star formation, and pressure-supported. This type includes: dwarf Ellipticals (dEs, $-18 < M_V < -14$ mag), dwarf Spheroidals (dSphs, $-14 < M_V < -8$ mag), and Ultra Faint Dwarfs (UFDs, $M_V > -8$ mag, Simon, 2019). Late-type dwarf galaxies are gas-rich, with recent star formation and are (commonly) rotationally-supported. This type includes: dwarf Irregulars (dIrrs), dwarf Spirals (dS), and blue compact dwarf galaxies. For details on the properties of dwarf galaxies in the Local group see Mateo (1998); Tolstoy et al. (2009); McConnachie (2012).

Dwarf galaxies are commonly found orbiting in the halo of larger, more massive galaxies, thus receiving the name of satellites. Some dwarf galaxies around the host can be on a satellite galaxy orbit (a satellite of a satellite, e.g., the Small and Large Magellanic Clouds). The morphology-density relation of dwarf galaxies in the Local Group shows that early-type dwarf galaxies are located in more dense environments, at closer distances to the host, while late-type dwarf galaxies are commonly found at larger galactocentric distances (e.g., Grcevich & Putman, 2009).

The stellar mass and metallicity of galaxies are correlated, with more massive galaxies displaying higher metallicity than the ones with lower masses (Tremonti et al., 2004). In spite of the extremely low luminosity of dwarf galaxies, this correlation is found to be consistent for galaxies in the Local group with stellar masses from $10^{3.5}$ to $10^{12} M_{\odot}$ (Kirby et al., 2013).

As early-type dwarfs, dSphs galaxies have an old stellar population and are depleted of gas. Kinematics studies show that dSph display typical central velocity dispersions of $\sigma \sim 10\,\mathrm{km\,s^{-1}}$. With mass-to-light ratios between $M/L = 10^{1-3}(M/L)_{\odot}$ (McConnachie, 2012), they are the most dark matter-dominated objects known after the UFDs. Under the model of a universe dominated by dark energy and dark matter, the small sizes and dark matter content of dSphs make them key targets to study the structure formation described by the cold dark matter (ΛCDM) model, where galaxies form in a hierarchical assembly (White & Rees, 1978). They provide the opportunity to estimate the density distribution of the dark matter in halos. The properties of the dSph observed in the Local group are also seen in other clusters (e.g., Chiboucas et al., 2009), suggesting they are universal targets for these studies.

1.1.2 The Role of Minor Mergers/Interactions

The life of a dwarf galaxy as a satellite is a turbulent one. They are considerably affected by the tidal field caused by the strong gravitational potential of the host galaxy. As a consequence, dwarf galaxies are affected by dynamical friction, losing angular momentum and kinematic energy producing its orbital decay and migration toward the host gravitational potential. These forces are strong enough to break the gravitational forces of the dwarf galaxy, resulting in the loss of their stellar and/or gas content leaving tidal stellar streams until its total disruption. These effects have been observed through simulations of minor mergers, which found that in the accretion process of a satellite, it can get tidally stripped, leaving stellar streams along their orbits (e.g., Helmi & White, 2001; Mayer et al., 2002). During this process, dwarf galaxies can lose their gas reservoir, quenching their star formation. This, together with the observed morphology-density relation for dwarf galaxies, raised the hypothesis that early-type dwarf galaxies (e.g., dSphs) can be a consequence of strong and constant tidal field effects on late-type dwarf galaxies (e.g., dIrrs, dS). This mechanism is known as "tidal stirring" (Mayer et al., 2001a,b), which resembles the change of gas-rich rotationally-supported late-type dwarf galaxies into gas-poor pressure-supported early-type dwarf galaxies, with ram pressure stripping producing the total gas depletion for gas-rich galaxies close to the host, or partial gas depletion if the galaxy is at larger distances (e.g., Mastropietro et al., 2005; Smith et al., 2010; Mayer et al., 2006, 2007;

Kazantzidis et al., 2011, 2017). This proves whether the environment where dwarf galaxies reside plays an important role in their evolution. Additionally, the metallicity distribution observed in luminous dSphs seems consistent with the quenching of star formation due to their gas stripping by ram pressure effects (Kirby et al., 2013).

In the last two decades, a vast amount of spectroscopic and photometric data from multiple instruments and surveys has become available to the astronomical community, allowing the detection of multiple stellar streams which result from the disruption of satellite galaxies and globular clusters operated by the tidal field of the host. Since dwarf galaxies present relatively high-velocity dispersions and some are dark matter dominated (e.g., ultra-faint dwarf galaxies), these are called dynamically hot streams. For globular clusters, which have low-velocity dispersions, streams are dynamically cold. Several detections of stellar streams from both dwarf galaxies and globular clusters have been reported in the Milky Way (e.g., Leon et al., 2000; Odenkirchen et al., 2001; Newberg et al., 2002; Majewski et al., 2003; Duffau et al., 2006; Belokurov et al., 2006; Grillmair & Dionatos, 2006; Bernard et al., 2016; Mateu et al., 2017; Shipp et al., 2018), and other galaxies (e.g., M31, Ibata et al., 2001a; Zucker et al., 2004). Sometimes streams are detected but it is not possible to constrain their origin, however, from their characteristics it can be presumed (e.g., Grillmair, 2009). In the last few years, *Gaia* data releases (Gaia Collaboration et al., 2016, 2018) have pushed forward the detection of stellar streams. With the copious amount of information on resolved stars in the Milky Way, it is now possible to constrain the stars that actually belong to the streams and to better constrain their characteristics, like proper motions and parallaxes (e.g., Malhan et al., 2018; Torrealba et al., 2018b; Fardal et al., 2019; Koposov et al., 2019; Carballo-Bello, 2019; Ibata et al., 2019b).

Both types of stellar streams can survive for long periods of time, thus becoming a key memory source that can help constrain the accretion history and evolution of the host galaxy. These features are solid proofs of the Galactic potential, and can be used to constrain their depth. These structures are also used to estimate the shape and mass of the dark halo mass distribution of the Milky Way (e.g., Johnston et al., 1999; Ibata et al., 2001b; Eyre & Binney, 2009; Koposov et al., 2010; Varghese et al., 2011; Bovy et al., 2016), and sub-structures of the dark matter (e.g., Ibata et al., 2002; Bonaca et al., 2018). In addition, stellar streams from globular clusters provide valuable information to understand the formation and evolution of globular clusters (e.g., Balbinot & Gieles, 2018).

Even though a large number of streams from dwarf galaxies and globular clusters have been detected, predictions from simulations suggest there is another large fraction to detect. However, there are still some observational limitations, e.g., the obscured regions due to dust.

1.2 Globular Clusters

1.2.1 Properties of Globular Clusters

Globular clusters (GCs) are dense stellar systems made up of 10^{4-6} stars, with masses between $10^{4-6}M_{\odot}$ and half-light radii of 1 to 10 pc. Around 160 GCs have been detected in the Milky Way (e.g., Harris catalog, Harris, 1996) with more expected to be discovered in the obscured dusty regions. Larger galaxies have more GCs, e.g., M31 has ~ 450 GCs (Galleti et al., 2004), and the giant early-type galaxy M87, close to the center of the Virgo cluster, has $\sim 14\,000$ GC candidates (Tamura et al., 2006). The position of GCs in the luminosity-size diagram clearly distinguishes them from more extended objects as dwarf galaxies. For several years, GCs were considered to be simply spherical old stellar clusters, formed in one single star-forming burst in the early times of the universe (> 10 Gyr), with no signatures of rotation and an isotropic velocity distribution. However, in the last years, this view has dramatically changed. New instrument capabilities provided a deeper look into the heart of these objects enabling studies on resolved stellar populations and internal kinematics showing that GCs are more complex than they appeared to be. GCs are among the oldest stellar systems in the universe, relics full of imprints left by physical events that their host has experienced, such as kinematic signatures or different star formation histories. Here resides the importance of GCs, as they provide valuable information from the assembly to the evolution of their host galaxy.

Contrary to dwarf galaxies, GCs show no signs of dark matter and are gas depleted. GCs are composed of old stars of ages > 10 Gyr that are typically metal-poor ($-2.5 < [\mathrm{Fe/H}] < -0.5$), consistent with no recent star formation episodes due to their lack of gas. GCs are not completely spherical, as they present some degree of flattening, and in some cases, the ellipticity varies with radius (e.g., Geyer et al., 1983; Chen & Chen, 2010). The most flattened GCs display an ellipticity of up to ~ 0.2.

Typically in high-mass galaxies, the GC system is characterized by a bi-modal color-distribution with a blue (metal-poor) and a red (metal-rich) GC population (e.g., Kundu & Whitmore, 2001; Peng et al., 2006). This observation suggests two different formation channels: (i) in-situ formation in the host galaxy for the red (metal-rich GCs), and (ii) accretion as a consequence of the disruption of a smaller galaxy for the blue (metal-poor GCs) (e.g., Brodie & Strader, 2006). Our host is not an exception, as this bimodality is also found in the GC system of the Milky Way (Marín-Franch et al., 2009; Forbes & Bridges, 2010; Leaman et al., 2013). This finding is consistent with the large number of streams from disrupted galaxies that provides evidence of its assembly history. Blue GCs are consistent with being formed at early times in low-mass galaxies (likely dwarfs), that the Milky Way has accreted. GCs are thus useful to (i) constrain the accretion and formation history of the host galaxy, and ii) also the formation conditions of the progenitor galaxies, where they formed.

The tidal field of the host galaxy affects the GCs, e.g. in their size. This is observed when the GCs host is being accreted by a larger galaxy. Under the dwarf galaxy tidal field, GCs display a certain size that changes when the tidal field of the larger galaxy becomes stronger. Thus, the GCs adapt, changing their size accordingly to the new field. This occurs in a short period of time, making it difficult to differentiate accreted from in-situ formed GCs by their size (Miholics et al., 2014, 2016).

1.2.2 Multiple Stellar Populations

In the last years, high-resolution spectroscopic and photometric data, e.g., from *HST* as “The ACS Survey of Galactic Globular Clusters” (Sarajedini et al., 2007) in the optical, and “The Hubble Space Telescope UV Legacy Survey of Galactic Globular Clusters” (Piotto et al., 2015) in the ultraviolet, have triggered a series of publications on GCs, revealing new and surprising characteristics of stars in GCs. One of the most relevant observations is that GCs host multiple stellar populations. When referring to GCs, the term “multiple populations” denotes stars with different chemical composition in elements such as C, N, O, He, Na, Mg, and Al. This has a different meaning compared to nuclear star clusters, where the multiple stellar populations show a large spread in both age and metallicity. The populations of GCs are usually referred to as first generation (1G) of stars, if they show a primordial composition, and second generation (2G) of stars, if they are enriched in light elements.

There are different correlations (i.e., positive slope) and anticorrelations (i.e., negative slope) found between different elements in GCs. More massive GCs display higher spread in He (Milone, 2015), with the 2G being more He-enhanced (e.g., Milone et al., 2018). In addition to these chemical differences between the first and second generation of stars, helium enhancement variations have been detected inside the first generation of stars in GCs (Lardo et al., 2018). The Na-O anticorrelation is one of the most common along GCs, but is stronger for the most massive ones (Carretta et al., 2010a). The Al-Mg anticorrelation seems to be related to the mass and metallicity of the GCs, which is more prominent for a cluster with high-mass and metal-poor (e.g., Carretta et al., 2009a,b; Mészáros et al., 2015; Pancino et al., 2017; Mucciarelli et al., 2018). Elemental variations and correlations are not limited to Galactic GCs, they are also observed in extragalactic GCs, for example those in the Large Magellanic Cloud (e.g., Mucciarelli et al., 2009), the Small Magellanic Cloud (e.g., Niederhofer et al., 2017a,b), and M31 (e.g., Colucci et al., 2014; Sakari et al., 2015; Nardiello et al., 2019). The fraction of 2G stars in comparison with the 1G depends on the mass, where for more massive GCs the 2G dominate in number over the 1G (e.g., Milone et al., 2017b).

The need to understand the origin of multiple populations in GCs has motivated studies in younger and less massive clusters to constrain their presence. It seems that multiple populations are not hosted by only old GCs (>6 Gyr, e.g., Niederhofer et al., 2017a,b; Hollyhead et al., 2017, 2018), but also for clusters ~ 2 Gyr old (e.g., Martocchia et al., 2018; Hollyhead et al., 2019). At a mass of $\sim 10^5 M_\odot$, GCs older than >6 Gyr show multiple populations, but no multiple populations are detected for clusters younger than 2 Gyr (e.g., Mucciarelli et al., 2014; Martocchia et al., 2017, 2018). All the mentioned characteristics suggest that the mass and age of GCs seem to determine the presence of multiple populations, and that old GCs and young massive clusters might not form and evolve so differently.

These chemical differences in GC stars pose a challenge to the community to find a viable way to explain the observations since this complexity cannot result from simple stellar evolution processes, thus something else must be playing a role. To date, some scenarios can partially explain these oddities, but there is no conclusive explanation for this GC nature. For a detailed review on multiple populations in GCs and proposed scenarios see Bastian & Lardo (2018).

1.2.3 Internal Kinematics of Globular Clusters

It is clear that GCs are complex systems. Their structure is subject to a combination of processes linked to stellar and dynamical evolution/interaction. Additionally, they evolve under the effects of the tidal field of the host galaxy.

The conception that all GCs were non-rotating systems was recently completely ruled out. A high fraction ($> 50\%$) of Milky Way GCs show clear signatures of rotation (e.g., van de Ven et al., 2006; Bellazzini et al., 2012; Bianchini et al., 2013; Kacharov et al., 2014; Fabricius et al., 2014; Kimmig et al., 2015; Bellini et al., 2017a; Ferraro et al., 2018; Kamann et al., 2018; Bianchini et al., 2018; Sollima et al., 2019), and have some degree of flattening with radial dependence. GCs with high internal central rotation seem to be more flattened than non/low-rotating GCs, suggesting that internal rotation actively affects and defines the shape of GCs (Fabricius et al., 2014; Kamann et al., 2018).

Velocity anisotropy is an important characteristic when studying GC kinematics. At a radius close to the half-light radius, GCs seem to be close to isotropic (e.g., Watkins et al., 2015a), however, they become radially anisotropic at larger radii (e.g., van de Ven et al., 2006; Jindal et al., 2019). This can be the result of certain events such as violent relaxation at early times of the GC formation (Lynden-Bell, 1967). The tidal field of the GCs host galaxy also affects the anisotropy distribution, which is stronger in the outer parts (e.g., Vesperini et al., 2014; Sollima et al., 2015; Tiongco et al., 2016; Zocchi et al., 2016; Jindal et al., 2019). In the case of accreted GCs, the change of the dominant tidal field between the host and the accreting larger galaxy will change the velocity anisotropy of the GCs in a few relaxation times due to the new tidal field (Bianchini et al., 2017).

The two-body interactions lead to a mass-dependency for the kinematics. As part of the thermalization process between two bodies, the massive stars in the GCs lose kinematic energy and sink to the center while the low-mass stars gain kinematic energy migrating to the outer parts of the cluster. This is known as energy equipartition. GCs with an age of more than 20 times their core relaxation time will reach a full equipartition (Bianchini et al., 2016). Even if the equipartition is only partial, two body interactions and equipartition will still result in a mass-dependent migration of stars.

1.3 Nuclear Star Clusters

At the bottom of the potential well of galaxies, we find the most extreme environments where a series of physical events take place, creating a suitable climate for the formation of new structures such as nuclear star clusters (NSCs).

1.3.1 Properties of Nuclear Star Clusters

With densities of $\sim 10^{6-7} M_\odot\,\mathrm{pc}^{-3}$ (Walcher et al., 2005; Misgeld & Hilker, 2011; Norris et al., 2014), NSCs are the densest stellar systems in the universe. They have masses from 10^5 to $10^8 M_\odot$, and half-light radii of about 1-10 pc (Georgiev & Böker, 2014; Georgiev et al., 2016). These characteristics clearly distinguish them from galaxy bulges. Figure 1.1 shows examples of galaxies hosting NSCs that are easily spotted by eye as highly compact and bright objects. NSCs reside at the photometric center of their host (Böker et al., 2002), and coincide with their kinematic center (e.g., in bulgeless galaxies, Neumayer et al., 2011). In the center of the Milky Way, at ~ 8 kpc from the Sun, resides the closest NSC with a dynamical mass of $(2.1 \pm 0.7) \times 10^7 M_\odot$ (Feldmeier-Krause et al., 2017b). The proximity of the Milky Way NSC enables resolved studies of its stellar populations and their characterization, including dynamical modeling for the kinematics of this NSC (e.g., Schödel et al., 2007, 2009, 2014a; Chatzopoulos et al., 2015; Feldmeier et al., 2014; Feldmeier-Krause et al., 2015, 2017a,b).

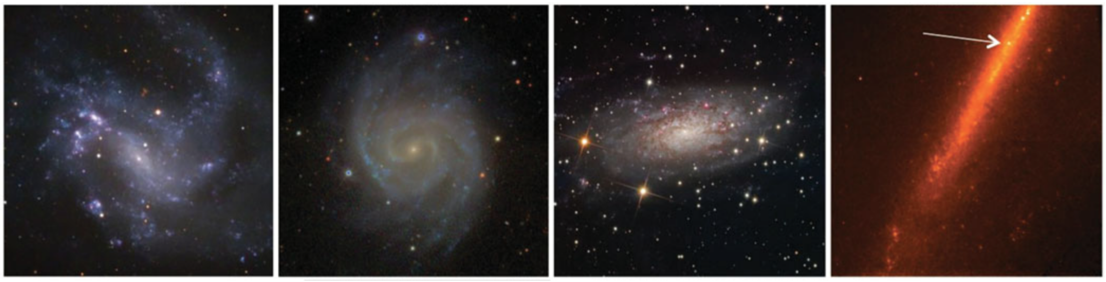

Figure 1.1 From left to right: NGC 4395, NGC 1042, NGC 3621, NGC 4178. Examples of bulgeless galaxies hosting an NSC in their center. Figure from Böker (2010).

High-resolution *Hubble Space Telescope (HST)* imaging of nearby galaxies has revealed that NSCs are present in $\gtrsim$70% of galaxies across the Hubble sequence (Phillips et al., 1996; Carollo et al., 1998; Böker et al., 2002, 2004; Côté et al., 2006; Turner et al., 2012; Georgiev et al., 2009; Georgiev & Böker, 2014). Moreover, the nucleation fraction of galaxies (i.e. fraction of galaxies of a certain mass that host an NSC) seems to be similar for different galaxy cluster environments, e.g., Fornax (Turner et al., 2012; Muñoz et al., 2015), Virgo (Côté et al., 2006; Sánchez-Janssen et al., 2018), and Coma (den Brok et al., 2014b). Figure 1.2 shows the nucleation fraction for galaxies in the stellar mass range of 10^5 to $10^{12} M_\odot$. The nucleation fraction peaks at galaxy masses in the range $10^{8-10} M_\odot$, reaching a fraction over 90% for galaxies with masses of $10^9 M_\odot$ (see also Georgiev et al., 2009; Ordenes-Briceño et al., 2018). The nucleation fraction declines toward lower and higher masses from the peak value. In the low-mass regime, the nucleation

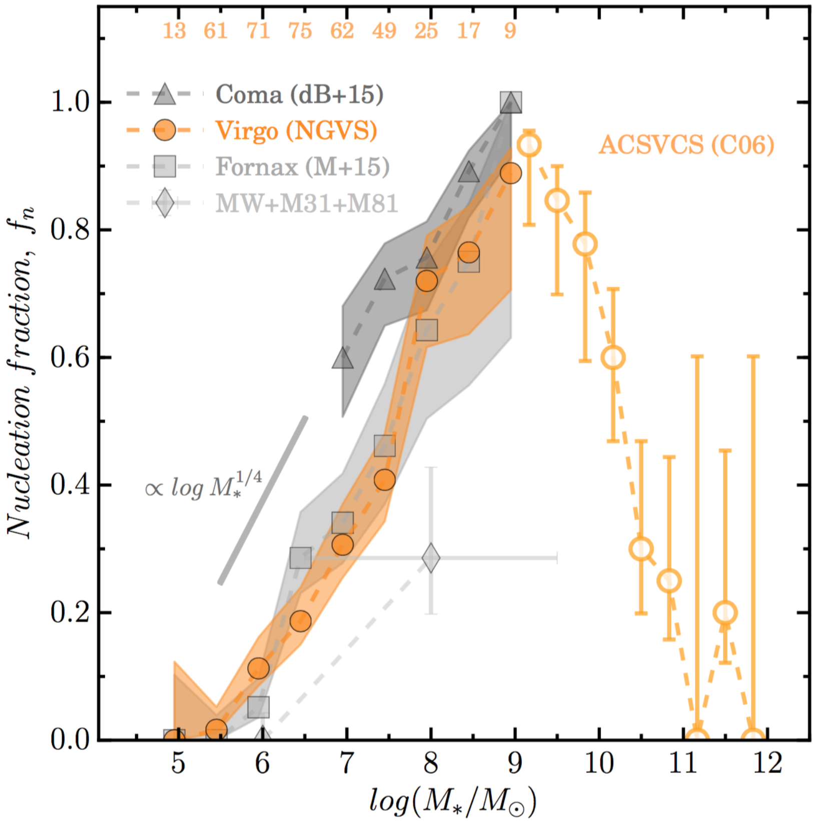

Figure 1.2 Galaxy nucleation fraction versus galaxy stellar mass in different cluster environments: Virgo (Côté et al., 2006; Sánchez-Janssen et al., 2018), Fornax (Muñoz et al., 2015) and Coma (den Brok et al., 2014b) clusters as circles, squares, and triangles, respectively. Figure from Sánchez-Janssen et al. (2018)

fraction is well described as $f_n \propto logM_*^{1/4}$ (Sánchez-Janssen et al., 2018). At masses of $10^5 M_\odot$ and lower, galaxies do not seem to host an NSC. However, the currently known NSC fractions could be considered as lower limits, since due to limits on the observing capabilities there might be a number of NSCs we are not able to detect.

The size of NSCs correlates with their mass, as well as with the stellar mass of the host galaxy (see left and middle panel of Figure 1.3). Observations of a wide sample of NSCs hosted by early- and late-type galaxies show a difference of $\sim 1.5\sigma$ between the size and NSC mass correlation for early- and late-type galaxies. This suggests that the correlation is galaxy-type dependent, hence at a certain NSC mass, the NSCs hosted by late-type galaxies appear more compact than those found in early-type galaxies. This can be attributed to the still ongoing evolution of NSCs in late-type galaxies (Georgiev & Böker, 2014; Georgiev et al., 2016).

The masses of NSCs are found to be $\sim 0.1 \pm 0.2\%$ of the total stellar mass of the host galaxy (Georgiev et al., 2016), and seems to be correlated with the properties of the host galaxy, e.g., mass, luminosity, velocity dispersion (Böker et al., 2004; Côté et al., 2006; Ferrarese et al., 2006; Seth et al., 2008; Georgiev et al., 2016). The correlation between the NSC and host mass is also found to be dependent on the galaxy type (see right panel of Figure 1.3). For early-type

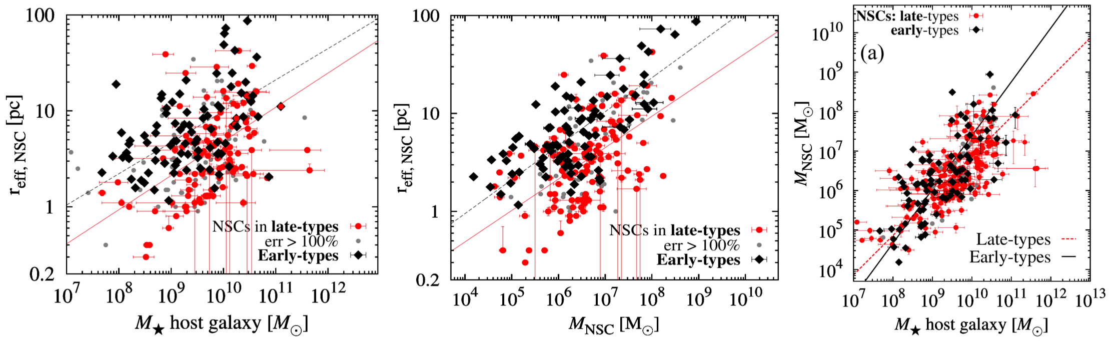

Figure 1.3 Left panel: NSC size vs. host stellar mass relation. Middle panel: NSC size vs. NSC mass relation. Right panel: NSC mass vs. host stellar mass relation. For the three panels red circles and black squares represent late- and early-type galaxies, respectively. Gray circles are for NSCs with uncertainties $>$ 100%. Figures from Georgiev et al. (2016).

galaxies the correlation is steeper than for late-type galaxies. It is unknown if this difference is caused by a bias in the structural decomposition of the observations or due to real physical effects (Georgiev et al., 2016). The relation between the NSC mass and the stellar mass of the host galaxy is non-linear but seems universal for galaxies in different environments, suggesting that instead of the density of the cluster, the mass of the NSC would depend on the mass of their host (Sánchez-Janssen et al., 2018). In addition, NSC masses show a correlation with the luminosity and mass of the bulge of the host galaxies (Ferrarese et al., 2006; Wehner & Harris, 2006; Erwin & Gadotti, 2012; Savorgnan et al., 2016). All these correlations between the host galaxy and its NSC suggest that the NSC properties are not random and might be directly linked to the evolution of the host.

The inability of fitting single stellar population models to the observed spectrum of NSCs suggests that they actually host multiple stellar populations with differences in metallicity and age of a few Gyr (e.g., Walcher et al., 2006; Rossa et al., 2006; Seth et al., 2006; Lyubenova et al., 2013; Carson et al., 2015; Kacharov et al., 2018). The existence of a young population explains the size of the NSC increasing with the wavelength (Georgiev & Böker, 2014; Carson et al., 2015), as young stellar populations are found to be more centrally concentrated than the old ones (e.g., Seth et al., 2008), as observed in the Milky Way (Do et al., 2013; Lu et al., 2013; Feldmeier-Krause et al., 2015).

1.3.2 The Coexistence with Massive Black Holes

All galaxies in the high-mass regime, above $\approx 10^{12} M_\odot$, show signatures of hosting a supermassive black hole (SMBH, $\gtrsim 10^6$M$_\odot$) in their centers. The SMBH mass correlates with the properties of the host galaxy, e.g., mass (Häring & Rix, 2004), velocity dispersion (Ferrarese & Merritt, 2000; Gebhardt et al., 2000), bulge luminosity (Kormendy & Richstone, 1995), light concentration (Graham et al., 2001).

In galaxies of masses between $\sim 10^{10}$ and $10^{12} M_{\odot}$, NSCs are found to coexist with SMBHs (e.g., Seth et al., 2008; Filippenko & Ho, 2003; Graham & Spitler, 2009; Neumayer & Walcher, 2012; Nguyen et al., 2018), as also observed in the Milky Way (Genzel et al., 2010; Schödel et al., 2014a,b; Feldmeier et al., 2014). The similarities in the scaling relations observed between NSCs and SMBHs with their host galaxies suggest that their formation and evolution might be directly connected. Under this consideration, these two objects together have been named central massive objects (CMOs, Ferrarese et al., 2006). Nevertheless, the steepness in the correlations seems to differ: the mass of the NSC and of the SMBH scales with the velocity dispersion of the host as $\sim \sigma^2$ and $\sim \sigma^5$, respectively (Graham 2012, see also Scott & Graham 2013). This might imply that the formation mechanism was not the same for both objects (Antonini, 2013), but it does not refute the possibility that the NSC might be the seed for the SMBH to form and grow.

As shown in Figure 1.2, there is a peak in the nucleation fraction for galaxies with masses of $\sim 10^9 M_{\odot}$, and the fraction decreases towards both sides of the mass regime. This might be a reflection of the coexistence and dominance between the SMBH and the NSC in the center of the host. NSCs could be the birthplaces of SMBHs. In this scenario, NSCs form and dominate the center of galaxies. As part of the stellar evolution, black holes form and merge in the NSCs. Hence, both structures grow and evolve together in coexistence. However, as the central black hole (BH) increases its mass it can reach a point where it will considerably affect the NSC ($M_{BH} \approx 10^8 M_{\odot}$; Antonini et al., 2015), thus becoming the SMBH the dominating component in the CMO.

For galaxies with masses $< 10^{10} M_{\odot}$, the presence of NSCs has been detected. However, no SMBHs have been found in these low-mass galaxies. The CMO for galaxies over $\sim 10^{11} M_{\odot}$ seems to be dominated by a SMBH, with no detection of a NSC signature. Figure 1.4 shows the correlation between the BH mass (M_{BH}) and NSC mass (M_{NC}), where the mass of $3 \times 10^6 M_{\odot}$ and a ratio of $M_{BH}/M_{NC} = 100$ define the different dominance regions: NSC dominated region (lower left of both lines), BH dominated region (upper left of both lines), coexistence or transition region (to the right of both lines). If this scenario is correct, we expect to find intermediate-mass black holes (IMBH, $10^{2-4} M_{\odot}$) in the NSC of low-mass galaxies. However, because of observing limitations, there has not been a definitive proof of their existence.

1.3.3 Formation Mechanisms

Although the properties of NSCs are linked to those of the host galaxy, their origin is still partly unknown. There are two scenarios to explain NSC formation: (i) accretion of GCs driven to the center of the galaxy by dynamical friction effects (Tremaine et al., 1975); (ii) in-situ formation (Milosavljević, 2004) from gas driven to the center, e.g., as a result of galaxy interactions (e.g., Barnes & Hernquist, 1996; Mihos & Hernquist, 1996; Springel et al., 2005; Tissera, 2000; Lagos et al., 2018) or by torques of bars (e.g., Roberts et al., 1979; García-Burillo, S. et al., 2014; Emsellem et al., 2015), then triggering star formation episodes. However, the observed

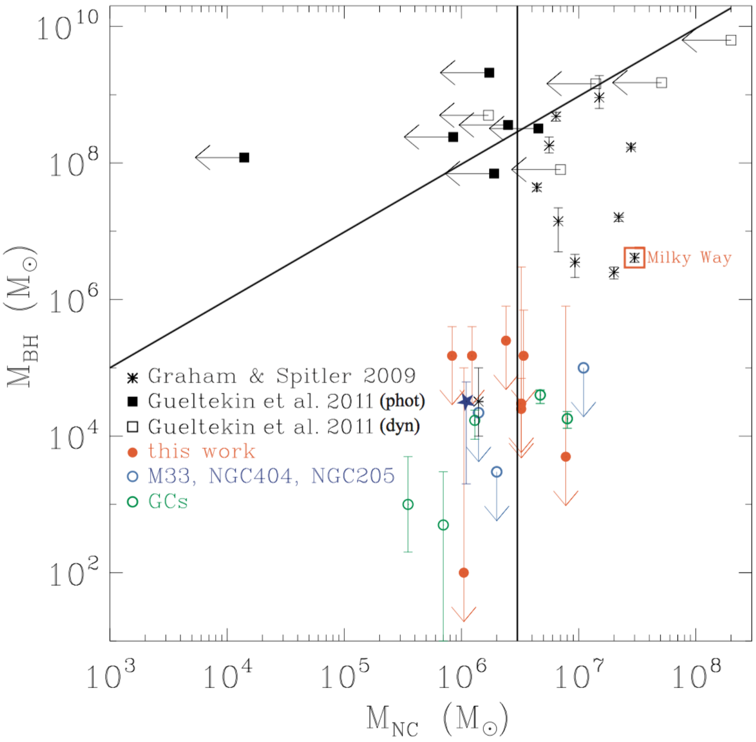

Figure 1.4 Relation between the black hole mass (M_{BH}) and the NSC mass (M_{NC}). Black solid lines show an NSC mass of $3 \times 10^6 M_\odot$ and a ratio of $M_{BH}/M_{NC} = 100$. These lines define a region where the NSC dominates (lower left of both lines), one where the BH dominates the galaxy nuclei (upper left of both lines), an also a transition region (to the right of both lines). Figure from Neumayer & Walcher (2012).

properties of NSCs, like multiple stellar populations with broad age differences, suggested that the two mechanisms might not be exclusive, and that both can contribute to the NSC formation and growth. Thus, a scenario (iii) was proposed as the combination of both mechanisms, ex-situ formation of gas-rich star clusters that fall to the center with their gas reservoir followed by potential in-situ formation (Guillard et al., 2016). Figure 1.5 shows a schematic diagram of the three NSC formation mechanisms.

The formation mechanism of the NSCs seems to depend on the mass and environment of the host galaxy. The low-mass galaxy regime ($\leq 10^{9-10} M_\odot$) would favor the migration scenario (Turner et al., 2012; den Brok et al., 2014b; Arca-Sedda & Capuzzo-Dolcetta, 2014). On the other hand, for high-mass galaxies the in-situ formation scenario becomes more important, contributing up to $\sim 80\%$ of the NSC mass (Antonini et al., 2015). These high-mass galaxies can more easily retain and drive gas to the center triggering new star formation episodes; on the contrary, low-mass galaxies can lose their gas reservoir due to ram pressure effects.

The formation mechanism leaves traces in the properties of the NSC, such as kinematics or affects the behavior of the scaling relations they follow. The merging of GCs can better reproduce the scaling relations in NSCs (e.g., Arca-Sedda & Capuzzo-Dolcetta, 2014), but this is not possible by the in-situ scenario alone (Antonini, 2013). The dynamics of the NSC can provide additional evidence on the formation process. NSCs formed in situ display a high amount of rotation, due to the conservation of the angular momentum of the gas infalling to the center of the galaxy. NSCs formed by GCs accretion, were long considered to be non-rotating systems (Hartmann et al., 2011). However recent simulations showed that NSCs built up by the accumulation of a finite number of GCs can also display a significant amount of rotation independently of the random infall directions and orbital distribution of GCs (Tsatsi et al., 2017). Hence, in any case the formation mechanism plays a role in the dynamics of NSCs.

The NSC of the Milky Way, a late-type galaxy, displays signatures of both mechanisms: (i) this system presents a high spread in metallicity and age, with young stellar populations that suggest in-situ formation, and (ii) an observed kinematic substructure that is misaligned with respect to the main body of the NSC and the Galactic plane, which suggests remnants of accretion (Feldmeier et al., 2014). However, it is not yet possible to constrain which of the mechanisms is the dominating one in the NSC formation. To provide constraints on the relative importance of the formation mechanisms, there is a necessity for further studies and simulations that account for the complex mixture and signatures of multiple populations, as well as different kinematics and scaling relations.

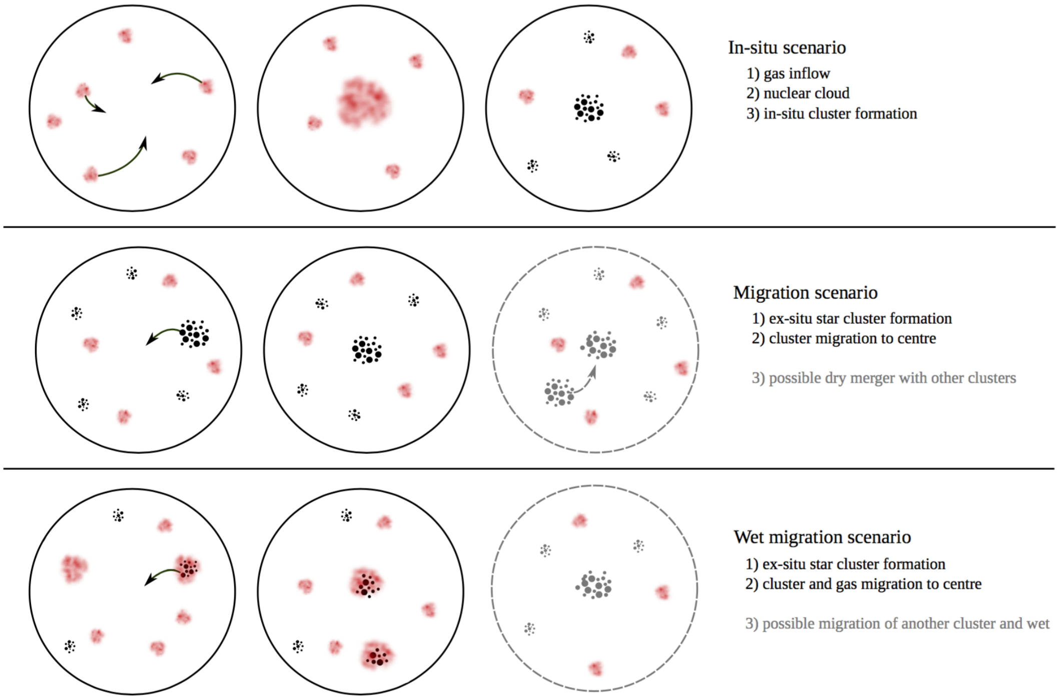
In-situ scenario
1) gas inflow
2) nuclear cloud
3) in-situ cluster formation
Migration scenario
1) ex-situ star cluster formation
2) cluster migration to centre
3) possible dry merger with other clusters
Wet migration scenario
1) ex-situ star cluster formation
2) cluster and gas migration to centre
3) possible migration of another cluster and wet

Figure 1.5 Schematic diagram of the three NSC formation mechanisms. Top: in-situ formation scenario. Middle: GC accretion scenario (or migration scenario). Bottom: accretion of star cluster and gas, followed by in-situ formation. Figure from Guillard et al. (2016).

1.4 Stripped-off Nuclear Star Clusters[1]

As discussed above, a high fraction of galaxies, including dwarfs, host NSCs and likely GC systems. Galaxies can be satellites of larger galaxies, under the constant influence of their tidal fields. Eventually, the satellite might sink toward the center of the potential well of the dominant galaxy while getting tidally disrupted losing its stellar component as streams. In the end, the body of the satellite is totally disrupted and accreted by the dominant galaxy and its GCs will also become part of the larger galaxy. If GCs can survive the strong tidal effects, we expect that NSCs must also survive and end as stripped nuclei. NSCs are, indeed, the densest objects we know and they are too compact to be disrupted (e.g., Pfeffer & Baumgardt, 2013). But, where do we find these stripped nuclei and how do they look like?

As mentioned, the mass of the NSC correlates with the mass of the host (e.g., Georgiev et al., 2016). Thus, depending on the mass of the progenitor galaxy it is presumed that these stripped nuclei can be found as ultracompact dwarfs or high-mass metal complex GCs.

1.4.1 Ultracompact Dwarfs

Ultracompact dwarfs (UCDs) were identified for the first time in the Fornax cluster about two decades ago when they were classified as compact stellar objects (Minniti et al., 1998; Hilker et al., 1999; Drinkwater et al., 2000). They were later also found in other galaxy clusters, e.g., Virgo (Drinkwater et al., 2004), and Coma (Price et al., 2009). UCDs are among the densest stellar systems with masses of 10^6 to $10^8 M_\odot$ and half-light radii between 3 and 50 pc (Brodie et al., 2011). These objects present absolute magnitudes between $-10 \gtrsim M_V \gtrsim -16$.

The observations of UCDs suggest the following scenarios as possible formation paths: (i) UCDs belong to the high-mass end of the GC distribution (Mieske et al., 2004, 2012; Murray, 2009; Pfeffer et al., 2014, 2016); (ii) they are the result of star cluster mergers (Brüns et al., 2011; Renaud et al., 2015); (iii) they are stripped nuclei from massive dwarf galaxies (Bekki et al., 2003; Pfeffer & Baumgardt, 2013). All formation paths are considered feasible given the characteristics of UCDs, making it difficult to realize which fraction of UCDs were formed through each of the scenarios.

UCDs with masses above $10^7 M_\odot$ show signatures of hosting a SMBH at their center, which make up a large fraction of their mass (Seth et al., 2014; Ahn et al., 2017, 2018; Afanasiev et al., 2018). This, or the fact they have an extended SFH (Norris et al., 2015), suggests that a large fraction of massive UCDs are in fact stripped nuclei. With these characteristics, UCDs blend smoothly in mass and size with the massive GCs with no clear dividing line between them. Figure 1.6 shows the comparison between the mass of GCs and UCDs with their central BH mass. The three black lines show different BH mass fractions, from bottom to top, 1%, 10%, and 20%. The UCDs in which SMBHs have been detected are close to the 15% BH mass fraction. These UCDs represent the high-mass regime of stripped nuclei. At lower masses, we find the complex GCs for which the presence of a central IMBH was claimed, but not yet firmly established (e.g., Gebhardt et al., 2005; Noyola et al., 2008; Lützgendorf et al., 2011; Baumgardt, 2017). All of them are classified as GCs, however, they all share a very similar appearance to NSCs in low-mass galaxies, suggesting that they can be the stripped nuclei of dwarf galaxies whose main body has been disrupted by the dominant galaxy (Zinnecker et al., 1988; Böker, 2008; Da Costa, 2016).

---

[1] This section presents part of the content of the Introduction of Alfaro-Cuello et. al 2019 (ApJ in press)

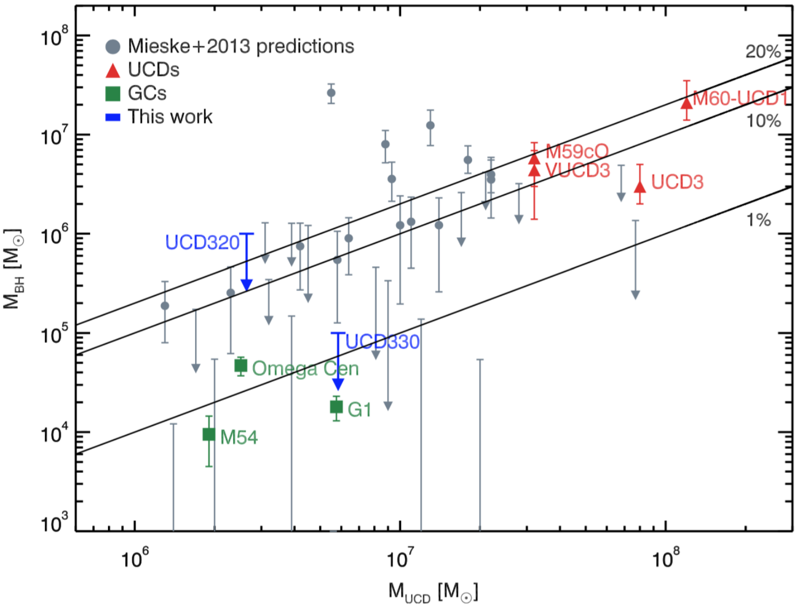

Figure 1.6 The masses of UCDs and GCs are plotted against the (predicted) masses of their central black hole. Gray points represent the predictions and upper limits for UCDs from Mieske et al. (2013), which are based on integrated dispersions. Green squares are the measured black holes in GCs ω Cen, G1, and M54 from Lützgendorf et al. (2013). Red triangles show the four known black hole masses in UCDs from Seth et al. (2014); Ahn et al. (2017); Afanasiev et al. (2018). The three black lines mark constant fractions of 1%, 10%, and 20% black hole mass fraction, respectively. Figure from Voggel et al. (2018).

1.4.2 High-mass, Metal Complex Globular Clusters

There is a “sub-group” of GCs that exhibit strong similarities with the NSCs of dwarf galaxies, e.g., they show high spreads in both age and metallicity, as seen in NSCs in dwarf galaxies.

At masses below $10^7 M_{\odot}$, no equivalent evidence has been found outside of ω Cen’s extended SFH; however, stripped NSCs at these masses are expected to be quite common (Georgiev & Böker, 2014; Pfeffer et al., 2014; Kruijssen et al., 2018). Cosmological simulations of the Milky Way suggest that between one and three GCs with masses higher than $10^5 M_{\odot}$ are tidally stripped nuclei, with a high likelihood of remnants above $10^6 M_{\odot}$ (Pfeffer et al., 2014).

Many of the most massive clusters in the Milky Way and M31 show significant spreads in metallicity (Meylan et al., 2001; Fuentes-Carrera et al., 2008; Willman & Strader, 2012; Bailin, 2018), and the most massive Milky Way GC, ω Cen ($2.5\times10^6 M_\odot$, van de Ven et al., 2006), seems to have age spreads as well (Hilker et al., 2004; Villanova et al., 2014). Terzan 5 is another multicomponent cluster that resides in the bulge of the Milky Way which displays a high spread in iron (Massari et al., 2014) and age (Ferraro et al., 2016; Origlia et al., 2019), with a chemical composition similar to the Galactic bulge.

These observations led to the suggestion that they are former NSCs of dwarf galaxies that have been accreted (Zinnecker et al., 1988; Böker, 2008; Da Costa, 2016), as NSCs are known to have extended SFHs (e.g., Walcher et al., 2005; Kacharov et al., 2018). Metallicity spreads alone could also be due to self-enrichment during formation (Bailin, 2018), however, age spreads are likely a strong indicator of a stripped NSC.

If these "atypical" GCs are former nuclei, we expect they host an IMBH at their center. There is no confirmation yet, but studies suggest that some of them are strong IMBH host candidates: e.g., ω Cen (Noyola et al., 2008; Jalali et al., 2012; Baumgardt, 2017), G1 (Gebhardt et al., 2005), NGC 6388 (Lützgendorf et al., 2011).

1.5 A Unique Laboratory: The Nucleated Sagittarius Dwarf Spheroidal Galaxy

1.5.1 The Sagittarius Dwarf Spheroidal Galaxy

In 1994, Ibata et al. reported the detection of the Sagittarius dwarf spheroidal galaxy (hereafter Sgr dSph), the third most massive Milky Way satellite after the Large and Small Magellanic Clouds. Located at a distance of 18.7 kpc from the Galactic center (Monaco et al., 2004), observations show that it is already considerably affected by the tidal field of the Milky Way (Ibata et al., 1997).

Evidence of the advanced stage of disruption of the Sgr dSph strongly suggested the presence of a stellar stream, thereby motivating the search of such structure. The first signatures of a stellar stream were reported by Totten & Irwin (1998), who found stars in the expected orbital path of the stream with consistent properties to those found in the core of the satellite galaxy. It was not until several years after the Sgr dSph discovery that the data release of large stellar surveys, such as the *Sloan Digital Sky Survey* (SDSS) and the *Two Micron All Sky Survey* (2MASS), allowed the detection of the Sagittarius stellar stream in the Northern Galactic hemisphere (Newberg et al., 2002; Majewski et al., 2003, respectively). Years later, the continuation of the stream was detected in the Southern Galactic hemisphere (Koposov et al., 2012). Both parts of the stream cover a large extension on the sky, going around the Milky Way beyond 360° (Belokurov et al., 2014), proving the advanced degree of disruption with its stellar debris. Both the northern and southern hemisphere parts of the stream show a bifurcation in their leading arms. The bifurcation in the northern arm results in two stellar components separated by $\sim 15^\circ$, one brighter than the other, but with similar stellar kinematics and composition (Belokurov et al., 2006). The bifurcation in the southern arm of the stream results in two components separated by $\sim 10^\circ$, one significantly thicker, brighter, and more metal enriched than the other (Koposov et al., 2012). The SFH of the bright and faint streams suggest that the faint stream is early stripped material which belonged to the outer parts of the progenitor dwarf (de Boer et al., 2015). In both cases, the angular separation between the two components of the arms seems to be constant across the extension around the Milky Way, with no crossing between them. This arm bifurcation is an intriguing feature that simulations on the Sagittarius stream have just partially explained (e.g., Fellhauer et al., 2006; Peñarrubia et al., 2010), giving no definitive answer. One of the proposed scenarios is that the Sgr dSph had a dwarf satellite companion (like the Magellanic Clouds) which fell together into the Milky Way as a group (e.g., Li & Helmi, 2008).

As previously mentioned, stellar streams are widely used to constrain the shape and depth of the gravitational potential of the dominant galaxy. The Sgr dSph and its stream offer an excellent target for the study of the Milky Way gravitational potential. Moreover, the fact that we observe the satellite galaxy in such a current strong disruption process, with its remaining core still intact, makes this system unique. There is no other object available that resembles these characteristics and is at a distance to us where resolved stellar population studies are possible. Simulations have been performed to model the streams and infall of the galaxy toward the Milky Way into their present location (e.g., Martínez-Delgado et al., 2007; Law & Majewski, 2010b; Peñarrubia et al., 2010; Gibbons et al., 2014; Laporte et al., 2019), suggesting multiple pericentric passages, consistent with the observations of the extension of the stream. In addition, a large number of studies on the stellar properties, such as metallicity and kinematics, have been published helping to understand this tidal disruption event and improving the inputs for new simulations that can closely reproduce what we observe today in the sky.

The estimated luminosity of the progenitor galaxy is $\sim 10^8 L_\odot$ ($M_v \sim -15$; Niederste-Ostholt et al., 2012). The chemical distribution in the Sgr dSph suggests a progenitor dark halo mass of $M_{dh} = 6 \times 10^{10} M_\odot$ (Mucciarelli et al., 2017). The progenitor properties suggest that before starting its disruption, the Sgr dSph was likely a Large Magellanic Cloud galaxy type (e.g., Mucciarelli et al., 2017).

The stellar populations in the streams and the core of the Sgr dSph show that the stars display differences in chemical composition and age. This is expected since the stripped stars used to be part of the outer regions of the galaxy. The main body of the Sgr dSph is dominated by a stellar population of intermediate age ($4-8$ Gyr) with $-0.6 < [\mathrm{Fe/H}] < -0.2$ ($> 80\%$) (e.g., Bellazzini et al., 2006a; Layden & Sarajedini, 2000; Monaco et al., 2002; Hasselquist et al., 2017, 2019). In addition, studies revealed that stars also show variations in metallicity and age inside the stream (e.g., Bellazzini et al., 2006b; Monaco et al., 2007; Carlin et al., 2012).

Studies of the Sagittarius stream show the Sgr dSph has not only contributed to the Milky Way with its field stars. The consistency between the Sgr dSph's orbital path and the phase space distribution of GCs in the outer part of the Milky Way halo motivated studies for constraining the former membership of these GCs to the Sgr dSph, finding that the satellite galaxy has significantly contributed to the GC population in the Milky Way (Lynden-Bell & Lynden-Bell, 1995;

Bellazzini et al., 2003; Carraro et al., 2007; Law & Majewski, 2010a). For a summary of the literature for confirmed and candidates of current and former GCs members of the Sgr dSph see Law & Majewski (2010a).

It is unquestionable that the Sgr dSph and its stream are a unique target to address several open questions in astronomy. The stage of its disruption offers a privileged opportunity to understand the effects of these drastic events. Hence, the Sgr dSph has become one of the most studied galaxies in our neighborhood, as it is an important proof of the hierarchical assembly of galaxies. For details on the Sagittarius stream see the review by Law & Majewski (2016).

1.5.2 M54[2]

In addition to all the aforementioned properties and study opportunities offered by the Sgr dSph, this prodigious galaxy also seems to host an NSC, named M54. Thus, this target is the perfect laboratory to understand low-mass galaxy nucleation and to search for the presumed direct link between the most massive metal complex GCs and NSCs.

The NSC of this galaxy was discovered as the GC Messier 54 (NGC 6715) long before the remainder of the galaxy was discovered by Ibata et al. (1994). With a mass of $(1.41 \pm 0.02) \times 10^6 M_\odot$ (Baumgardt & Hilker, 2018), M54 is the second most massive GC in the Galaxy after ω Cen. It is located in the densest region of the Sagittarius stream at the photometric center of the galaxy (Ibata et al., 1994; Mucciarelli et al., 2017) at a distance of 28.4 kpc (Siegel et al., 2011). Figure 1.7 shows an image of the Milky Way and the location of the Sgr dSph and M54.

The Sgr dSph NSC is composed of at least two distinct populations, a metal-poor and metal-rich one, with the metal-rich population having stars as young as $\sim$2 Gyr, while the metal-poor population is consistent with an age of $\sim$13 Gyr (Monaco et al., 2005a; Siegel et al., 2007; Bellazzini et al., 2008). Some authors have referred to these two components as separate objects, a massive metal-poor GC (M54), and a metal-rich component associated with the galaxy (Sgr, or Sgr NS). However, in the context of extragalactic NSCs (where these two populations could not be easily separated), and given the populations' identical photocenters (Monaco et al., 2005b) and radial velocities (Bellazzini et al., 2008), we prefer to think of these components as two (or more) sub-populations of the Sgr dSph NSC.

Monaco et al. (2005b) found that the metal-rich sub-population presents a cusp with a peak located in an indistinguishable position from the center of the metal-poor population, thus displaying a different radial profile in the inner parts in comparison with the rest of the Sgr dSph (Majewski et al., 2003). Ibata et al. (2009) reported that the metal-poor sub-population shows a stellar density cusp, together with a peak in the velocity dispersion. The density profiles from both sub-populations are found to be different (Monaco et al., 2005b; Bellazzini et al., 2008).

---

[2] This section presents part of the content of the Introduction of Alfaro-Cuello et. al 2019 (ApJ in press)

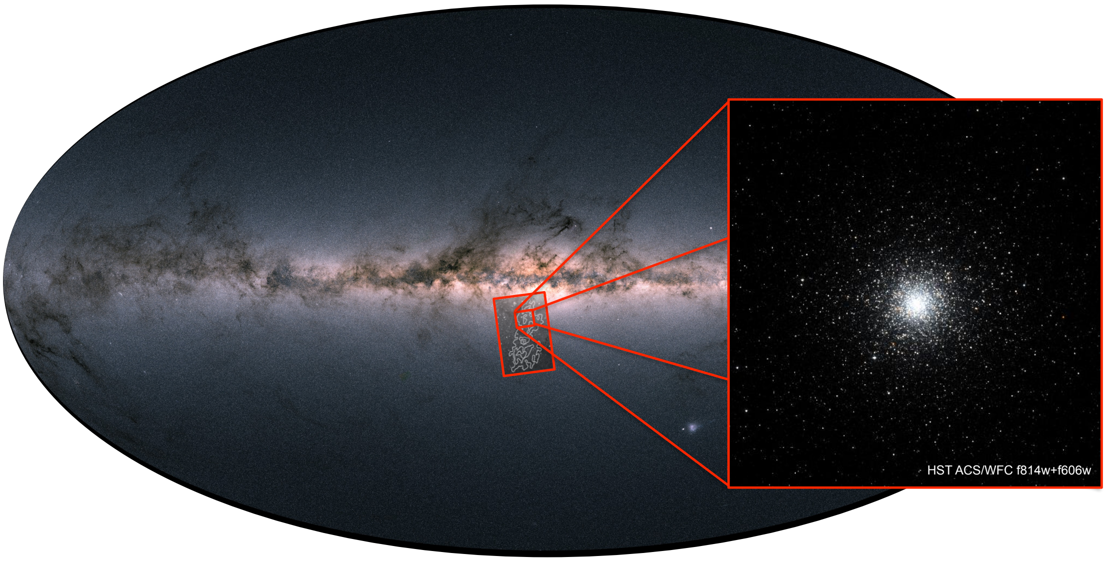

Figure 1.7 Gaia's sky in colour (Credit: Copyright ESA/Gaia/DPAC). The red rectangle shows the position of the Sgr dSph represented by the isopleth maps from Ibata et al. (1994)*. The zoom in red square shows an image of M54 taken with the *HST* ACS/WFC F814W+F606W. *Image cut from: `http://www.poyntsource.com/Richard/m54_sagittarius_dwarf.htm`.

Siegel et al. (2007), using *HST* photometry, suggested that at least four discrete stellar populations are present in the nucleus of the Sgr dSph, revealing a very complex SFH. These populations are characterized by:
(i) [Fe/H]$= -1.8$, $[\alpha/\text{Fe}] = +0.2$ with ages of 13 Gyr;
(ii) [Fe/H]$= -0.6$, $[\alpha/\text{Fe}] = -0.2$ with ages of $4-6$ Gyr;
(iii) [Fe/H]$= -0.1$, $[\alpha/\text{Fe}] = -0.2$ with ages of 2.3 Gyr; and
(iv) [Fe/H]$= +0.6$, $[\alpha/\text{Fe}] = 0.0$ with ages of $0.1-0.8$ Gyr.

Previous spectroscopic studies have focused on the division of the cluster into metal-rich and metal-poor sub-populations (i.e. population (i) above vs. all others). Bellazzini et al. (2008) presented a kinematic analysis for a total of ~ 400 stars (from metal-poor to metal-rich). The systemic velocities of the stars in both metallicity regimes coincide within $\simeq \pm 1.0$ km s^{-1}, consistent with previous findings based on samples with a considerably lower number of stars (Da Costa & Armandroff, 1995; Ibata et al., 1997; Monaco et al., 2005a). According to the authors, the metal-rich stars follow a flat velocity dispersion profile of $\sigma = 10$ km s^{-1} within the central $9\farcm0$ radius. The metal-poor population follows a King profile (King, 1966), which provides a good fit to the surface brightness, at least for the innermost region, as is usually found in GCs. This latter population has a maximum dispersion of $\sigma = 14.2$ km s^{-1} in the center and $\sigma = 5.3$ km s^{-1} at $\sim 3\farcm5$ (~ 29 pc) from the cluster center. Hence, the authors found differences in the kinematics between the two populations in a radial range of $1\farcm5 < r < 6\farcm5$, suggesting different origins. In this picture, the metal-poor population enabled the collection of the gas that formed the metal-rich population, resulting in different velocity dispersion profiles. In addition, Bellazzini et al. (2008) found a weak signal of rotation (< 2 km s^{-1}) for the metal-poor population. This signal seems to increase at radii larger than $10\farcm0$, where a clear sign of rotation is displayed. Based on line-of-sight velocities, Baumgardt & Hilker (2018) reported a central velocity dispersion for M54 of $\sigma_0 = 16.2$ km s^{-1}.

Despite the coincidence in radial velocities, the velocity dispersion profiles differ significantly for these populations, with the metal-rich stars having a much flatter dispersion profile than the metal-poor stars (Bellazzini et al., 2008). To explain the spatial coincidence and the differing dispersion and surface brightness profiles of the different populations, Monaco et al. (2005b) and Bellazzini et al. (2008) suggested the following possible scenarios: (1) Both were formed in situ at the bottom of the potential well of the galaxy, first the metal-poor stars, followed by the metal-rich stars in subsequent star-forming episodes from enriched gas, (2) the metal-poor stars were an ordinary GC that was driven by dynamical friction to the center of the galaxy where a nucleus either had already formed independently or formed subsequently. Using N-body simulations, Bellazzini et al. (2008) showed that the latter scenario is feasible even with a preexisting NSC. More specifically, the dynamical friction inspiral time scale of the metal-poor progenitor GC is <3 Gyr for a wide range of starting radii and initial relative velocities (unlike the other GCs in the Sgr dSph). Furthermore, the end state of these simulations results in radial velocity differences between the pre-existing NSC and migrated GC of <2 km s^{-1}.

Studies on the abundances of the metal-poor and metal-rich population and radial variations of the metallicity have also been published. The metal-poor population displays a large spread in the iron content of its stars ($\sigma_{[\mathrm{Fe/H}]} = 0.186$, Carretta et al., 2010c; Willman & Strader, 2012). In addition, Carretta et al. (2010c) reported that a sodium-oxygen anticorrelation similar to those seen in other GCs is present in the metal-poor population. On the other hand, the authors do not observe any signatures of this anticorrelation in the metal-rich population. Mucciarelli et al. (2017) found a metallicity gradient in the metal-rich population, with this component becoming more metal-poor at larger radii. They also estimated that the chemical distribution they found for the Sgr dSph is consistent with a progenitor of $M_{dh} = 6 \times 10^{10} M_{\odot}$, in agreement with the estimate by Gibbons et al. (2017).

Finally, kinematic observations of the metal-poor population have also been used to determine if it hosts a central massive black hole. Two studies have reported a possible detection based on dynamical modeling ($M_{BH} \sim 10^4 M_{\odot}$; Ibata et al. 2009; Baumgardt 2017).

Studies on NSCs commonly cover the high-mass galaxy regime. There are not many studies on NSCs in the low-mass galaxies. This restricts our knowledge about them and raises several questions, such as how many of the massive GCs in our Milky Way are former nuclei of low-mass galaxies? What are the detailed properties (morphology, stellar ages, metallicity, and kinematics) we would expect these systems to have? The goal of this Thesis is to start answering these open questions through M54, an excellent laboratory and exclusive key for a better understanding of the NSC in the low-mass galaxy regime. The next section shows the plan for this objective.

1.6 Thesis Outline

As previously mentioned, a high fraction of dwarf galaxies host an NSC. The strong similarities between the characteristics of their NSCs and high-mass, metal-complex GCs suggest that they are former nuclei of dwarf galaxies that have been disrupted and accreted by the Milky Way. A privileged example is observed in the advanced state of disruption of the Sgr dSph. The NSC of this galaxy, M54, offers a perfect opportunity to understand low-mass galaxy nucleation, how they might have formed and evolved. In this Thesis, we aim to provide valuable information to understand the presumed direct connection between the most massive, metal-complex GCs and NSCs through this key object: M54.

In Chapter 2 we present the data set this work is based on. We include the analysis carried out to extract the single stellar spectra from the data set and the stellar characterization that allowed us to disentangle the multiple stellar populations in M54. In Chapter 3 we complement the characterization by adding kinematic information for the multiple stellar populations presented in Chapter 2. Chapter 4 includes the preliminary results on the discrete dynamical modeling on M54. This chapter paves the path to the discrete modeling for the different populations in M54, which will be based on chemo-dynamical models. Finally, in Chapter 5 we summarize and discuss the results of this work and end with an outlook toward future prospects.

The contents of Chapters 2, 3 and 4 of this Thesis are based on the following papers, respectively:

- *"A deep view into the nucleus of the Sagittarius Dwarf Spheroidal Galaxy with MUSE. I. Data and stellar populations characterization."*
  M. Alfaro-Cuello, N. Kacharov, N. Neumayer, N. Lützgendorf, A.C. Seth, T. Böker, S. Kamann, R. Leaman, G. van de Ven, P. Bianchini, L. L. Watkins, and M. Lyubenova.
  ApJ in press.

- *"A deep view into the nucleus of the Sagittarius Dwarf Spheroidal Galaxy with MUSE. II. Kinematic characterization of the stellar populations."*
  M. Alfaro-Cuello, N. Kacharov, N. Neumayer, A. Mastrobuono-Battisti, P. Bianchini, S. Kamann, A.C. Seth, N. Lützgendorf, T. Böker, R. Leaman, G. van de Ven, L. L. Watkins, and M. Lyubenova.
  To be submitted.

- *"A deep view into the nucleus of the Sagittarius Dwarf Spheroidal Galaxy with MUSE. III. Discrete dynamical modeling of M54."*
  M. Alfaro-Cuello, et al.
  In preparation.

Chapter 2

Stellar Population Characterization of M54

In the Introduction we presented the main characteristics in the literature of the subpopulations in M54 in the Introduction, showing that it is a key object for understanding NSCs in the low-mass galaxy regime before the total disruption of the galaxy, as still resides in the center of its host. Its proximity enables us to estimate physical parameters for individual stars, providing valuable information on the nucleus itself and on its coevolution with the progenitor galaxy. This object offers the opportunity to better understand the link between the most massive GCs and NSCs as stripped nuclei of low-mass galaxies. In extragalactic NSCs studies, the differentiation of multiple subpopulations is challenging. Previous works identifies M54 with the metal-poor population, and the nucleus of the Sgr dSph to the metal-rich population. We prefer to think of these components as two (or more) subpopulations of the Sgr dSph NSC. In this chapter we will refer to the different subpopulations in the NSC of the Sgr dSph considering their stars physical parameters (e.g., metallicity, age).

The Multi-Unit Spectroscopic Explorer (MUSE) spectrograph is an excellent instrument for studying individual stars in GCs (i.e. Husser et al., 2016; Kamann et al., 2018). Using data acquired with this instrument we develop an extremely detailed analysis of the NSC of the Sgr dSph, constraining its properties and SFH.

In this chapter we present the first part of our study on M54. We describe the data in Section 2.1, including the extraction of the single stellar spectra. Section 2.2 presents our analysis, including LOS velocity, membership probability, metallicity and age measurements. Our results are presented in Section 2.3, we discuss these in Section 2.4 and conclude in Section 2.5.

2.1 Data

2.1.1 Observations and Data Reduction

The data set was acquired with Multi-Unit Spectroscopic Explorer (MUSE, Bacon et al., 2014), an integral field spectrograph mounted at the UT4 of the Very Large Telescope at the Paranal Observatory in Chile, between June 29th and September 19th 2015 in run 095.B-0585(A) (PI: Lützgendorf).

A total of 16 pointings, with a field of view (FOV) of $59''\!.9 \times 60''\!.0$ each, create a $4{\times}4$ mosaic that covers a contiguous area out to $\sim$2.5 times the half-light radius of M54 ($\mathrm{R_{HL}} = 0'\!.82$, Harris, 1996, 2010 update), equivalent to ~ 25 times its core radius ($\mathrm{R_c} = 0'\!.09$, Harris, 1996, 2010 update). The estimated tidal radius of M54 is $\mathrm{R_t} = 9'\!.87$ (assuming a King-model central concentration of $c = 2.04$, Harris, 1996, 2010 update). Due to overlaps between neighboring pointings, the observations cover a FOV of $\sim 3'\!.5 {\times} 3'\!.5$ (1 arcmin corresponds to 8.27 pc at an assumed distance of 28.4 kpc, Siegel et al. 2011). This results in a total FOV of 29 pc×29 pc. The data have a wavelength coverage of 4800 - 9300 Å and a spectral resolution increasing with wavelength from $R \sim 1750$ to $R \sim 3750$. The spatial sampling is $0''\!.2\ \mathrm{pixel}^{-1}$. Each field was observed with three exposures, applying offsets in rotation of 90° between them (no dithering) to increase the homogeneity of the data across the FOV. The exposure time for each of the three exposures was chosen to be 400 seconds for the inner 4 pointings and 610 seconds for the outer 12 pointings. This was done to avoid saturation of the innermost crowded region with high surface brightness. During the observations, the air mass varied from 1.0 to 1.9, and the seeing between $0''\!.5$ - $1''\!.2$. Figure 2.1 shows the color image of the $4{\times}4$ mosaic obtained from the MUSE data using synthetic i, r, and z filters.

The data reduction was performed using the MUSE pipeline (version 1.2.1, Weilbacher et al., 2014). The pipeline includes all tasks for the data reduction process: bias creation/subtraction, flat-fielding, illumination correction and wavelength calibration. Before combining the single exposures, they were flux-calibrated using a standard star and corrected for the barycentric motion of the Earth.

2.1.2 Stellar Spectra Extraction

We extract individual stellar spectra with PampelMuse (Kamann et al., 2013). This tool takes a photometric catalog as a reference for the positions and magnitudes of the stars in the FOV. It models the change in the point spread function (PSF) as a function of wavelength and allows deblending of sources efficiently even in crowded and dense regions. A reference stellar catalog for M54 was published by Siegel et al. (2007) as part of the ACS Survey of Galactic Globular Clusters (Sarajedini et al., 2007). The catalog includes source positions and F606W (V) and F814W (I) magnitudes with their respective uncertainties. Its total coverage is larger than the MUSE data set FOV.

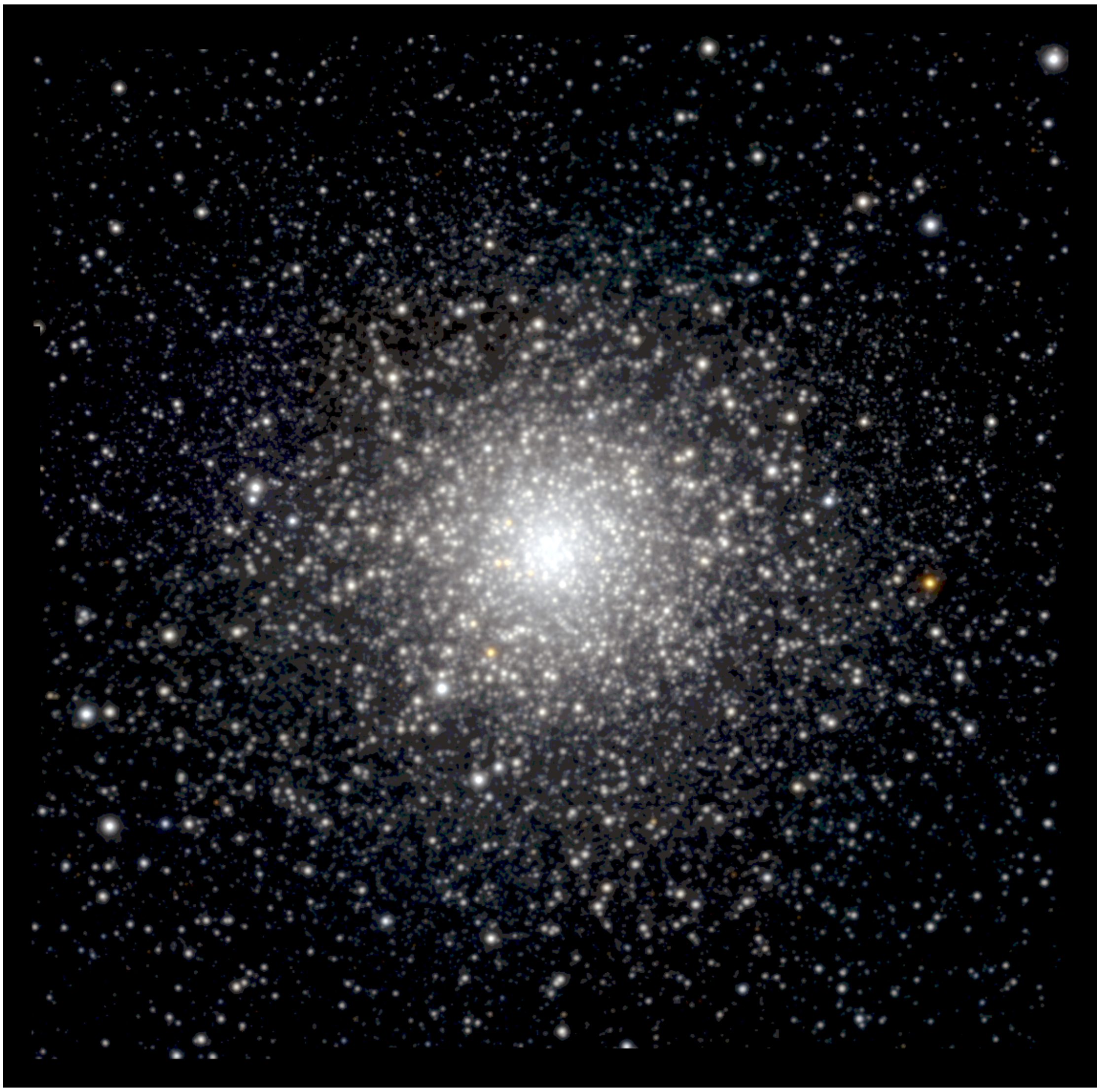

Figure 2.1 Color image obtained from the MUSE data of the Sgr dSph NSC, using synthetic i, r, and z filters. The image is a 4×4 mosaic of 16 MUSE pointings, covering $\sim$2.5 R_{HL} ($R_{HL} = 0\farcm82$, Harris 1996, update 2010) of this NSC. The total covered field of view – considering overlaps – is $\sim 3\farcm5 \times 3\farcm5$, corresponding to 29 pc×29 pc ($1\farcm0 = 8.27$ pc). North is up and east is to the left.

We extract the spectra of $\sim$55 000 stars from the entire field. For our subsequent analysis we only consider the spectra with signal-to-noise ratio $S/N \geq 10$, which are labeled by PampelMuse as good extracted spectra. Within the entire MUSE FOV, we extract good spectra for a total of $\sim$7 000 different stars in the magnitude range of $22 < \mathrm{F814W} < 13$ (I band).

In our stellar sample we do not include main-sequence (MS) stars below the oldest turnoff point since they are fainter than $I \sim 21$ and their spectra are typically below our $S/N = 10$ threshold.

2.2 Analysis

To measure physical stellar parameters, we use ULySS (University of Lyon Spectroscopic Analysis Software; Koleva et al., 2009), a tool for determination of atmospheric parameters of stars through interpolating and fitting stellar library templates to the observed spectrum in the wavelength range of 3900 to 6800Å. We note that the spectral wavelength range of MUSE allows us to fit from 4800 to 6800Å only, and we masked the Na I D line region between 5850 and 5950 Å of the observed spectrum. The observed spectrum is compared with a library of synthetic spectra with varying metallicity, surface gravity, and temperature. The best fit is achieved by interpolation within the synthetic library and χ^2 minimization. The fit performed by UlySS is a Levenberg-Marquardt local minimization for nonlinear parameters, while for the linear ones it uses a bounded-values least square. The synthetic spectroscopic grid available in ULySS is built on the basis of the ELODIE 3.2 library (Wu et al., 2011). It is limited to a metallicity range of $-2.5 < [\mathrm{Fe/H}] < 0.5$. ULySS also simultaneously estimates the line-of-sight velocity shifts of the input spectra. Finally, ULySS derives the uncertainties of the different physical parameters via Monte Carlo simulations. For stars in overlapping regions, where multiple spectra are extracted, the final values for the line-of-sight velocity and metallicity are the weighted mean and its uncertainty of the multiple ULySS measurements.

Figure 2.2 shows three examples of the fitting performed by ULySS for stars with a spectrum of S/Ns of 14 (close to the minimum value of 10), 48, and 100. We use a multiplicative polynomial of order 6, which provides sufficiently good normalization of the observed spectra without the danger of overfitting.

2.2.1 Line-of-sight Velocity

From the spectral fitting performed by ULySS we obtain the line-of-sight (LOS) velocities for each star. Since the space motion of the nucleus can mimic the effect of an additional rotation component, we correct the LOS velocity values for this effect, known as perspective rotation, using Equation 6 in van de Ven et al. (2006). We use the absolute proper motion of the cluster M54 $V_W = -2.82 \pm 0.11$ mas yr^{-1} and $V_N = -1.51 \pm 0.14$ mas yr^{-1} (Sohn et al., 2015). These values are in good agreement with the recent values based on *Gaia* data by Vasiliev (2019). We obtain correction values between -0.3 and 0.3 km s^{-1}.

In Section 2.2.4, we discuss the agreement between velocity measurements derived for stars observed in multiple MUSE pointings.

2.2.2 Sgr dSph NSC Membership

The position of the Sgr dSph with respect to the Milky Way and the large FOV of the MUSE data mosaic result in a considerable amount of contamination of nonmember stars in our Sgr

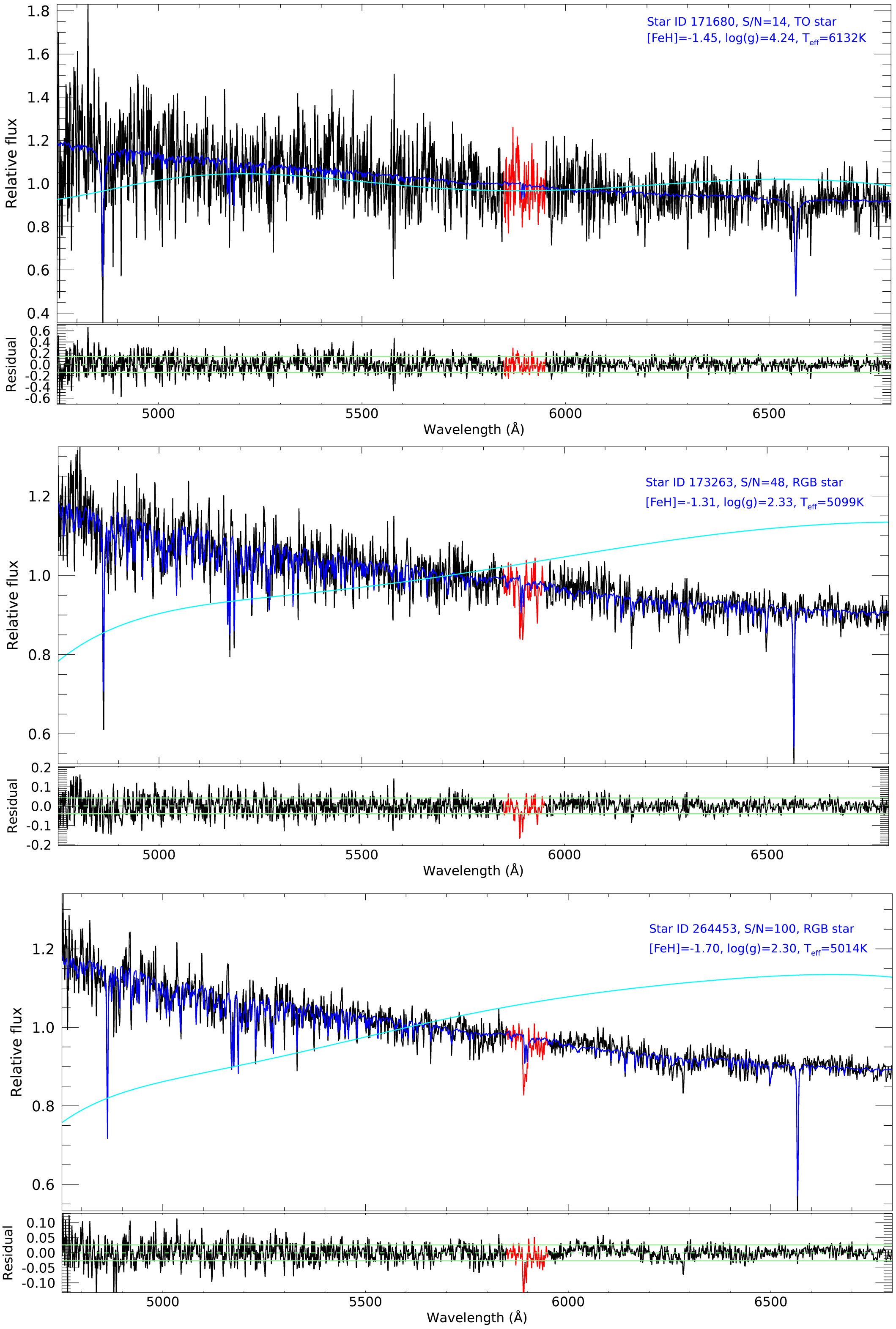

Figure 2.2 Three examples of the fitting performed by ULySS (Koleva et al., 2009) for different types of stars with S/N of 14 (close to minimum of 10), 48, and 100, in the wavelength range of 4701 – 6800Å . Top panels: the best fit is represented in blue, data not considered for the fit in red (both panels), and the multiplicative polynomial in turquoise. Bottom panels: residual of the spectrum fitting (black). Overplotted in dashed and solid green are the mean and the 1σ deviation, respectively.

dSph NSC sample. We determine the membership probability based on the iterative expectation maximization technique using "clumPy"[1] (Kimmig et al., 2015). We use our LOS velocity measurements and the distance of the stars to the center of the cluster M54 as input values (no metallicity estimates considered).

This procedure is described in detail by Walker et al. (2009) and later with some variations by Kimmig et al. (2015). The technique iteratively estimates the mean velocity and velocity dispersion of the cluster plus the membership probability of each star until all the parameters converge. We use a foreground/background contamination model for the Milky Way based on the Besançon model of the Galaxy (Robin et al., 2003).

The membership probability obtained with the expectation maximization technique for each star is represented by color in the radius versus velocity plot in Figure 2.3. From our total sample of 7 000 stars we consider those with probability $\geq 70\%$ to be members of the Sgr dSph NSC, leaving a total of 6 651 members.

We obtain a maximum likelihood median LOS velocity for the member stars (dark red points) of $141.34 \pm 0.18\,\mathrm{km\ s^{-1}}$ and a median central velocity dispersion of $16.31 \pm 0.28\,\mathrm{km\ s^{-1}}$. The LOS velocity estimate is in good agreement with previous works, e.g., $V_{LOS} \sim 141\,\mathrm{km\ s^{-1}}$ by Bellazzini et al. (2008) for the metal-poor and metal-rich populations. From this point, the analysis is carried out on a sample that only includes the members of the Sgr dSph NSC determined by this technique.

In the CMD in Figure 2.4 we show the full sample of extracted single stellar spectra. Member stars of the Sgr dSph NSC (probability $\geq 70\%$) are color-coded by the S/N logarithm, while nonmembers (probability $< 70\%$) are shown in gray. The stellar photometry information in F606W (V) and F814W (I) filters is extracted from the M54 *HST* reference catalog.

2.2.3 Metallicity Estimates

For the metallicity estimates we use two independent methods to test the robustness of our results. One method is based on spectral fitting, this is performed by UlySS (Koleva et al., 2009). The second method used is based on the sum of the equivalent width of the calcium triplet lines (CaII triplet) at 8498, 8542, 8662 Å and their relation with the metallicity in red giant stars. We used the CaII triplet metallicity calibration published by Carrera et al. (2013).

2.2.3.1 Metallicity from Full Spectrum Fitting

The top panel of Figure 2.5 shows the metallicity histogram for the member stars of the Sgr dSph NSC. In the bottom panel, we present the relation between radius and metallicity for the sample of 6 651 stars as derived with ULySS, color-coded by the metallicity uncertainties. Two clear

---

[1] `https://github.com/bkimmig/clumpy`

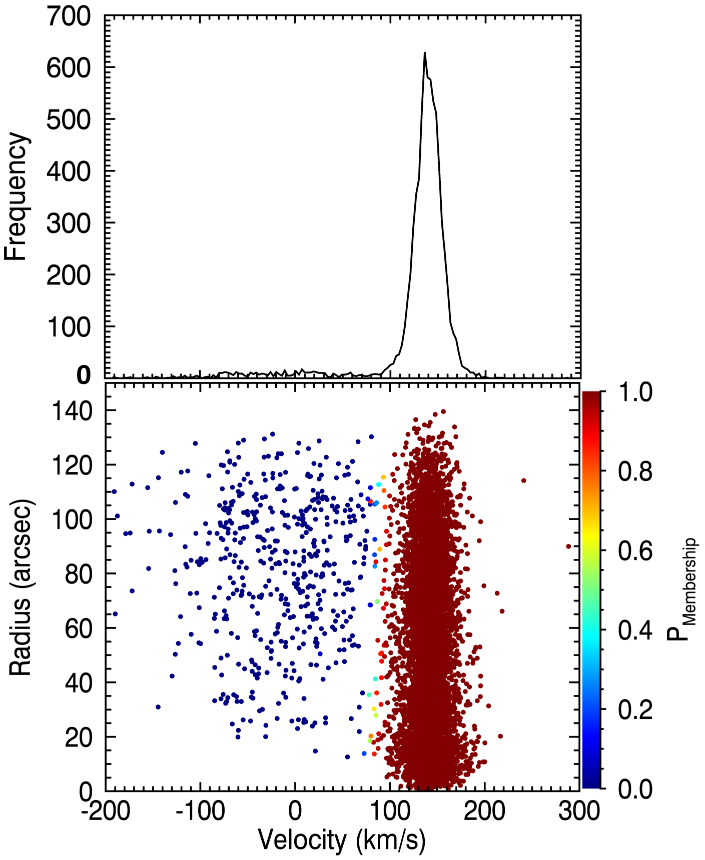

Figure 2.3 Top: distribution of the LOS velocities for the extracted stars with S/N$\geq$ 10 from the entire MUSE FOV. Bottom: radius vs. velocity for our stellar sample color-coded by the cluster membership probability ($P_{\rm Membership}$). We consider as member stars of the Sgr dSph NSC those with probability $\geq 70\%$.

distributions in metallicity become apparent: a metal-poor population at $[\mathrm{Fe/H}] = -1.5$ and a metal-rich population around $[\mathrm{Fe/H}] = -0.3$ with a separation at $[\mathrm{Fe/H}] = -0.8$. The median metallicity uncertainty is 0.05 dex.

In the top panel of Figure 2.6 we present the CMD corresponding to all the Sgr dSph NSC members color-coded by metallicity (hereafter CMD+metallicity, and a zoom-in onto the turnoff region; bottom panel). We overplotted in blue, green, and orange isochrones from the Dartmouth Stellar Evolution Database (Dotter et al., 2008) corresponding to different stellar populations in the Sgr dSph NSC, using as a reference the work by Siegel et al. (2007). We are able to see stars in different evolutionary stages: turnoff point (TO), red giant branch (RGB), horizontal branch (HB), asymptotic giant branch (AGB), red clump (RC), and even the extreme horizontal branch (EHB) and the blue plume (BP). The CMD shows clear evidence for an old metal-poor population, as well as at least two distinct younger populations with metallicity $\gtrsim -0.4$ that agree well with the 4.5 – 6 Gyr isochrone highlighted by Siegel et al. (2007).

For our complete sample of member stars we estimate a mean metallicity of $[\mathrm{Fe/H}] = -1.06$, with a standard deviation of $\sigma = 0.64$. For the metal-poor stars ($[\mathrm{Fe/H}] < -0.8$) we obtain a

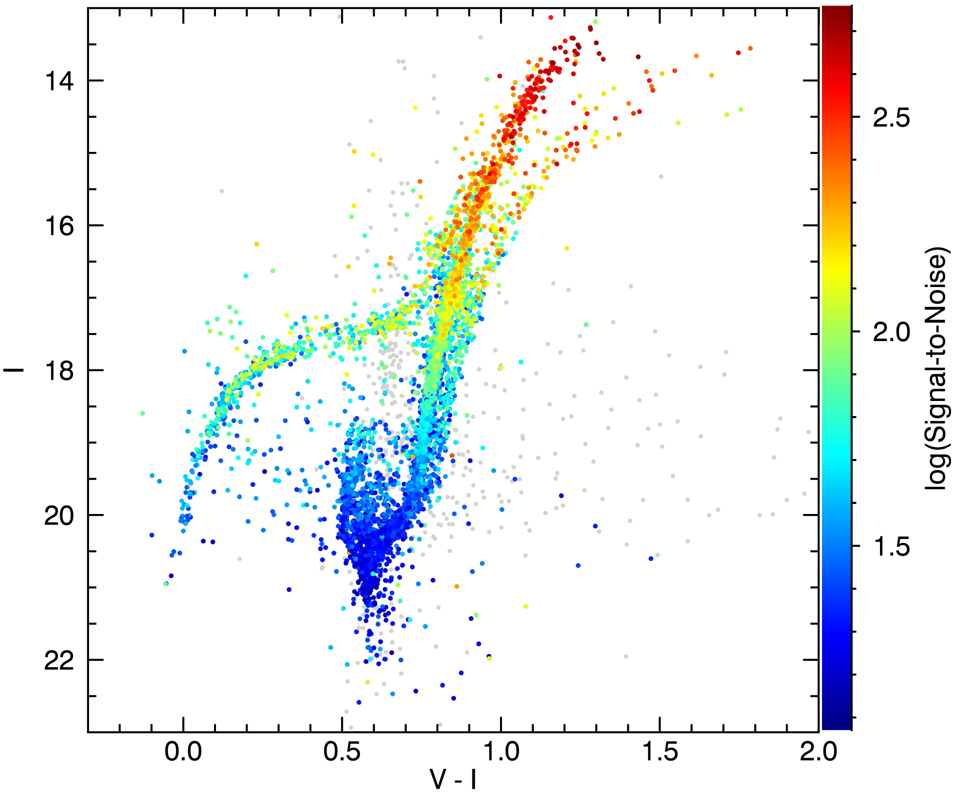

Figure 2.4 CMD for the total number of extracted spectra with S/N≥ 10. Stellar photometry information in F606W (V) and F814W (I) filters (*HST*/ACS WFC) taken from the M54 catalog (Siegel et al., 2007) of the ACS Survey of Galactic Globular Clusters (Sarajedini et al., 2007). Member stars of the Sgr dSph NSC (probability ≥ 70%) are color-coded by the S/N logarithm and nonmembers (probability < 70%) are shown in gray.

mean metallicity of $[\mathrm{Fe/H}] = -1.45$ and a standard deviation of $\sigma = 0.32$. This is in good agreement with previous works, such as Brown et al. (1999) and Da Costa & Armandroff (1995) with an estimate of $[\mathrm{Fe/H}] = -1.55$, and later by Carretta et al. (2010b), who estimated a metallicity of $[\mathrm{Fe/H}] = -1.559 \pm 0.021$ dex.

In the case of the stars in the metal-rich regime ($[\mathrm{Fe/H}] > -0.8$), we obtain a mean value of $[\mathrm{Fe/H}] = -0.27$ and a standard deviation of $\sigma = 0.29$. In this case, the metallicity measurement differs from previous studies. Carretta et al. (2010b) obtained a metallicity value of $[\mathrm{Fe/H}] = -0.622 \pm 0.068$ dex, and Mucciarelli et al. (2017) obtained $[\mathrm{Fe/H}] = -0.52 \pm 0.02$ dex. A possible explanation for this difference is discussed in Section 2.3.1.

We observe that our metallicity distribution (see top panel of Figure 2.5) is highly consistent with the one presented by Mucciarelli et al. (2017) for a total of 76 stars in a radius range of $0\farcm0 < \mathrm{R} \leqslant 2\farcm5$. Since the FOV of our MUSE data partially overlaps with those in Carretta et al. (2010b) and Mucciarelli et al. (2017), for consistency, we cross-matched the samples using coordinate information for the stars with $I \leqslant 17.75$ mag, where the S/N of the spectra is larger and warrants reliable metallicity measurements.

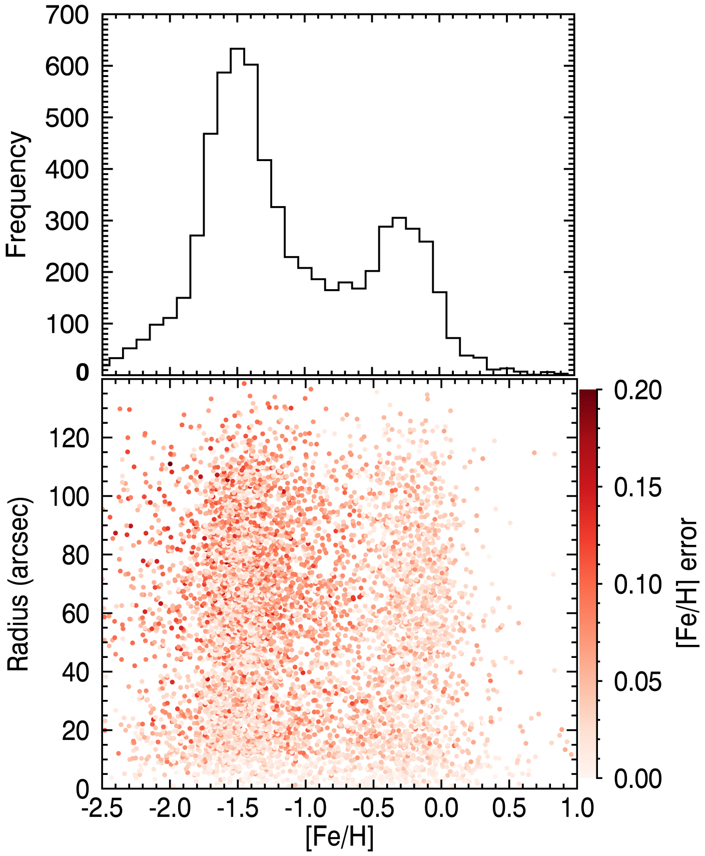

Figure 2.5 Top: metallicity histogram of the member stars of Sgr dSph NSC. Bottom: Radius vs. metallicity plot for the same sample. The stars are color-coded by the uncertainties in the [Fe/H] measurements.

In the top panel of Figure 2.7 we present the difference in [Fe/H] (Δ[Fe/H]) of the 51 stars that are in common between this work and Mucciarelli et al. (2017, red circles), and the 36 with Carretta et al. (2010b, blue circles). The dashed black line shows a $\Delta[\mathrm{Fe/H}] = 0$. For Δ[Fe/H] between this work and Mucciarelli et al. (2017), we obtain a mean value of 0.05 ± 0.02 dex, with a standard deviation of $\sigma = 0.17$. For Δ[Fe/H] between this work and Carretta et al. (2010b), we have a mean value of 0.15 ± 0.03 dex, with a standard deviation of $\sigma = 0.16$. With the respective colors, we include in the figure the Δ[Fe/H] mean values as solid lines, the dashed lines show the area confined by the error of the mean. In this analysis we observe a good agreement between our metallicity measurements and those of previous studies, which use different methods and, in the case of Carretta et al. (2010b), high-resolution spectra.

In the bottom panel of Figure 2.7 we show the relation between the metallicity values from this work and those of Mucciarelli et al. (2017, 51 stars, red circles) and Carretta et al. (2010b, 36 stars, blue circles). In addition, we include the 13 stars in common between Carretta et al. (2010b) and Mucciarelli et al. (2017) as gray circles. The cross-match between these 13 stars and our sample gives eight stars in common. These stars are included in green circles when comparing this work with Mucciarelli et al. (2017) and green squares when comparing with Carretta et al. (2010b).

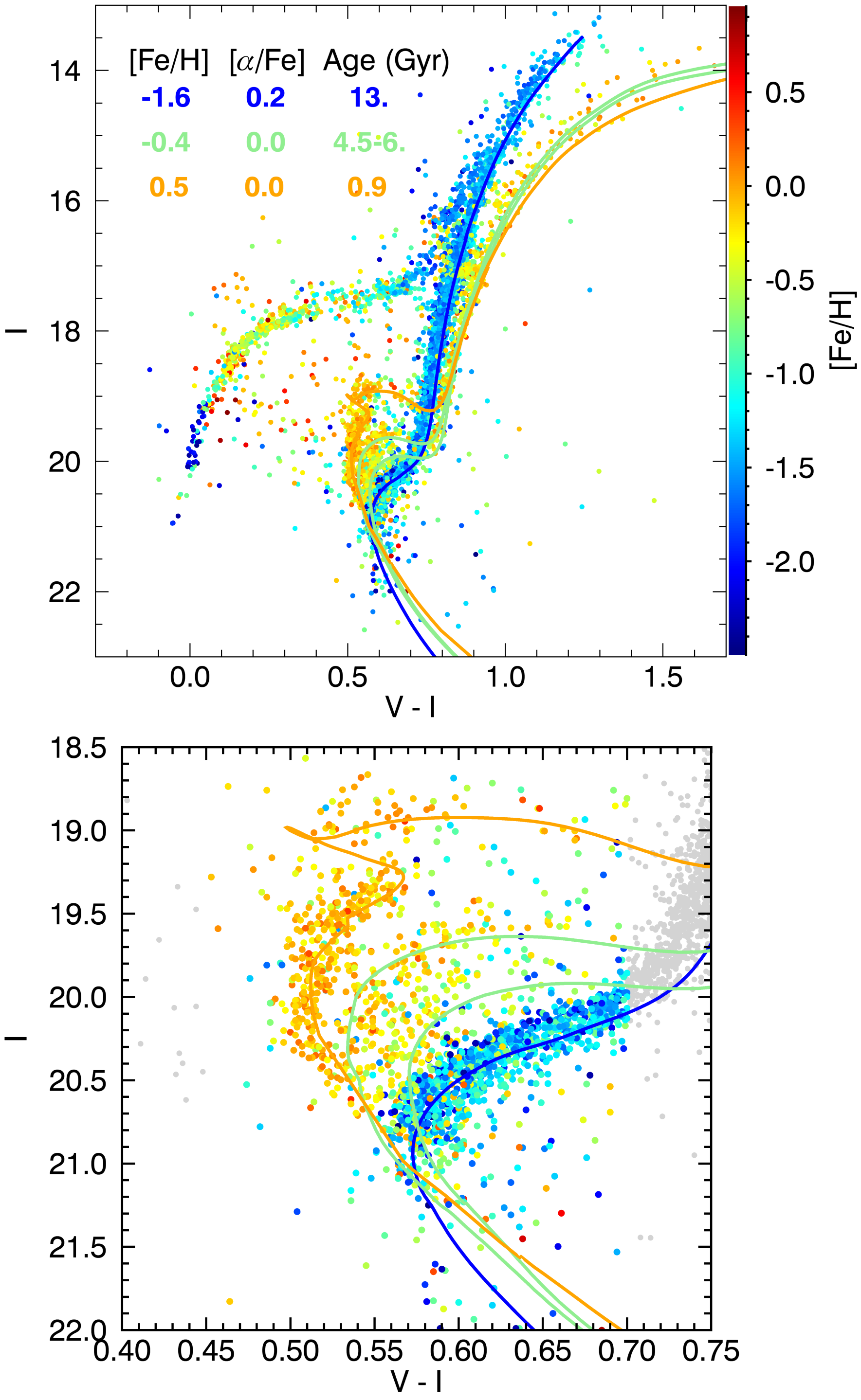

Figure 2.6 Top panel: CMD for the Sgr dSph NSC members color-coded by metallicity (CMD+metallicity) estimated with ULySS. Bottom panel: Zoom into the TO region. Updated isochrones from the Dartmouth Stellar Evolution Database are overplotted in blue, green, and orange for three stellar populations published by Siegel et al. (2007).

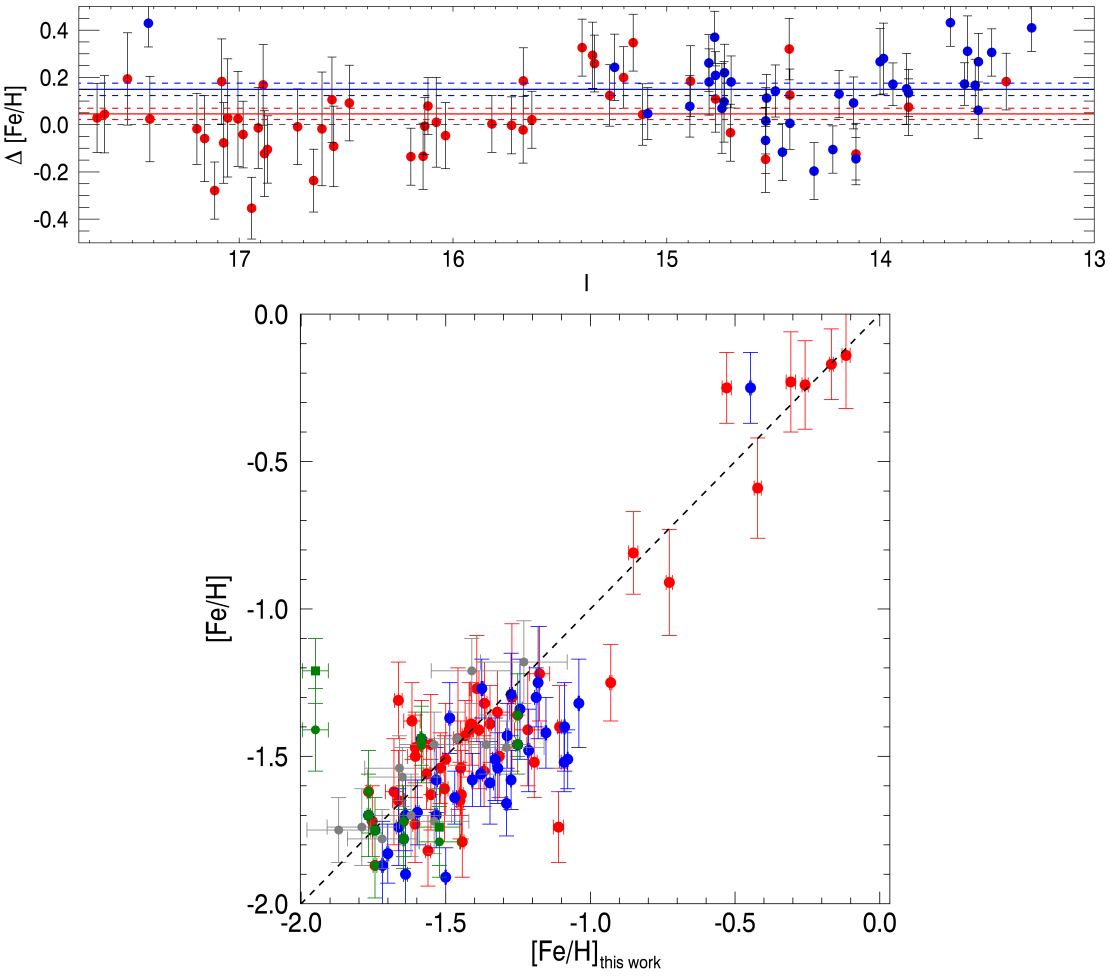

Figure 2.7 Top: difference in metallicity [Fe/H] between this and other works for stars with $13 \leqslant I \leqslant 17.75$ mag. The 51 red circles show the Δ[Fe/H] between this work and Mucciarelli et al. (2017), and the 36 blue circles are for Carretta et al. (2010b). The mean Δ[Fe/H] between this work and Mucciarelli et al. (2017) is 0.05 ± 0.02 dex, with $\sigma = 0.17$. For Δ[Fe/H] between this work and Carretta et al. (2010b), the mean is 0.15 ± 0.03 dex, with $\sigma = 0.16$. The solid red and blue lines show the mean value of the respective Δ[Fe/H] estimates, while the same color dashed lines show the area confined by the mean error. The dashed black line shows a $\Delta[\mathrm{Fe/H}] = 0$. Bottom: relation between [Fe/H] estimates from this work and those of other works: red circles for Mucciarelli et al. (2017, 51 stars), and blue circles for Carretta et al. (2010b, 36 stars). The gray circles represent the relation of 13 common stars between Carretta et al. (2010b) and Mucciarelli et al. (2017). The eight common stars between the three samples are represented as green circles when comparing this work with Mucciarelli et al. (2017) and green squares when comparing with Carretta et al. (2010b). The dashed black line shows a one-to-one relation.

2.2.3.2 CaII Triplet Metallicity

The second method we use to estimate the metallicity is based on the calcium triplet lines (CaII triplet) at 8498, 8542, 8662 Å (see, e.g., Starkenburg et al. 2010; Carrera et al. 2013). We use the calibration presented by Carrera et al. (2013), obtained using the CaII triplet and calibration measurements obtained from hundreds of RGB star observations.

These nonlinear calibrations are specifically tailored toward the metal-poor regime, reaching reliable estimates of metallicity for stars between $-4.0 < [\mathrm{Fe/H}] < 0.5$. CaII triplet lines are strong on the RGB, but their strength depends on the joint effects from metallicity, temperature, and surface gravity. Therefore, to obtain just the effect due to the metallicity, the authors removed these last two contributions using luminosity indicators in order to obtain the following relation (Equation 2 in Carrera et al. 2013):

$$\begin{aligned}[\mathrm{Fe/H}] = a + b \times \mathrm{Mag} + c \times \Sigma\mathrm{Ca} + d \times \Sigma\mathrm{Ca}^{1.5} \\ + e \times \Sigma\mathrm{Ca} \times \mathrm{Mag}\end{aligned} \tag{2.1}$$

We use Mag – the luminosity indicator – as $V - V_{\mathrm{HB}}$, where $V_{\mathrm{HB}} = 18.16$ (Harris, 1996) is the average magnitude of the HB. The coefficient values according to Carrera et al. (2013) are as follows: $a = -3.45$, $b = 0.11$, $c = 0.44$, $d = -0.65$, $e = 0.03$. ΣCa corresponds to the sum of the equivalent width (Σ EW) of the three CaII lines. For additional details see Carrera et al. (2013).

We applied the Doppler correction to the spectra using the LOS velocity values of each star and performed a continuum normalization. We fit a Gauss and Voigt profile to estimate the EW of the CaII triplet lines. We use the spectral ranges for these lines defined by Armandroff & Zinn (1988). We find that Voigt profiles provide better fits than Gaussian profiles for high S/N; therefore we use Voigt profile fits for estimating the metallicity. In Figure 2.8 we show fitting examples for two stars with different S/N values ($\mathrm{S/N} = 10$ and $\mathrm{S/N} = 95$). The best-fit Voigt profiles are overplotted as a dashed red line.

Using the Σ EW values from the Voigt fitting in the calibration in equation 2.1 we obtain metallicity values from $-2.9 < [\mathrm{Fe/H}] < 0.5$. Since this calibration is limited to RGB stars, for this procedure we consider a cut in $V - I = 0.7$, selecting 4 051 stars for the metallicity estimates in the sample of members of the Sgr dSph NSC. In the top panel of Figure 2.9, we show the Σ EW versus $V - V_{\mathrm{HB}}$; overplotted in red lines are the metallicity values for this calibration. The middle panel shows the metallicity histogram of the metallicity values obtained with this method (red). For comparison, we have overplotted the metallicity histogram of the estimates obtained performing full spectral fitting using ULySS (Koleva et al., 2009, blue) for the same sample of RGB stars (see Section 2.2.3.1). The vertical black line on the left shows the average metallicity for the metal-poor population ($[\mathrm{Fe/H}] = -1.559 \pm 0.021$ dex), estimated by Carretta

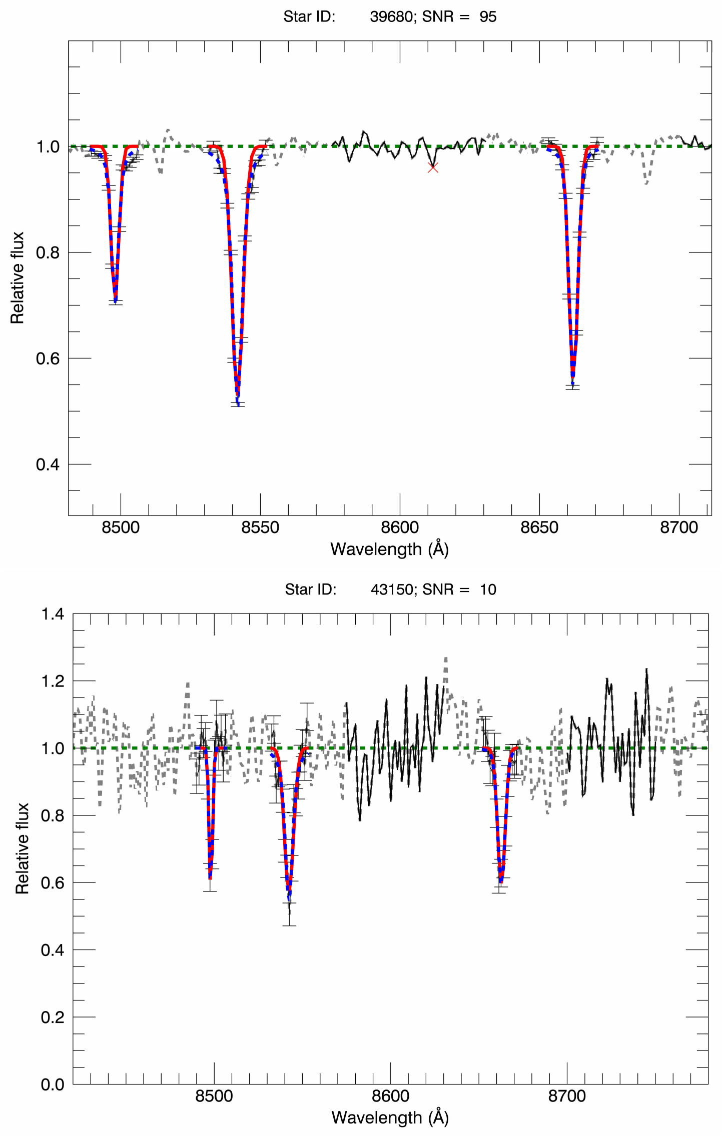

Figure 2.8 Fitting examples of Voigt (dashed red line) profiles to the CaII triplet lines for two spectra. Top: Example of high-S/N to noise spectrum ($S/N = 95$). Bottom: example of low-S/N spectrum ($S/N = 10$).

et al. (2010b) using neutral Fe lines of 76 stars. The vertical black line to the right shows the average metallicity for 25 metal-rich stars ($[Fe/H] = -0.622 \pm 0.068$ dex) estimated by the same authors. We see consistent results between our metallicity measurements using full spectral fitting with ULySS (Koleva et al., 2009) and the measurement by Carretta et al. (2010b) for the metal-poor stars. For the metal-rich population we see a difference in the average metallicity, our peak a more metal-rich ($[Fe/H] \sim -0.3$ dex). We give a possible explanation for this difference in Section 2.3.1. The bottom panel shows the correlation of the metallicity values between the two methods, where we see a bigger difference in the high-metallicity regime. The estimates are plotted in blue for the spectra with S/N$>$ 60 and in gray for S/N$<$ 60.

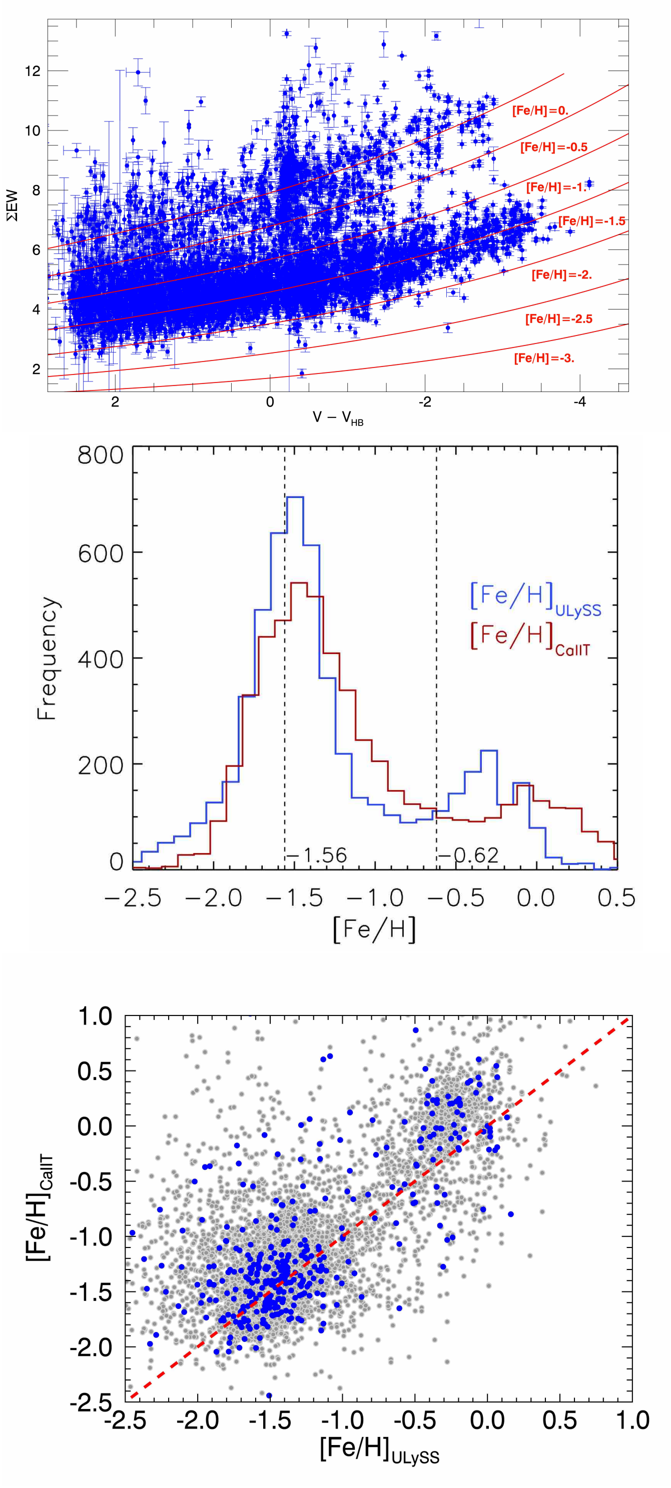

Figure 2.9 Top panel: Equivalent width sum of the three CaII triplet lines versus $V - V_{HB}$. Overplotted in red lines are the metallicity values for the Carrera calibration using the spectral ranges of the CaII triplet lines defined by Armandroff & Zinn (1988). Middle panel: Metallicity histogram of the values obtained with the CaII triplet lines method using the calibration published by Carrera et al. (2013, red) and those obtained performing full spectral fitting using ULySS (Koleva et al., 2009, blue) for the same stellar sample. There are fewer stars in the first method since it is restricted to RGB stars ($\sim$4 000). From left to right the vertical black lines show the average metallicity for the metal-poor and metal-rich stars estimated by Carretta et al. (2010b). Bottom panel: Correlation of the metallicity values obtained with the two methods, for spectra with $S/N > 60$ in blue and $S/N < 60$ in gray.

2.2.4 Comparison for Multiple Stellar Spectra Measurements

In Section 2.1.2 we describe the stellar spectra extraction from the MUSE dataset. Due to overlaps between the neighboring pointings, we have from one up to four spectra for an individual star. To compare how the velocity, metallicity, and their respective uncertainties are correlated, we include the comparison between the velocity estimates for the complete extracted stellar sample (see Section 2.2.1). The top left panel in Figure 2.10 shows velocity versus velocity measurements of the repeated stars. We show the same for their corresponding errors in the middle left panel. The bottom left panel shows the histogram of the difference in the measurements. The estimated sigma is $\sigma = 16.25\,\mathrm{km\ s}^{-1}$. The right panels of Figure 2.10 include the same comparison for the case of the metallicity measurements described in Section 2.2.3.1 for the same stellar sample. The top right panel of Figure 2.10 shows metallicity versus metallicity measurements of the repeated stars. The correlation between their respective errors is shown in the middle right panel. The bottom left panel shows the histogram of the difference in the measurements, with a sigma of 0.51 dex.

Since brighter stars have higher S/N, to show the variation of the spread in dependency with magnitude, in Table 2.1 we include the standard deviation of the [Fe/H] and LOS velocity measurements at different magnitude cuts.

The difference in the values for both parameters can be due to the different observing conditions during the acquisition of the 16 pointings (between June and July 2015). This produces variations in the quality of the spectra. In spite of this, we extracted good-quality spectra with a reasonable S/N threshold of 10. The dispersion we observe between repeated stars is acceptable and does not affect our main results.

2.2.5 Stellar Age Estimates

Valuable information about the SFH of the Sgr dSph NSC can be obtained from age and metallicity estimates together. For the age estimates of individual stars we use a grid of isochrones, which we compare with the magnitudes and colors of the stars as measured from the *HST* photometry in V (F606W) and I (F814W) bands with their respective uncertainties (σ_V, σ_I), and metallicities Z, obtained from the MUSE spectra, including their uncertainties σ_Z. We set the metallicity uncertainty to 0.1 dex when lower than that value. We consider age the only free parameter of the model.

We use Bayes's theorem to estimate the ages through the posterior probability as:

$$P(\tau\,|\,V_{\mathrm{obs}},I_{\mathrm{obs}},Z_{\mathrm{obs}}) \propto P(V_{\mathrm{obs}},I_{\mathrm{obs}},Z_{\mathrm{obs}}\,|\,\tau) \times P(\tau), \tag{2.2}$$

where the normalized likelihood function $P(V_{\mathrm{obs}},\, I_{\mathrm{obs}},\, Z_{\mathrm{obs}}|\tau)$ of the observables at a given age is a trivariate Gaussian:

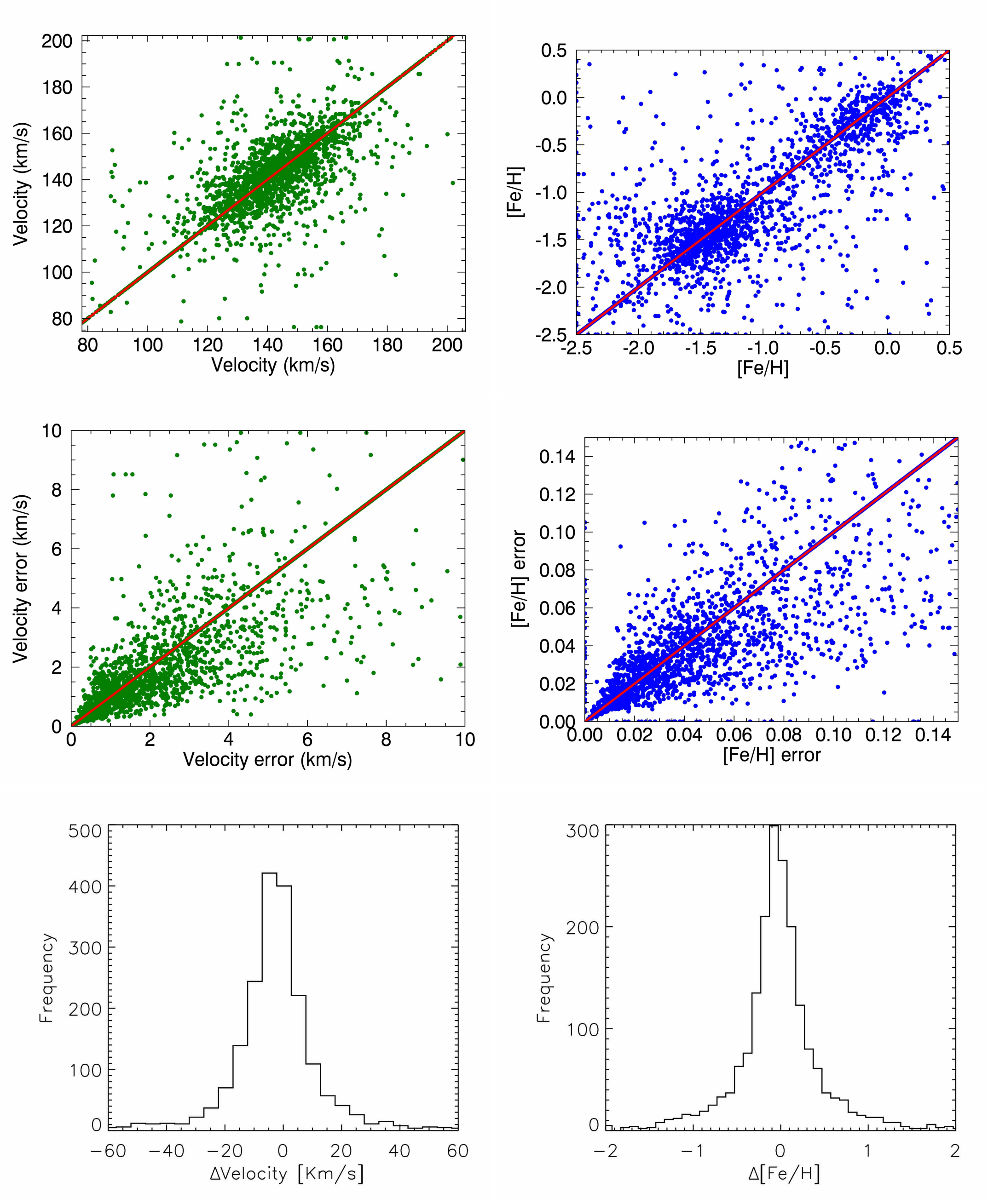

Figure 2.10 Top left panel: velocity measurements' correlation of the repeated stars. Middle left panel: correlation between the uncertainties. Bottom left panel: histogram of the difference in the measurements, with $\sigma = 16.25\,\mathrm{km\,s^{-1}}$. Top right panel: shows metallicity measurements' correlation of the repeated stars. Their respective errors' correlation is shown in the middle right panel. Bottom left panel: histogram of the difference in the measurements, with $\sigma = 0.51$ dex.

Table 2.1. Line-of-sight velocity and [Fe/H] spread for repeated stars.

Imag Range	$\sigma_{\mathrm{V_{LOS}}}$ (km s^{-1})	$\sigma_{\mathrm{[Fe/H]}}$	Number of Stars
$[13-14)$	5.84	0.19	55
$[14-15)$	12.75	0.40	135
$[15-16)$	13.12	0.51	235
$[16-17)$	16.83	0.54	425
$[17-18)$	17.78	0.54	430
$[18-19)$	12.30	0.47	324
$[19-20)$	16.87	0.50	236
$[20-21)$	29.51	0.58	68
$[21-22)$	30.75	0.42	6
$[13-22]$	16.25	0.51	1920

Note. — σ corresponds to the spread given by the standard deviation of the measurements from the repeated stars at different magnitude cuts.

$$
\begin{aligned}
P(V_{\mathrm{obs}}, I_{\mathrm{obs}}, Z_{\mathrm{obs}} \,|\, \tau) = & \frac{1}{\sigma_{V_{\mathrm{obs}}}\, \sigma_{I_{\mathrm{obs}}}\, \sigma_{Z_{\mathrm{obs}}}\, (2\pi)^{3/2}} \times \exp \frac{-(V_{\mathrm{obs}} - V_0)^2}{2\sigma^2_{V_{\mathrm{obs}}}} \\
& \times \exp \frac{-(I_{\mathrm{obs}} - I_0)^2}{2\sigma^2_{I_{\mathrm{obs}}}} \times \exp \frac{-(Z_{\mathrm{obs}} - Z_0)^2}{2\sigma^2_{Z_{\mathrm{obs}}}},
\end{aligned}
\tag{2.3}
$$

where V_0, I_0, and Z_0 denote the real magnitudes and metallicity of the star given its age and the σ values represent the independent errors in each measurement. We marginalize over the unknown true magnitudes and metallicity of the star by integrating over the isochrones (see, e.g., Pont & Eyer, 2004, for a similar approach).

Due to the lack of extended horizontal branch isochrone models, we have excluded stars with colors between $V - I = -0.2$ and 0.4 and I in the range of 21 to 17 in our age analysis.

Initially, we used a flat prior in age $P(\tau)$ for all the remaining stars. The age-metallicity relation (AMR) found for the TO region stars turned out to be very well represented by the empirical model published by Layden & Sarajedini (2000). On the other hand, the obtained ages for a fraction of metal-poor RGB stars were lower than expected for such a metallicity regime. This degeneracy could be a consequence of high abundance of elements like oxygen, which has been reported to display a high spread in this metal-poor population (Carretta et al., 2010b). In fact, VandenBerg et al. (2012) showed the impact of different elements abundances on computed evolutionary tracks at similar [Fe/H] values and how this affects the color of the stars and thus their position in the CMD. After this examination of the initial ages, to guard against systematic age uncertainties, we set a weak Gaussian age prior $P(\tau)$ to their model with a standard deviation of 3 Gyr for the age estimates of all extracted member stars from the MUSE cube.

We built the isochrone grid with a resolution of 0.2 Gyr with ages from 0.2 to 15 Gyr from the Dartmouth Stellar Evolution Database (Dotter et al., 2008) assuming the *HST*/ACS WFC photometric system. The metallicity range is from -2.495 to 0.500 dex with steps of 0.005 dex, considering $[\alpha/\mathrm{Fe}] = 0.0$. We correct the isochrone magnitudes by extinction of $\mathrm{A}_V = 0.377$ and $\mathrm{A}_I = 0.233$ from NED[2]. These are obtained using the calibration published by Schlafly & Finkbeiner (2011) for the F606W and F814W bands for a reddening of $E(B-V) = 0.15$ estimated in the central $5\overset{\prime}{.}0$ radius of M54 (Schlegel et al., 1998) with $R_V = 3.1$. We shifted the grid of isochrones adopting a distance modulus of $(m-M_0) = 17.27$ (Siegel et al., 2007). For comparison, we performed the same analysis considering a reddening of $E(B-V) = 0.16$ and a distance modulus of $(m-M_0) = 17.13$ (Sollima et al., 2010), obtaining consistent age estimates. We take the mode of the likelihood distribution of ages as the best age estimate and the highest density interval that accommodates 68% of the probability as the age uncertainty.

The CMD for the clean stellar sample color-coded by age (hereafter CMD+age) is presented in the top panel of Figure 2.11, with a zoom-in of the TO region in the bottom panel of the figure. Three isochrones based on those presented in Siegel et al. (2007) are overplotted; they are also from the Dartmouth Stellar Evolution Database (Dotter et al., 2008).

2.2.6 Populations Split by Age and Metallicity

We use Gaussian Mixture Models (GMMs) in age-metallicity space to separate the stars into distinct multiple populations. To this aim, we used only TO region stars, where we obtain the most reliable age estimates as we describe in Section 2.2.5. We tested GMMs with three, four, and five components and found that a GMM with four components gives the best representation of our data set based on the Akaike Information Criterion (Akaike, 1974). We optimized the GMM using the affine-invariant Markov chain Monte Carlo (MCMC) algorithm (Goodman & Weare, 2010; Foreman-Mackey et al., 2013). We then computed the probabilities of all stars[3] in the observed sample of belonging to any of the GMM defined populations. The fourth Gaussian component of the GMM captures outliers and is not further considered in our analysis.

We estimate the mean and spread in both age and metallicity for each of the subpopulations. We start by taking stars with a high probability ($> 50\%$) of belonging to each subpopulation. Then, we perform a maximum likelihood fit for the ages and metallicities of these stars using a two-dimensional Gaussian and accounting for the observational uncertainties in each stars' age and metallicity. The result is a mean and intrinsic spread in both age and metallicity for each population. We assumed that the [Fe/H] probability distribution functions (pdf's) are Gaussian

---

[2] The NASA/IPAC Extragalactic Database (NED) is operated by the Jet Propulsion Laboratory, California Institute of Technology, under contract with the National Aeronautics and Space Administration.

[3] From here we consider all stars those with ages consistent with the current age of the universe, age $\leqslant$ 14 Gyr.

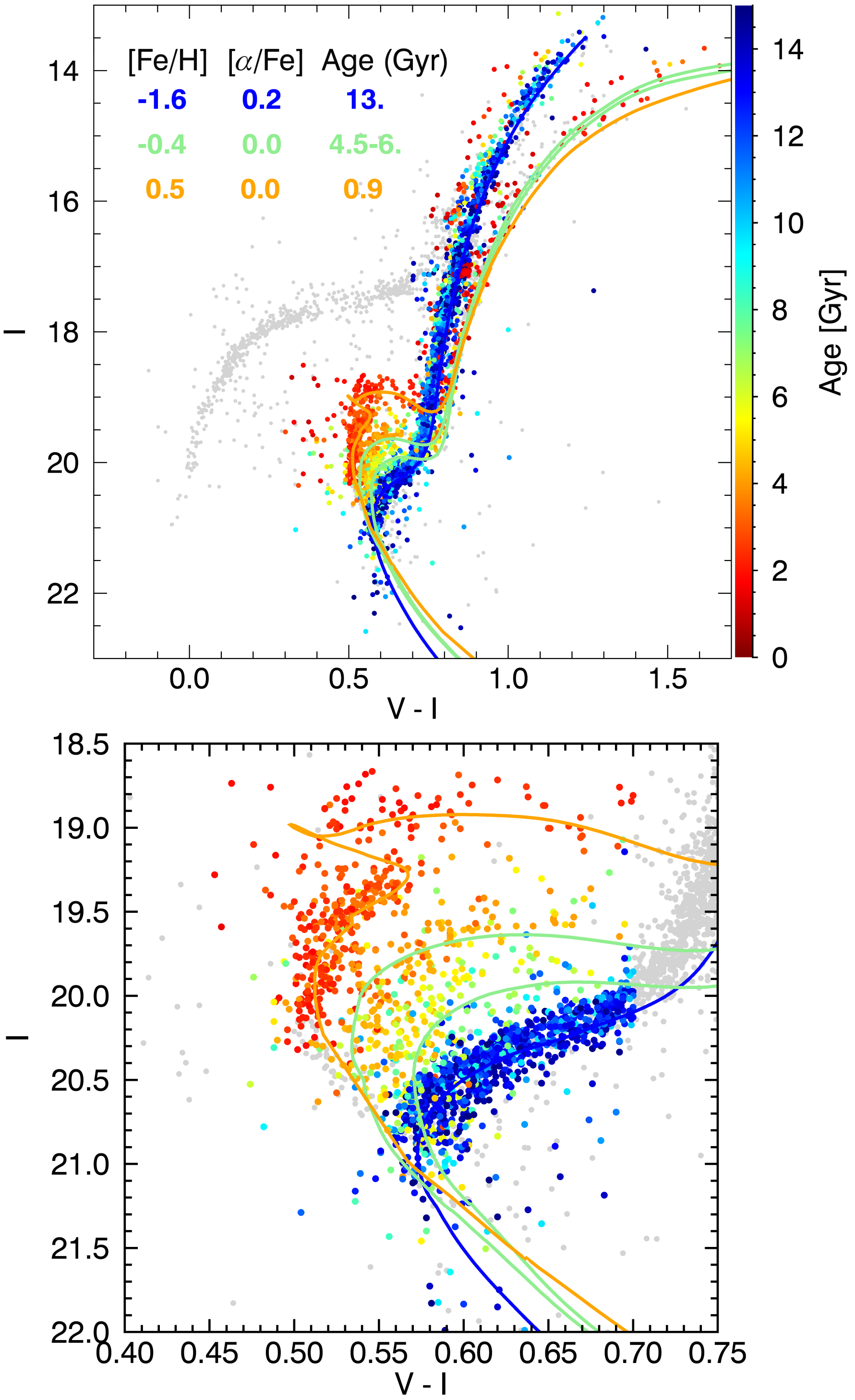

Figure 2.11 Top panel: CMD for the Sgr dSph NSC members color-coded by age (CMD+age). Bottom panel: Zoom-in of the TO region. Updated isochrones from the Dartmouth Stellar Evolution Database are overplotted in blue, green, and orange for three stellar populations published by Siegel et al. (2007).

and integrated numerically over the non-Gaussian individual stellar age pdf's. From the results of this procedure we define three different subpopulations as follows:

- YMR: young metal-rich (red).
  With mean age of 2.16 ± 0.03 Gyr and mean $[\mathrm{Fe/H}] = -0.04 \pm 0.01$.
- IMR: intermediate-age metal-rich (orange).
  With mean age of 4.28 ± 0.09 Gyr and mean $[\mathrm{Fe/H}] = -0.29 \pm 0.01$.
- OMP: old metal-poor (blue).
  With mean age of 12.16 ± 0.05 Gyr and mean $[\mathrm{Fe/H}] = -1.41 \pm 0.01$.

We find that the YMR population has an intrinsic 1σ spread of 0.20 ± 0.03 Gyr in age and 0.12 ± 0.01 dex in metallicity; the IMR population has an intrinsic spread of 1.16 ± 0.07 Gyr in age and 0.16 ± 0.01 dex in metallicity; the OMP population has an intrinsic spread of 0.92 ± 0.04 Gyr in age and 0.24 ± 0.01 dex in metallicity. The uncertainties are represented by the standard deviation in each parameter in the converged part of the MCMC, thus obtaining low errors. The age-metallicity correlation coefficients, ρ, for the three populations are $\rho_{\mathrm{YMR}} = -0.35$, $\rho_{\mathrm{IMR}} = -0.70$, and $\rho_{\mathrm{OMP}} = -0.97$.

To check for consistency, we use the same method to estimate the intrinsic spread in metallicity for stars with $I \leqslant 16.5$ mag, where the S/N of the stars is mostly > 100. This leaves a total of 22 stars for the YMR (5% of YMR sample) and 208 for the OMP ($\sim 9\%$ of OMP sample). For the YMR subpopulation we obtain an intrinsic 1σ spread of 0.11 ± 0.06 dex, and 0.13 ± 0.03 dex for the OMP subpopulation. The spread for the YMR subpopulation derived from the brightest stars is consistent with the one measured for the stars of all magnitudes. For the OMP subpopulation, we observe a difference of 0.11 dex. This can be a consequence of the low number of stars in comparison with the entire sample and the effects of the age uncertainties at the RGB region, which can be more uncertain, as we mention in the previous section. Since these values are obtained from a reduced fraction of the entire sample ($< 10\%$), we will consider the intrinsic spread measured from the sample at all magnitudes.

The AMR is presented in Figure 2.12, where we include all stars for which ages were measured and have relative age errors $\leq 40\%$. The overplotted crosses represent the intrinsic spreads of the different populations: YMR in red, IMR in orange, and OMP in blue. The intrinsic age and metallicity spreads, together with the age-metallicity correlation coefficient ρ define the inclination angle of the crosses for each subpopulation. We discuss the possible origin of these populations in Section 2.4.

For the RC stars in the sample we were able to obtain reliable measurements in metallicity and found that they all fall in the metal-rich regime. The complexity of this stage of stellar evolution prevents us from getting reliable ages for the RC stars from simple isochrone fits. Due to this effect, the RC stars were not considered to belong to any of the subpopulations when we decompose the stars into subpopulations via the maximum likelihood method. For completeness,

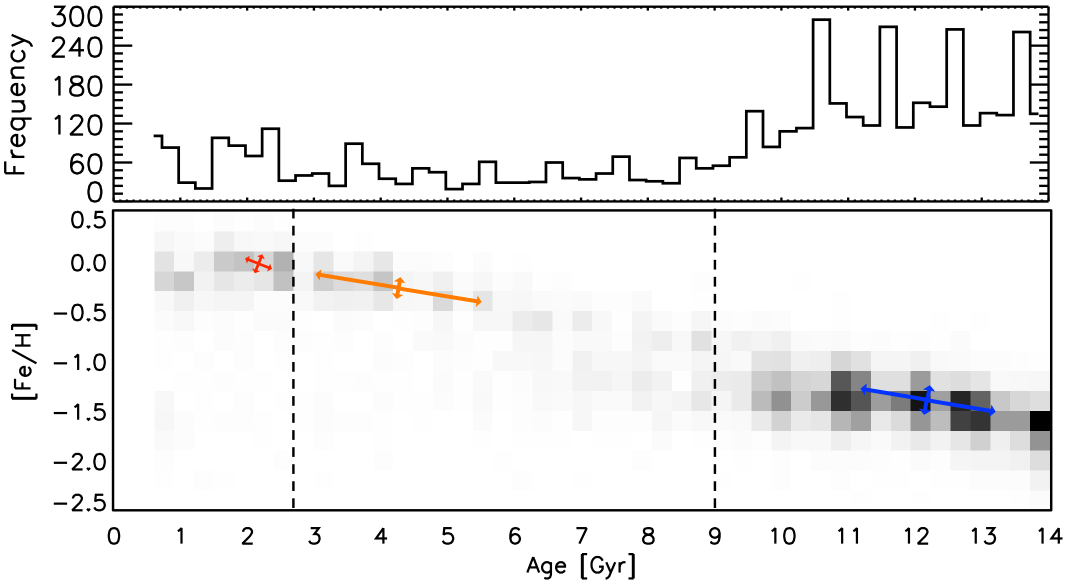

Figure 2.12 Top: age histogram. Bottom: density plot of the age-metallicity relation. The crosses show the intrinsic spread of the different stellar populations in the Sgr dSph NSC: young metal-rich (YMR) in red, intermediate-age metal-rich (IMR) in orange, and old metal-poor (OMP) in blue. The subpopulations's stellar parameters are summarized in Table 2.2. All the stars included in both panels have age relative errors $\leqslant$40%. The vertical dashed lines show where the probability is equal for the two neighbouring subpopulations. Note: the inclination of the crosses is given by the correlation coefficient obtained from the Gaussian mixture model.

these stars are shown in Figure 2.12 and fall on the diagram clustered together as the overdensity at ∼1 Gyr in a metallicity range of $-0.5 < [\mathrm{Fe/H}] < 0.0$. To get a better estimate of the likely age distribution of RC stars, we follow Girardi (2016) and compute the RC age distribution for representative SFHs of Sagittarius. We do this for two assumptions of the SFH: (i) the Sgr dSph has a constant SFH, and (ii) the SFH follows the observed SFH from the CMD analysis of de Boer et al. (2015). The de Boer et al. (2015) SFH shows a declining SFR with time but is constructed from the tail of the Sgr dSph, so it is likely missing the most metal-rich and young stars – biasing the star formation to early times. Inclusion of the younger populations in the CMD analysis might produce a SFH more closely represented by a constant SFH. We therefore consider these two cases as plausible bounds on the likely true SFH of Sgr. For the constant SFH case we find that the RC stars are predominantly (∼ 51%) younger than 2.2 Gyr, thus being more likely to belong to the YMR subpopulation than to the IMR (10%.) For case (ii), we obtain that anywhere from 10% to 70% of RC stars are younger than 2.2 Gyr, with probabilities of less than 10% for the IMR. Taking these two cases into consideration, we consider it most likely that the majority of the RC stars are associated with the YMR subpopulation, and we consider them as part of that population in our further analysis.

2.3 Results

2.3.1 Population Analysis

Comparing the metallicity and age information presented in the CMDs in Figure 2.6 and 2.11, we observe that in the TO region in the CMD+age we distinguish three well separated subpopulations with different age ranges. The faintest stars have ages over 9 Gyr. This subpopulation belongs to the metal-poor regime in the CMD+metallicity. The middle subgiant branch population has ages of $\sim 3-9$ Gyr, while the brightest stars have ages younger than 3 Gyr. These last two populations belong to the metal-rich regime in the CMD+metallicity. From the CMD+metallicity figure, some small difference in metallicity (~0.3 dex) is also visible between these two younger populations.

In the CMD+metallicity the metal-poor RGB is well defined by stars with metallicity below $[\mathrm{Fe/H}] = -0.8$, displaying a wide range toward $[\mathrm{Fe/H}] = -2.5$, corresponding to an intrinsic iron spread of $\sigma_{[\mathrm{Fe/H}]} = 0.24$ dex. In addition, we observe that the stars in the BP region between $18.5 \leqslant I \leqslant 20.5$ and $0.1 \leqslant V-I \leqslant 0.5$ show a wide range in metallicity (from -2.0 to 0.5). We discuss this further in Section 2.4.3.

From the CMDs (Figures 2.6, and 2.11) and the AMR (Figure 2.12), we can decipher the SFH of the Sgr dSph NSC. It appears to be extended from 0.5 to 14 Gyr, showing a clear metallicity enrichment toward younger stars.

We present a CMD comparing the three subpopulations in Figure 2.13. In both panels the subpopulations are represented as follow: YMR in red, IMR in orange, and OMP in blue. In the top panel we can see how the different populations fall in different positions in the CMD; this is easier to see in the zoom-in of the TO region shown in the bottom panel.

Our findings are in good agreement with the characteristics of three (of four) subpopulations obtained with isochrone fitting by Siegel et al. (2007), and later also by Mucciarelli et al. (2017). From their fitting of the CMD, Siegel et al. (2007) suggest the presence of four populations: (i) the old metal-poor population, with ages of 13 Gyr and $[\mathrm{Fe/H}] = -1.8$; (ii) the intermediate-age metal-rich population, with ages between 4 and 6 Gyr and $[\mathrm{Fe/H}] = -0.6$; (iii) the young metal-rich population with 2.3 Gyr and $[\mathrm{Fe/H}] = -0.1$; and (iv) the very young, very metal-rich population with $[\mathrm{Fe/H}] = 0.6$ and ages $0.1-0.8$ Gyr. We do not detect any stars belonging to their fourth population.

We do find a higher mean metallicity for the metal-rich regime population compared to Carretta et al. (2010b) and Mucciarelli et al. (2017). This may be due to several factors. First, we separate the metal-rich stars into two subpopulations, with the YMR having significantly higher mean metallicity than the IMR; the latter, older stars have metallicity closer to previous measurements. Second, our spatial coverage is confined to much smaller radii in comparison to Carretta et al. (2010b) and Mucciarelli et al. (2017), which cover out to a larger radius. Third, the resolution of our data allow us to extract more stars from the most crowded central regions.

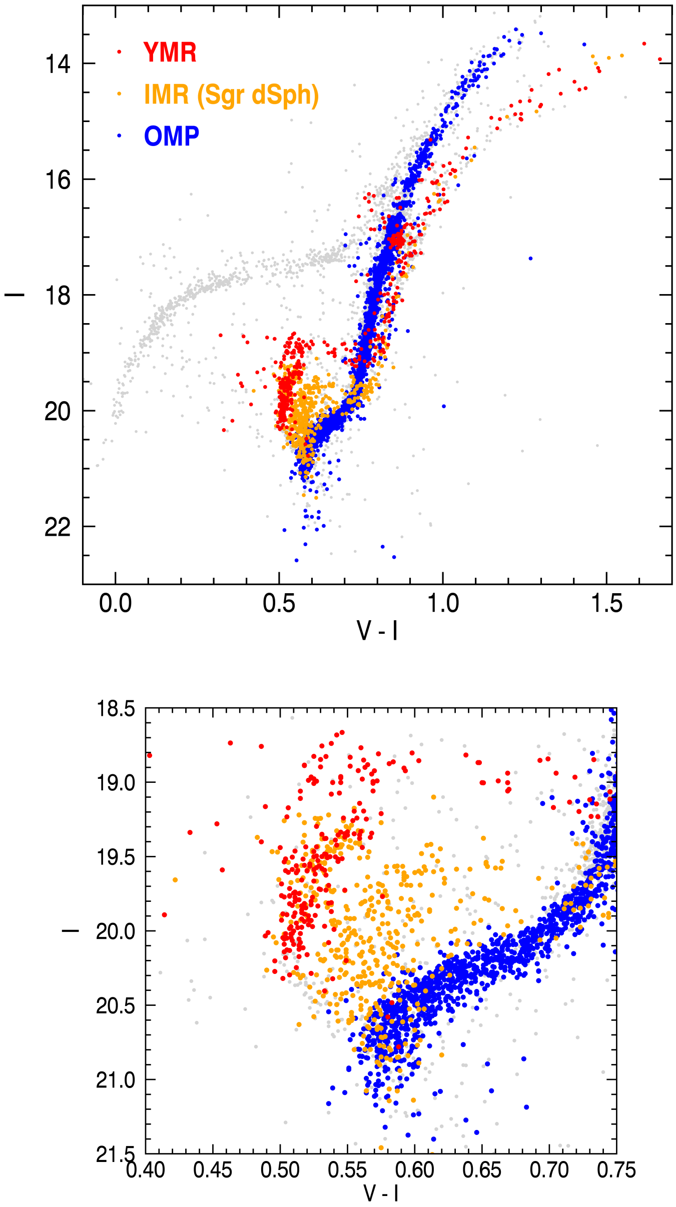

Figure 2.13 For the two panels: red points represent the YMR subpopulation (2.2 Gyr, [Fe/H] = −0.04), orange points for the IMR (4.3 Gyr, [Fe/H] = −0.29), and blue points are for the OMP (12.2 Gyr, [Fe/H] = −1.41). Gray points show the stars with age relative error greater than 40% or for which age was not estimated. Top panel: CMD. Bottom panel: zoom-in of the top panel showing just the TO region.

Table 2.2. Summary of the stellar Subpopulations in M54.

Subpopulations	YMR	IMR	OMP
[Fe/H]	-0.04 ± 0.01	-0.29 ± 0.01	-1.41 ± 0.01
$\sigma_{[\mathrm{Fe/H}]}$	0.12 ± 0.01	0.16 ± 0.01	0.24 ± 0.01
Age (Gyr)	2.16 ± 0.03	4.28 ± 0.09	12.16 ± 0.05
σ_{Age} (Gyr)	0.20 ± 0.03	1.16 ± 0.07	0.92 ± 0.04
ρ	-0.35	-0.70	-0.97
Median V_{LOS} (km s^{-1})	141.92 ± 0.54	142.61 ± 0.59	141.22 ± 0.26
R.A. Centroid (deg)	283.76351 ± 0.00176	*	283.76299 ± 0.00094
Decl. Centroid (deg)	-30.476992 ± 0.000977	*	-30.477067 ± 0.000673
R$_{\mathrm{HL}}$ (arcmin)	1.47 ± 0.20	*	1.90 ± 0.12
Ellipticity	0.31 ± 0.10	*	0.16 ± 0.06
PA (rad)	4.23 ± 11.14	*	16.43 ± 13.75
Number of stars	440	536	2550

Note. — *: Measurements do not converge. $\sigma_{[\mathrm{Fe/H}]}$ and σ_{Age} correspond to the [Fe/H] and age intrinsic spreads, respectively. ρ: Correlation factor. V_{LOS}: Line-of-sight velocity. R$_{\mathrm{HL}}$: Hal-light radius. PA: position angle. The correlation factor (ρ) indicates how age and metallicity are correlated and is estimated using Gaussian Mixture Models.

Fourth, on average, our metallicity estimates are slightly higher. We obtain a mean Δ[Fe/H] of 0.15±0.03 dex when comparing with Carretta et al. (2010b), and 0.05±0.02 dex with Mucciarelli et al. (2017).

In Table 2.2 we include a summary of all the estimated parameters for the subpopulations.

2.3.2 Subpopulation Spatial Distributions

We now analyze the spatial distribution of the three subpopulations in the Sgr dSph NSC defined in the previous section. In Figure 2.14 we present the cumulative radial distribution for the three subpopulations: YMR (red), IMR (orange), and OMP (blue). We consider all the member stars extracted with $\mathrm{S/N} \geqslant 10$. In order to fairly compare the three subpopulations distribution in terms of completeness, we also constrain the sample to magnitudes $I \leqslant 20.5$ mag.

In Figure 2.14 we observe that the YMR subpopulation is the most centrally concentrated of the three in this NSC. The second highest central density is shown by the OMP subpopulation, which is the dominant one in stellar number with over 2 000 stars. Finally, the lowest central concentration is shown by the IMR subpopulation. Comparing the distribution of these subpopulations with a uniform distribution (magenta dashed line), we observe that the stars in the IMR subpopulation are the least centrally concentrated in the most central 40.″ However, they are still not uniformly distributed; as we observed in Figure 2.14, the distribution shows that the

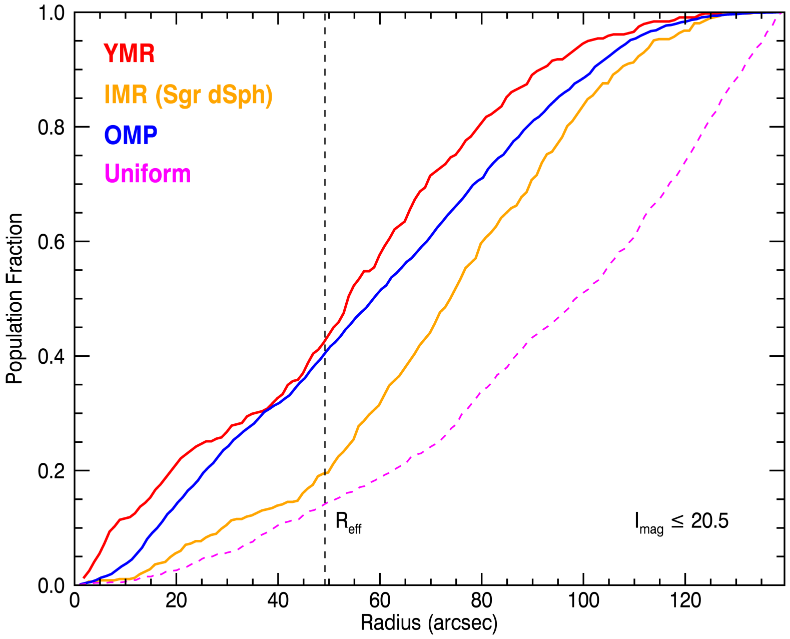

Figure 2.14 Cumulative radial distribution for the three subpopulations for the member stars extracted with $S/N \geqslant 10$ and $I \leqslant 20.5$ mag. YMR subpopulation in shown in red (2.2 Gyr, $[Fe/H] = -0.04$), IMR in orange (4.3 Gyr, $[Fe/H] = -0.29$), and OMP in blue (12.2 Gyr, $[Fe/H] = -1.41$). The magenta dashed line describes a uniform stellar distribution. The vertical black dashed line shows the half-light radius of M54 ($R_{HL} = 0.'82$, Harris, 1996, 2010 edition).

stars in the IMR subpopulation are still significantly centrally peaked. This difference in the spatial distribution between the subpopulations suggests different origins. We discuss this in detail through Section 2.4.

It is important to consider that, due to extreme central crowding and the limitations of our spatial resolution, we are not able to extract all the stars that actually reside in this NSC. Improved spatial resolution is needed to more accurately derive the spatial distribution of the different stellar populations.

2.3.3 2D Morphology of Subpopulations

Using the coordinate information of the stars and the data FOV, we fit a two-dimensional Plummer profile (Plummer, 1911) to each of the subpopulations, optimizing the best profile using a MCMC algorithm (Goodman & Weare, 2010; Foreman-Mackey et al., 2013). We set the centroid, ellipticity, position angle (PA), and half-light radius as free parameters, thus obtaining the best estimates for each stellar subpopulation.

The estimated parameters are summarized in Table 2.2. The likelihoods for the YMR and OMP populations converge and give good estimates for the centroid, ellipticity, and PA. However, for the IMR it does not converge due to the less centrally concentrated distribution that this subpopulation shows (see Section 2.3.2).

2.4 Discussion

We show the systemic velocities of the three subpopulations in Table 2.2. The difference of $\sim 1\sigma$ to 2σ between them could be a consequence of the number of stars in each sample, which is considerably higher for the OMP, with ~5 times more stars than the YMR and IMR subpopulations. This results in lower errors for the OMP. In spite of the slight difference, the velocities are consistent. The nearly identical systemic velocities derived from a high number of stars strongly support the idea that all three subpopulations are spatially coincident, as also suggested in previous studies (e.g., Da Costa & Armandroff, 1995; Ibata et al., 1997; Monaco et al., 2005a; Bellazzini et al., 2008). We also add another piece of evidence to this with their respective centroids (Table 2.2), showing that the subpopulations OMP and YMR are actually spatially coincident with the same centroid. This strongly argues against a chance alignment in projection between the metal-poor and metal-rich populations (Siegel et al., 2011).

2.4.1 A Possible Merger Remnant as the Seed of the Sgr dSph NSC

We find that the stars in the metal-poor regime show a large spread in age, $\sigma_{\rm age} = 0.9$ Gyr, and iron content, $\sigma_{\rm [Fe/H]} = 0.24$, a higher spread in comparison with the literature ($\sigma_{\rm [Fe/H]} = 0.186$; Carretta et al. 2010c; Willman & Strader 2012). Large iron spreads in GCs can be explained by a scenario in which two GCs merge (Gavagnin et al., 2016; Bekki & Tsujimoto, 2016; Khoperskov et al., 2018, and references therein).

Gavagnin et al. (2016), using N-body simulations studied the structural and kinematic signatures in the remnants of GC mergers with a sample of progenitors of different densities and masses. They pointed out that if two GCs were formed in the same dwarf galaxy (or molecular cloud) and display a low relative velocity, they could merge, making the merging scenario more likely in dwarf galaxies. They actually mention the Sgr dSph as a good candidate for this scenario to happen. Bellazzini et al. (2008) found that the velocity dispersion profile is close to flat, with values of $\sim 10\,\rm km\ s^{-1}$ in the innermost 80 arcmin.

Bekki & Tsujimoto (2016) used numerical simulations to suggest that GC mergers explain the existence of complexity in high-mass GCs, with multiple stellar populations and a large spread in metallicity, what the authors called “anomalous” GCs. Performing several tests, Bekki & Tsujimoto (2016) found that the merger between GCs with masses greater than $3\times10^5 M_\odot$ will occur inevitably in the host dwarf galaxy, with a mass in the range of $M_{dh} = 3\times10^9 - 3\times10^{10} M_\odot$. This is due to a stronger dynamical friction effects on the GCs compared to the field stars in those shallow, low-dispersion galaxies. The authors mention that if the clusters are massive enough, the timescale for the merger is just a few gigayears, and it occurs before the total disruption of the dwarf galaxy due to the Galactic tidal field. They find that with a merger of at least two GCs it would be possible to observe GCs with an internal metallicity spread. In the case of the Sgr dSph, the progenitor dark halo mass before infall to the Milky Way has been estimated with a lower limit of $6\times10^{10} M_\odot$ by Gibbons et al. (2017), in good agreement with

Mucciarelli et al. (2017). The mass estimated for M54 is $(1.41 \pm 0.02) \times 10^6 M_\odot$ (Baumgardt & Hilker, 2018), consistent with mergers of GCs of $10^5 M_\odot$.

The merger scenario might explain the high mass and the large iron and age spreads in the OMP subpopulation. The mass of the Sgr dSph progenitor would be conducive for the GCs to merge. From simulations, the infall of a massive GC to the center of the Sgr dSph due to dynamical friction effects has been estimated to have occurred $\sim 5-9$ Gyr ago (Bellazzini et al., 2006a, 2008). The infall time is at most 3 Gyr (Bellazzini et al., 2008) for a cluster with M54's mass. The spread in age and metallicity of the oldest, metal-poor stars is consistent with the scenario where multiple GCs were driven to the center of the Sgr dSph and merged, thus building up the metal-poor component of the NSC.

2.4.2 In-situ Formation in the Sgr dSph NSC: YMR Subpopulation

From the metallicity and age characterization of our stellar sample we distinguish two subpopulations in the metal-rich regime. We are able to separate them using the AMR and CMD position of the stars. We observe that the youngest population – YMR – has the highest central density in the Sgr dSph NSC. The high metallicity, young age, and spatial distribution suggest that the formation of the YMR subpopulation formed in situ starting $\sim$3 Gyr ago.

Additional evidence for in-situ formation of the YMR population is that it appears more flattened than the OMP population. We measure an ellipticity of 0.31 ± 0.10 for the YMR component, while the OMP population has an ellipticity of 0.16 ± 0.06 (Table 2.2). Centrally concentrated and sometimes flattened young subcomponents are commonly found in other NSCs in both early- and late-type galaxies (Seth et al., 2006; Carson et al., 2015; Feldmeier-Krause et al., 2015; Nguyen et al., 2017); given the young age of these populations, in-situ formation is strongly favored, with the flattening suggestive of formation in a star forming gas disk. We note that the difference in ellipticity between the YMR and OMP subpopulations is small, given the measurement uncertainties. However, this difference becomes meaningful when we combine the ellipticity with the kinematics. In Chapter 3 we will present the kinematic characterization of the subpopulations, adding a new diagnostic to address this issue.

These young, flattened populations can survive despite being embedded in an older, hotter population. Mastrobuono-Battisti & Perets (2013, 2016) modeled the evolution of stellar disks in dense stellar clusters using N-body simulations, finding that even after several gigayears (around the Milky Way GC's age) the stars are still not fully mixed. Thus, both generations of stars show different distributions. They observed that the second population is concentrated at the center after 12 Gyr with no relaxed spherical shape. The amount of rotation is also evidence for this model, where the second generation of stars is found to rotate faster than the first one. From our kinematic analysis, we found that the YMR subpopulation rotates faster than the OMP. We will present the evidence on this matter in the next chapter.

To form the youngest and metal-rich subpopulation enriched gas is needed; however, no neutral gas has been detected in this galaxy. Using simulations, Tepper-García & Bland-Hawthorn (2018) found that the Sgr dSph might have lost all its gas after the second encounter with the Galactic disk. They found that two pericentric passages happened $\sim$2.8 and $\sim$1.3 Gyr ago. The first produced a gas loss of 30% to 50%, while the second would be responsible for the stripping of all the residual gas. The timescales of both encounters are consistent with the latest bursts of star formation seen in Figure 2.12 and were suggested based solely on the photometry by Siegel et al. (2007). This suggests that the YMR population may have formed by gas being driven into the nucleus during encounters with the Milky Way, supporting the in-situ formation of this population.

The in-situ formation of a new generation of stars could alternatively be explained for a massive NSC with a deep enough potential well to collect the enriched gas ejected from metal-rich and high-mass stars at larger radii that cools and sinks to the center (Bailey, 1980). This seems plausible given the characteristics of the stars in the IMR subpopulation and the relatively small fraction of YMR stars in comparison with the OMP.

2.4.3 Sgr dSph Field Stars in Its NSC: IMR Subpopulation

A different situation is observed for the IMR population in comparison to the YMR. These stars seem to be less centrally concentrated in the field, with a wide spread in ages from 3 to 8 Gyr. These findings suggest that the star formation in the Sgr dSph during this period was not particularly concentrated in the nucleus. The metallicity range of these stars is consistent with those found for stars close to the center of the galaxy (Hasselquist et al., 2017). In addition, comparing the IMR sample of our AMR (Figure 2.12) with the one presented by de Boer et al. (2015) for the Sagittarius bright stream, we see a good agreement in both age ($4-14$ Gyr) and metallicity ($-2.5 < \text{[Fe/H]} < -0.1$), thus, supporting our good recovery of the underlying chemical evolution of the host galaxy.

The spatial distribution of these two subpopulations – YMR and IMR – has also been reported by Mucciarelli et al. (2017). Using a sample of 109 stars with $\text{[Fe/H]} \geqslant -1.0$ and a magnitude limit of $I_{\text{mag}} = 18$, the authors observed a shift in the metallicity peak in the metal-rich population at different projected distances from its center. At $0\farcm0 < \text{R} < 2\farcm5$ the peak is at $\text{[Fe/H]} = -0.38$, changing to $\text{[Fe/H]} = -0.45$ at $2\farcm5 < \text{R} < 5\farcm0$, noticing a metallicity gradient for this population. In addition, the authors present the cumulative radial distribution of the two young populations where they found that the youngest subpopulation is more centrally concentrated than the intermediate-age population. With this finding they suggest that the youngest population is the dominant population in the Sgr dSph NSC, with the intermediate-age one becoming more important at larger radii. Since our observations reach out to $\sim 2\farcm0$ from the center of this NSC, we are not able to see a change in the peak at larger radii. However, we also see this behavior between the two youngest metal-rich subpopulations.

Our spectroscopic sample also includes stars in the BP region, which could be populated by young metal-rich stars of $[\mathrm{Fe/H}] = 0.6$ and $0.1 - 0.8$ Gyr (Siegel et al., 2007) or blue straggler stars (BSSs). However, we measure a wide range of metallicities for these stars, suggesting that they are BSSs instead of young stars, which would be expected to display a more homogeneous metallicity, e.g., as observed in the YMR subpopulation. Mucciarelli et al. (2017) found that the cumulative radial distributions of the BP and the intermediate-age metal-rich stars were not distinguishable. Since this is a less dense environment in comparison to the center of the NSC, these BSSs could be the product of mass transfer between binaries as has been found in other dSphs (e.g., Mapelli et al., 2007, 2009; Momany et al., 2007).

As discussed in this section, the stars from the IMR subpopulation seem to have properties consistent with those at larger radii in the galaxy. This population shows a central concentration, shallower than the other two. With the current information we are not able to tell if the stars in the inner regions are actually dynamically bound to the NSC (with the YMR and OMP) or if they are part of the main body of the host galaxy.

2.4.4 The Formation History of the Sgr dSph NSC

From this work and previous studies of the populations in the Sgr dSph NSC, we can put together the story of this NSC. It starts with two or more massive GCs that eventually merge at the center of the Sgr dSph, forming a massive nucleus consisting of old and metal-poor stars with a large metallicity spread. The two encounters of the Sgr dSph with the Galactic disk occurred ~ 2.8 and ~ 1.3 Gyr ago (Tepper-García & Bland-Hawthorn, 2018) and could have triggered two new episodes of star formation before the total stripping of the gas, creating in the first the YMR subpopulation. This results in a complex multipopulation NSC.

This NSC is on its way to becoming a stripped nucleus considering the ongoing strong interaction between its host – the Sgr dSph – and the Milky Way. In fact, Bellazzini et al. (2008) suggested that this nucleus will probably end up as a compact remnant with two populations: old metal-poor and young metal-rich, with no signatures of the progenitor galaxy. This puts the Sgr dSph NSC in close company with the most massive cluster in the Milky Way, ω Cen, which has long been considered a potential stripped nucleus (e.g., Lee et al., 1999; Carretta et al., 2010c). ω Cen presents a centrally concentrated disk-like component (van de Ven et al., 2006, see their Figures 19 and 20), very similar to the YMR subpopulation we detect in the Sgr dSph NSC. The age spread in ω Cen (at least 2 Gyr; Hilker et al., 2004; Villanova et al., 2014), similar to the spread we see in the OMP, suggests the merging of GCs early on in the nucleus of a progenitor galaxy (e.g., Bekki & Tsujimoto, 2016). Unlike ω Cen, the stripping around the Sgr dSph NSC is ongoing, and thus we have the opportunity to understand the role mergers and stripping have played in creating the cluster we see today.

Given all the evidence we have presented in this chapter, our suggestion to the community is to revert to the original naming and use “M54” in the same manner as it was given to the object upon its discovery by Charles Messier in 1778. The evidence consistently suggests that M54 is not a normal metal-poor GC but a complex NSC.

2.5 Conclusion

In this chapter we present a rich sample of ~ 6600 stellar spectra extracted from a mosaic of 16 pointings of MUSE data on M54, the NSC of the Sgr dSph, a dwarf galaxy currently being disrupted by the Milky Way. Through LOS velocity, metallicity ([Fe/H]), and age measurements we have characterized M54's stellar populations. We were able to detect at least three subpopulations with the same systemic velocity, differentiated by age and metallicity, where two of them have the same centroid.

The subpopulations we find are as follows: (i) YMR: young metal-rich, with ages 2.2 Gyr and average metallicity $[\mathrm{Fe/H}] = -0.04$; (ii) IMR: intermediate-age metal-rich, with ages of 4.3 Gyr and metallicity $[\mathrm{Fe/H}] = -0.29$; and (iii) OMP: old metal-poor, with ages 12.2 Gyr and metallicity $[\mathrm{Fe/H}] = -1.41$.

The existence of these three distinct subpopulations with the displayed differences in age and metallicity suggests the following conclusions:

- The stars in the OMP population have ages and metallicity consistent with it being assembled by two or more star clusters in-spiraling to the nucleus via dynamical friction.
- The YMR population is both more flattened and more centrally concentrated than the other two populations. These features suggest in-situ formation from enriched gas retained in the deep potential well of M54. This young, centrally concentrated component is similar to features observed in other NSCs. We estimate that the YMR subpopulation formation episode started around 3 Gyr ago, consistent with the time of the first big encounter between the Sgr dSph and the Milky Way, suggesting that gas was channeled into the nucleus during this encounter. The youngest stars in the YMR population, < 3 Gyr, might be related to when the Sgr dSph lost its gas during its ongoing interaction with the Milky Way. Alternatively, the YMR subpopulation could have formed from gas ejected from high-mass and metal-rich stars in the IMR subpopulation retained in the deep potential of the massive OMP subpopulation.
- Our metallicity measurements for the IMR subpopulation are consistent with those for the field star population of the galaxy, including regions close to the center. This subpopulation shows the lowest central concentration in M54 but is still significantly centrally peaked. Additional information is needed to determine whether these stars are actually dynamically bound to the NSC.

M54 is a unique test case. In this complex nucleus we find evidence for two processes that build up the NSC: (i) infall of two or more GCs, which merge to create a single high-mass cluster with a large metallicity spread, and (ii) in-situ star formation from enriched gas in the nucleus. In this case, the first scenario could be the key for the second to occur. This detailed formation history of the Sgr dSph NSC helps us understand the processes of NSC formation and the role of galaxy-galaxy interaction in this formation.

Chapter 3

Kinematic Characterization of the Stellar Populations in M54

From the evidence presented in Chapter 2, we suggested using "M54" to refer to the Sgr dSph NSC, as in the time of its discovery by Messier in 1778. Therefore, hereafter in this Thesis, we will refer as M54 to the NSC itself and not just the metal-poor population.

When detailed measurements of kinematics are possible, rotation seems to be a common dynamical ingredient of NSCs (Feldmeier et al., 2014; Nguyen et al., 2018), as well as of GCs (e.g., Bellazzini et al., 2012; Bianchini et al., 2013; Fabricius et al., 2014; Bellini et al., 2017a; Kamann et al., 2018; Bianchini et al., 2018; Sollima et al., 2019). In these latter systems the presence of internal rotation can be an indicator of the formation mechanism (Mastrobuono-Battisti & Perets, 2013, 2016; Hénault-Brunet et al., 2015; Gavagnin et al., 2016; Khoperskov et al., 2018; Mastrobuono-Battisti et al., 2019).

The observed kinematics give valuable information about the origin of different stellar subpopulations in NSCs. In this chapter, we present a kinematic analysis of M54 to complement the stellar characterization of the cluster and of its three subpopulations (YMR, IMR, and OMP) presented in Chapter 2. Using the exquisite observational data provided by MUSE, we are not only able to extract the kinematics of the entire NSC as one single stellar structure (as usually performed for extragalactic NSCs), but also for the different subpopulations. This provides valuable insights into the kinematics of NSCs resulting from multiple stellar structures. Since our MUSE data set covers ~ 2.5 times the half-light radius of M54, we are able to evaluate the changes at different radii beyond that point.

In this chapter, we continue with the characterization of the different populations in M54 by kinematics. In Section 3.1 we describe the kinematic extraction analysis, including LOS velocity, velocity dispersion, and rotation. In Section 3.2 we present the kinematic extraction for M54 and each of its subpopulations. Our analysis is complemented by data coming from *Gaia DR2* which we used to reconstruct the 3D structure as presented in Section 3.3. In Section 3.4 we show ad-hoc N-body simulations developed to support our interpretation of the data and of the formation history of M54. We discuss our findings in Section 3.5 and conclusions in Section 3.6.

3.1 Analysis

In this section we describe the methods we use for the kinematic extraction, which are applied to the samples presented in the next section.

3.1.1 Line-of-sight Velocity

In Section 2.2, we described the determination of physical parameters and LOS velocities of the stars using ULySS (University of Lyon Spectroscopic Analysis Software, Koleva et al., 2009). To obtain the stellar atmospheric parameters, ULySS interpolates and fits a stellar library of synthetic spectral templates characterized by a different metallicity [Fe/H], surface gravity and temperature to an observed spectrum. We use the synthetic spectroscopic grid built on the basis of the ELODIE 3.2 library (Wu et al., 2011). The median of the uncertainties of the LOS velocities estimated by UlySS is 2.2 km s^{-1}. We corrected the LOS velocity of the stars for the effect of perspective rotation using Equation 6 in van de Ven et al. (2006).

3.1.2 Rotation and Velocity Dispersion Estimate

Constraining the rotation of the subpopulations of M54 can provide fundamental constraints on their origin. We measure the rotation and dispersion properties of M54 simultaneously, using a discrete Bayesian approach similar to the procedure described in Cordero et al. (2017) and Koch et al. (2018). We approximate our velocity dispersion profile with a Plummer model (Plummer, 1911):

$$\sigma(r)^2 = \frac{\sigma_0^2}{\sqrt{1+\frac{r^2}{a^2}}}, \tag{3.1}$$

where σ_0 and a are the central velocity dispersion and the Plummer radius respectively, both set as free parameters. The mean LOS velocity ($< V_{LOS} >$) is also set as a free parameter. We use a Plummer model instead of a King model since a Plummer model provides better estimates for kinematics, while a King model seems to provide more satisfactory results for photometric profiles. We approximate the rotation profile with an analytical model (Mackey et al., 2013; Kacharov et al., 2014; Cordero et al., 2017):

$$V_{rot}\sin i = \frac{2V_{max}}{r_{peak}} \times \frac{X_{\mathrm{PA}}}{1+(X_{\mathrm{PA}}/r_{peak})^2}, \tag{3.2}$$

where $V_{rot}\sin i$ is the rotation amplitude at position X_{PA} within a factor of the clusters inclination (i) with respect to the LOS. The independent variable X_{PA} represents the distance of the different points to the center of M54 along the equatorial axis. For this model, we set three free parameters: V_{max}, the maximum rotation amplitude; r_{peak}, the projected radius where V_{max} is reached; and the rotation axis position angle (PA, measured from north 0° to east 90°). We set a weak Gaussian prior to r_{peak} centered at 0 with a standard deviation of $4\overset{\prime}{.}0$ – about 5 times the half-light radius and ~ 0.5 times the tidal radius of the cluster. We account for a total of six free parameters in our discrete kinematic model: σ_0, a, $< V_{LOS} >$, V_{max}, r_{peak}, and PA. We optimize the Gaussian likelihood function (see Eq. 2 & 5 in Cordero et al., 2017) using the MCMC algorithm (Goodman & Weare, 2010; Foreman-Mackey et al., 2013). We use this method since evaluating discrete data provides more accurate results than other methods that require binning the data, which can end in loss of information.

We measure the rotation amplitude of the rotation (A_{rot}) as the half of the difference between the maximum likelihood median velocity on the two sides of the rotation axis. For the analysis in the Section 3.2.3, we additionally measure the rotation at the half-light radius (A_{HL}) as the median of the rotation model posterior distribution at that radius, and the uncertainty is given by the standard deviation.

In the next section we present velocity maps, velocity dispersion profiles, velocity gradients and rotation profiles for the different samples defined in the Section 3.2. For all plots, the solid line shows the median of the respective best-fit models, and the dashed lines show the uncertainty. In addition to the median of the best-fit models for the discrete data, for representation, we include in the velocity dispersion and rotation profiles the velocity dispersion and rotation estimated adopting radial bins of $0\overset{\prime}{.}3$ and $0\overset{\prime}{.}6$, respectively.

3.2 Kinematic Extraction

M54 provides us with the unique opportunity to compare the integrated LOS kinematic maps of an NSC with those of its stellar subpopulations. In this section we present the results of the kinematic extraction applied to: (i) all M54's member stars as a whole – with no distinction in subpopulations – and (ii) for the three subpopulations in M54 found in Chapter 2.

The results illustrated in this section are summarized in Table 3.1. For an easier comparison, we include in this table some of the subpopulation parameters from Chapter 2 (i.e., [Fe/H], age, ellipticity, etc).

3.2.1 Kinematics of all M54 Member Stars

The member stars sample at our disposal includes 6 651 member stars of M54. These stars show a large range in age (0.5 to 14 Gyr) and metallicity ($-2.5 < [\mathrm{Fe/H}] < 0.5$). This sample represent the kinematic extraction from one single structure, as commonly performed for NSCs when it is not possible to distinguish the different populations.

3.2.1.1 Line-of-sight Velocity and Velocity Dispersion

In the top panel of Figure 3.1 we show the velocity map of our observed M54 member stars. The displayed LOS velocity varies between ∼80 to 210 km s^{-1}, represented by a median value of 141.34 ± 0.18 km s^{-1}. The median of the best-fit rotation axis, is shown as a solid gray line at $6.5 \pm 7.5°$. The dashed gray lines represent the 1σ uncertainties. The dashed circle shows the half-light radius of M54 ($\mathrm{R_{HL}} = 0'.82$, Harris, 1996, 2010 edition). The bottom panel of Figure 3.1 presents the velocity dispersion profile. The median of the best-fit Plummer profiles on the data is shown as a solid gray line, and the dashed gray lines show the $\pm 3\sigma$ uncertainty. The median central velocity dispersion is $\sigma = 16.31 \pm 0.29$ km s^{-1}. The gray circles show the velocity dispersion from the data points estimated in radial bins of $0'.3$, and the vertical dashed line shows the half-light radius of M54.

3.2.1.2 Rotation

The results of the rotation analysis for M54 are presented in Figure 3.2. In the top panel we show the velocity gradient perpendicular to the rotation axis. This choice ensures that we are observing the maximum rotation signal. The median of the best-fit rotation models is overplotted as a solid black line; the dashed black lines show ±3 times the velocity dispersion. In the bottom panel, we present the median of the best-fit rotation models to the discrete data obtained using Eq. 3.2 as a solid gray line, and the $\pm 3\sigma$ uncertainty as dashed gray lines. The vertical dashed lines show the half-light radius of M54 ($\mathrm{R_{HL}} = 0'.82$, Harris, 1996, 2010 edition). For representation, the gray circles represent the rotation profile derived as the difference between the median velocity and the systemic velocity for overlapping bins of $0'.6$ along the line perpendicular to the rotation axis. The horizontal and vertical error bars represent the radial bin size and the uncertainties in the offset of the median velocity, respectively.

We detect a low – but still considerable – amount of rotation in M54. We obtain a median rotation amplitude of $A_{rot} = 1.40 \pm 0.38$ km s^{-1}, with the rotation axis at $6.5 \pm 7.5°$, and a median maximum rotation of $V_{max} = 1.97 \pm 0.49$ km s^{-1}.

3.2.2 Kinematics of M54's Subpopulations

In this section, we study the kinematics of each of the three subpopulations identified via age and metallicity in Chapter 2:

- YMR: young metal-rich (440 stars), with mean age of 2.2 Gyr and mean metallicity of $[\mathrm{Fe/H}] = -0.04$, including the red clump stars (see Section 2.2.6 for details).

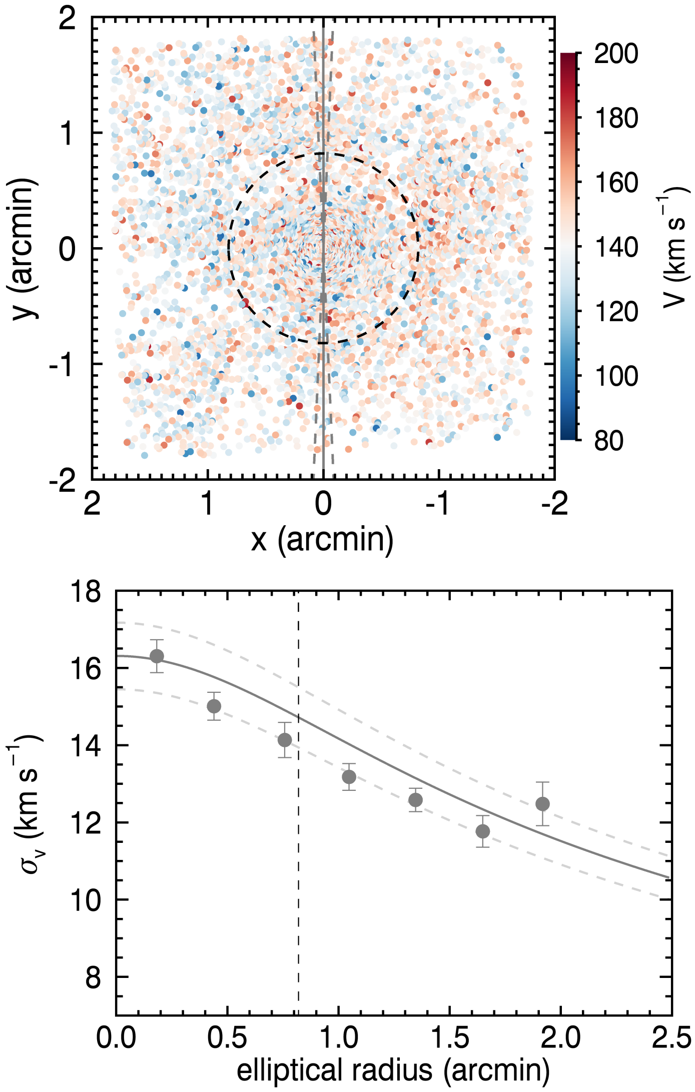

Figure 3.1 Kinematics for all the 6 651 member stars of M54. Top: Velocity map. The median of the best-fit rotation axes at $6.5 \pm 7.5^\circ$ is shown as a solid gray line, and the 1σ uncertainty as dashed gray lines. The dashed circle shows the half-light radius of M54 ($R_{HL} = 0\overset{\prime}{.}82$, Harris, 1996, 2010 edition). Bottom: Velocity dispersion profile. The median of the best-fit Plummer profiles is shown as a solid gray line, and the $\pm 3\sigma$ uncertainty as dashed gray lines. The gray circles show the velocity dispersion estimated in radial bins of $0\overset{\prime}{.}3$. The vertical dashed line shows the half-light radius of M54.

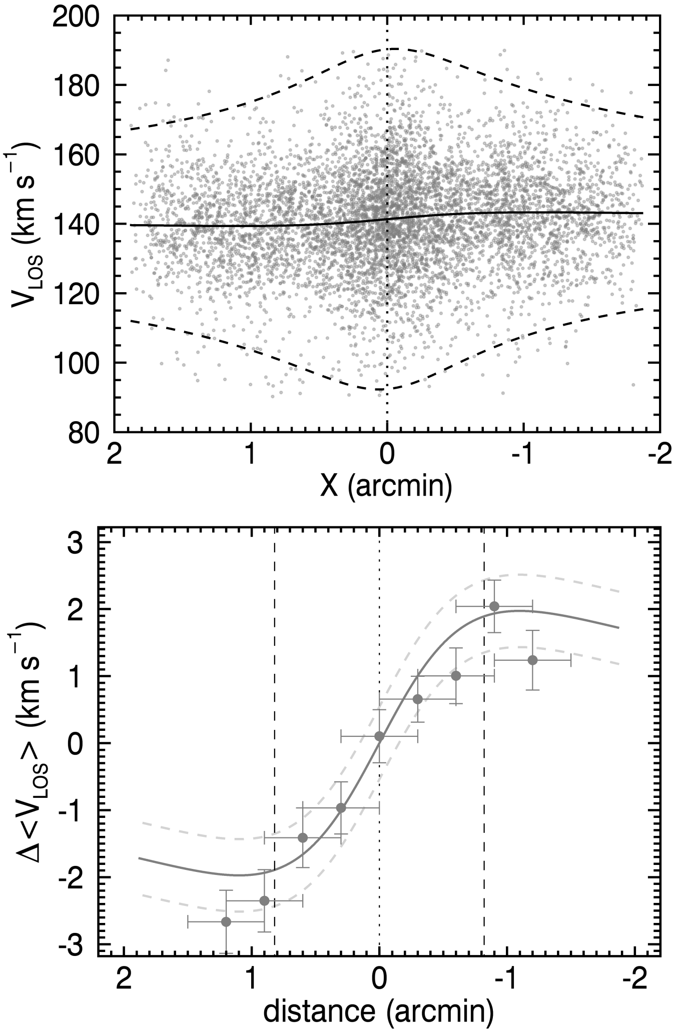

Figure 3.2 Rotation estimate for all 6 651 M54 member stars. Top: Velocity gradient of M54 with respect to a perpendicular line to the rotation axis. The solid black line shows the median of the best-fit rotation models and the dashed black lines show ±3 times the velocity dispersion. Bottom: Rotation profile. The gray solid line shows the median of the best-fit rotation models, and the dashed gray lines show the 3σ uncertainty. The black circles show the rotation profile obtained for overlapping bins of 0′.6 along the line perpendicular to the rotation axis. The horizontal and vertical error bars represent the bin size and the uncertainties in the offset of the median velocity, respectively. The vertical dashed lines show the half-light radius of M54 (R_{HL}= 0′.82, Harris, 1996, 2010 edition).

- IMR: intermediate-age metal-rich (536 stars), with mean age of 4.3 Gyr and mean metallicity of $[\mathrm{Fe/H}] = -0.29$.
- OMP: old metal-poor (2 550 stars), with mean age of 12.2 Gyr and mean metallicity of $[\mathrm{Fe/H}] = -1.41$.

The number of stars in the M54 sample is larger than the sum of the three subpopulations because it includes the horizontal branch stars (which were excluded for the age estimates), outliers from the Multi-Gaussian model performed in Chapter 2, and stars with ages with relative errors $> 40\%$.

In subsequent figures, we will show the YMR population in red, the IMR population in orange, and the OMP population in blue.

3.2.2.1 Line-of-sight velocity and velocity dispersion

The left panels of Figure 3.3 show the velocity maps for each of the subpopulations in M54, separated by their age and metallicity: YMR, IMR, and OMP, from top to bottom, respectively. The half-light radius of M54 is shown as a dashed circle ($R_{\mathrm{HL}} = 0\overset{\prime}{.}82$, Harris, 1996, 2010 edition). The median of the best-fit rotation axes is represented by a solid gray line, and the dashed lines show the $\pm 1\sigma$ uncertainty. We found very similar median LOS velocities and median rotation axis position angles for the three populations. The median velocities are 141.92 ± 0.54 km s^{-1} for the YMR, 142.61 ± 0.59 km s^{-1} for the IMR, and 141.22 ± 0.26 km s^{-1} for the OMP. The median rotation axis is: $-0.8 \pm 7.6°$ for the YMR, $-4.0 \pm 26.4°$ for the IMR, and $2.9 \pm 23.5°$ for the OMP. From the velocity maps we observe a clear velocity gradient for the YMR subpopulation only.

The velocity dispersion profile for each of the M54's subpopulations is presented in the right panels of Figure 3.3. In each case, the solid gray line represents the median of the best-fit Plummer models to the discrete data, and the dashed gray lines show the $\pm 3\sigma$ uncertainty. The vertical dashed line shows the half-light radius of M54 ($R_{\mathrm{HL}} = 0\overset{\prime}{.}82$, Harris, 1996, 2010 edition). The respective color circles show the velocity dispersion from the data estimated in radial bins of $0\overset{\prime}{.}3$. The top left panel shows the profile for the YMR subpopulation. We estimate a median central velocity dispersion of $\sigma_0 = 13.15 \pm 0.56$ km s^{-1}. The middle right panel shows the case for the IMR subpopulation with a median central value of $\sigma_0 = 15.24 \pm 0.89$ km s^{-1}. For the YMR and IMR velocity dispersion profiles we observe that they rather follow a flat distribution along the observed radius, thus the best-fit Plummer profiles do not provide a good description of the data for these two subpopulations. On the contrary, as seen in the bottom right panel, the OMP velocity dispersion profile is very well fit by a Plummer model. The median central velocity dispersion for the OMP subpopulation is $\sigma_0 = 15.22 \pm 0.52$ km s^{-1}.

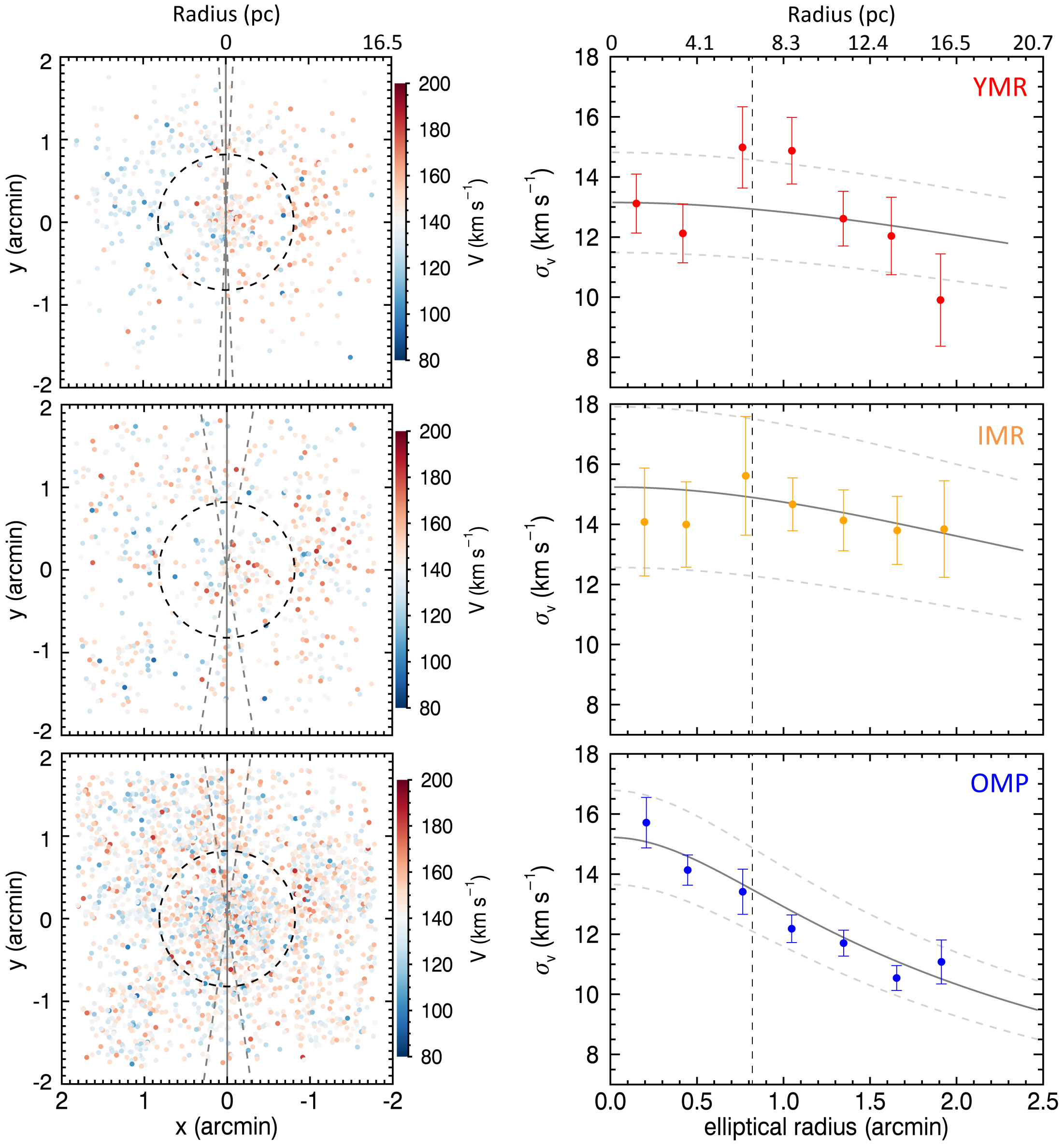

Figure 3.3 Kinematic extraction for the three subpopulations of M54: YMR in top panels, IMR in middle panels and OMP in bottom panels. Left panels: velocity maps. The gray solid lines show the median of the best-fit rotation axes, and the dashed gray lines the 1σ uncertainty. Dashed circles show the half-light radius of M54 (R$_{\rm HL}$= 0′.82, Harris, 1996). Right panels: Velocity dispersion profiles. The median of the best-fit Plummer profiles is shown as a solid gray line, and the dashed gray lines show the ±3σ uncertainty. The respective color circles show the velocity dispersion obtained adopting radial bins of 0′.3. The vertical dashed lines show the half-light radius of M54.

3.2.2.2 Rotation

As shown in Figure 3.4, the three subpopulations detected in M54 display different amounts of rotation. The left panels illustrate the velocity gradient of each subpopulation along the line perpendicular to the rotation axis. Overplotted as a solid black line is the best-fit rotation model, while the dashed black lines show ± 3 times the velocity dispersion.

We also include the rotation profiles for these subpopulations in the right panels. The gray lines show the median of the best-fit rotation models obtained using Eq. 2, and the dashed gray lines the $\pm 3\sigma$ uncertainty. The respective color circles profiles show the difference between the median velocity and the systemic velocity along the line perpendicular to the rotation axis in overlapping bins of $0\farcm6$. The horizontal and vertical error bars represent the radial bin size of $0\farcm6$ and the uncertainties in the offset of the median velocity, respectively. The vertical dashed lines show the half-light radius of M54 ($R_{HL} = 0\farcm82$, Harris, 1996, 2010 edition). The highest median rotation amplitude is found for the YMR subpopulation with $A_{rot} = 5.01 \pm 1.04\,\mathrm{km\ s^{-1}}$ (top panels). The second highest amount of rotation is displayed by the IMR subpopulation (middle panels) with a median of $A_{rot} = 2.44 \pm 1.21\,\mathrm{km\ s^{-1}}$, less than half of that the YMR subpopulation. The OMP subpopulation shows a low amount of rotation (bottom panels), a median value of $A_{rot} = 0.72 \pm 0.54\,\mathrm{km\ s^{-1}}$. The differences in the velocity dispersion and rotation properties suggest different origins for these subpopulations (see Section 3.5).

3.2.3 V/σ_0 vs. ε

The ratio between the rotation and central velocity dispersion versus ellipticity (V/σ_0,ε) diagrams have been introduced and are widely used to evaluate how the rotation affects the shape of galaxies (e.g., Binney, 2005; Cappellari et al., 2007; Emsellem et al., 2011). However, in the last few years these diagrams have also been applied to GCs (e.g Bellazzini et al., 2012; Bianchini et al., 2013; Kacharov et al., 2014; Fabricius et al., 2014; Lardo et al., 2015; Kimmig et al., 2015; Kamann et al., 2018; Bianchini et al., 2018). For GCs, several difficulties arise because: (i) the rotation measured in clusters depends on the inclination angle of the rotation axis, which is measurable only when 3D kinematics are available (LOS velocities and proper motions, e.g., Bianchini et al. 2018; Sollima et al. 2019); (ii) ellipticity and rotation change as a function of radius (e.g., Geyer et al., 1983); (iii) anisotropy varies with radii (e.g., van de Ven et al., 2006; Jindal et al., 2019). In spite of these issues, (V/σ_0,ε) diagrams still provide important insights into the role of rotation on the shape of these stellar systems, e.g., how flattened they are (Fabricius et al., 2014; Kamann et al., 2018).

In Figure 3.5 we present a (V/σ_0,ε) diagram where we add the measurements for the whole M54 sample (gray), the YMR (red), and OMP (blue) subpopulations. We do not include the IMR subpopulation in this section since the method used to obtain the 2D morphology parameters did not converge to an ellipticity value (see Section 2.3.3). Since different definitions of V/σ_0 are used in the literature, we decide to compute the V/σ_0 in two different ways: (i) based on the

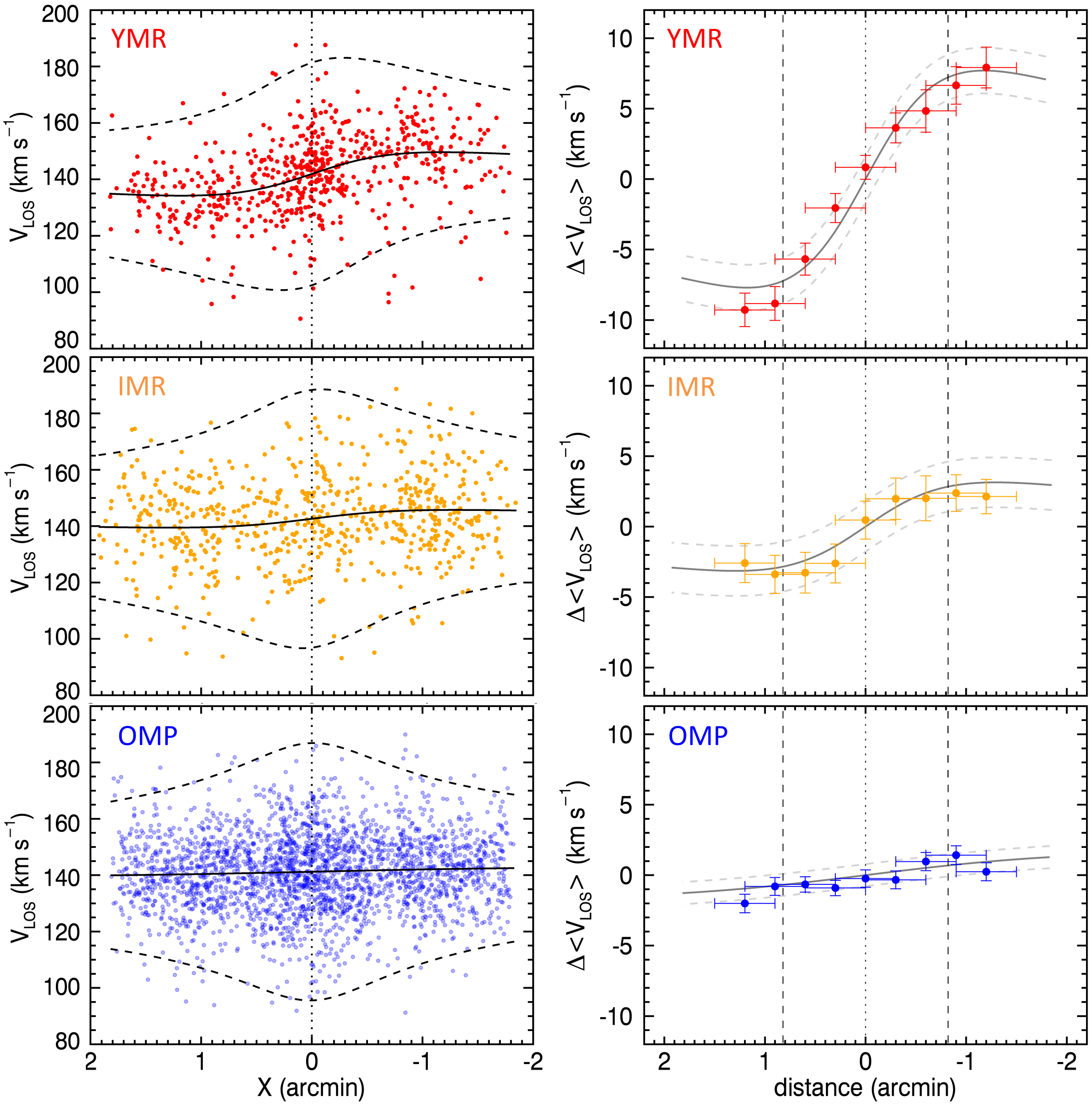

Figure 3.4 Left panels: Velocity gradients with respect to a line perpendicular to the rotation axis. The solid black line shows the best-fit rotation model, and the dashed black lines correspond to ±3 times the velocity dispersion of the respective population. Right panels: Rotation profiles. The solid gray line represents the median of the best-fit rotation models, and the dashed gray lines represent the $\pm3\sigma$ uncertainty. Respective color circles show the difference between the median velocity and the systemic velocity along the line perpendicular to the rotation axis in overlapping bins of $0'.6$. The horizontal and vertical error bars represent the radial bin size and the uncertainties in the offset of the median velocity, respectively. The vertical dashed lines show the half-light radius of M54 ($R_{HL} = 0'.82$, Harris, 1996, 2010 edition).

rotation and ellipticity at the half-light radius ($V_{\mathrm{HL}}/\sigma_0, \varepsilon_{\mathrm{HL}}$) represented by filled circles, and (ii) based on the rotation amplitude and ellipticity over the entire FOV ($A_{rot}/\sigma_0, \varepsilon$) represented by filled squares. Both ellipticity values are derived as described in Section 2.3.3 (see Table 3.1). We explore the possibility that the inclination angle, unknown a priori, could be different from an edge-on view and thus introduce a correction for inclination as described in Cappellari et al. (2007). We will show in Section 3.3 that by combining LOS data and *Gaia DR2* proper motions we can estimate that the most likely inclination angle is $\sim 90^\circ$. However, inclination angles within 60° and 90° cannot be excluded within the 1σ uncertainties. Therefore we illustrate the effects of a 60° inclination angle, and consider the corrected value as a conservative (upper limit) estimate for the intrinsic ($V/\sigma_0, \varepsilon$).

For comparison, we include literature information for the metal-poor population from Bellazzini et al. (2012, cyan triangle), who considered $\sigma_0 = 16.4$ km s^{-1} from Ibata et al. (2009) with $2 \times A_{rot} = 2$ km s^{-1} in a radius of $r \sim 5.'0$ (Bellazzini et al., 2008), and $\varepsilon = 0.06$ ($\varepsilon_{\mathrm{H96}}$; Harris, 1996, 2010 edition). We include this in the diagram as ($2 \times A_{rot}/\sigma_0, \varepsilon_{\mathrm{H96}}$). To compare with our measurements, we include a third estimate for the OMP subpopulation (blue triangle) considering $2 \times A_{rot}$ (as Bellazzini et al.) of this population versus the ellipticity in the Harris (1996, 2010 edition) catalog ($2 \times A_{rot}/\sigma_0, \varepsilon_{\mathrm{H96}}$). In addition, we add for comparison measurements for GCs from Bellazzini et al. (2012); Bianchini et al. (2013); Kacharov et al. (2014); Kamann et al. (2018). We overplot as a solid black line the relation for an isotropic oblate rotator as in Binney (2005), and the dashed black lines show the relation for an isotropic oblate rotator and with anisotropy parameter $\delta = 0.05, 0.1, 0.15, 0.2$ from left to right, as Cappellari et al. (2007).

We obtain large uncertainties for the ellipticity estimates for all cases, especially for the YMR subpopulation which consists of the lowest number of stars in the sample. Hence, we need to be cautious about the following information we extract from this diagram since more information is needed to be certain.

We observe that the ellipticity at the half-light radius $\mathrm{R_{HL}}$ is lower than considering the entire FOV for all cases (M54, YMR, and OMP). In spite of the large uncertainties in the ellipticity values, this tendency suggests that the ellipticity varies as a function of the radius with the cluster becoming more flattened at larger radii. Hence, the results for the YMR subpopulation would be consistent with the findings by Fabricius et al. (2014) and Kamann et al. (2018). They observe that the central rotation affects the shape of the cluster, finding clusters with higher rotation to be more flattened than those that do not rotate.

For the OMP subpopulation we observe a low amount of rotation, with only minor differences when estimating this value at the half-light radius $\mathrm{R_{HL}}$ (blue circle) or over the entire FOV of the sample (blue square). At the $\mathrm{R_{HL}}$ this population seems to be close to isotropic and becomes more anisotropic when going to larger radii. In spite of a small amount of rotation, the ellipticity estimated over the entire FOV shows that this subpopulation is flattened, similar to fast rotator GCs, e.g., see in Figure 3.5: ω Cen (black diamond) and M22 (black pentagon). We will discuss a possible explanation for this in Section 3.5.3.

Table 3.1. Summary of the observed properties of M54 and its stellar subpopulations.

subpopulations	M54 members	YMR	IMR	OMP
[Fe/H]	-2.5 - 0.5	-0.04 ± 0.01^a	-0.29 ± 0.01^a	-1.41 ± 0.01^a
$\sigma_{[\mathrm{Fe/H}]}$	-	0.12 ± 0.01^a	0.16 ± 0.01^a	0.24 ± 0.01^a
Age (Gyr) ^{a}	0.5 - 14	2.16 ± 0.03^a	4.28 ± 0.09^a	12.16 ± 0.05^a
σ_{Age} (Gyr)	-	0.20 ± 0.03^a	1.16 ± 0.07^a	0.92 ± 0.04^a
ε	0.13 ± 0.03	0.31 ± 0.10^a	^{b}	0.16 ± 0.06^a
$\varepsilon_{\mathrm{HL}}$	0.04 ± 0.03	0.25 ± 0.15	^{b}	0.09 ± 0.06
Position Angle (rad)	9.14 ± 6.48	4.23 ± 11.14^a	^{b}	16.43 ± 13.75^a
Median V_{LOS} (km s^{-1})	141.34 ± 0.18	141.92 ± 0.54^a	142.61 ± 0.59^a	141.22 ± 0.26^a
σ_0 (km s^{-1})	16.31 ± 0.29	13.15 ± 0.56	15.24 ± 0.89	15.22 ± 0.52
A_{rot} (km s^{-1})	1.40 ± 0.38	5.01 ± 1.04	2.44 ± 1.21	0.72 ± 0.54
A_{HL} (km s^{-1})	1.81 ± 0.31	6.98 ± 0.84	2.00 ± 0.93	0.77 ± 0.41
V_{max} (km s^{-1})	1.97 ± 0.49	7.70 ± 1.31	3.14 ± 1.97	1.57 ± 1.13
Rotation axis (degrees)	6.5 ± 7.5	-0.8 ± 7.6	-4.0 ± 26.4	2.9 ± 23.5
Number of stars	6651	440	536	2550

Note. — ^{a}: Values from Chapter 2. ^{b}: Measurements which did not converge to a value (see Section 2.3.3). $\sigma_{[\mathrm{Fe/H}]}$ and σ_{Age} correspond to the [Fe/H] and age intrinsic spreads, respectively. ε: ellipticity estimated at the entire FOV. $\varepsilon_{\mathrm{HL}}$: ellipticity estimated at the half-light radius. V_{LOS}: line-of-sight velocity. σ_0: central velocity dispersion. A_{rot}: rotation amplitude. A_{HL}: rotation at the half-light radius. V_{max}: maximum rotation. *Note*: The number of stars in the M54 sample is larger than the sum of the three subpopulations because it includes: horizontal branch stars (which were excluded for the age estimates), outliers from the Multi-Gaussian model performed in Chapter 2 for constraining the subpopulations, and stars with ages with relative errors $> 40\%$.

Our rotation estimates for M54 and its OMP subpopulation are consistent with the estimate for the metal-poor population by Bellazzini et al. (2012, cyan triangle in Figure 3.5), who considered an ellipticity of $\varepsilon = 0.06$ from Harris (1996, 2010 edition). A more consistent agreement between the rotation and ellipticity of the OMP population reported by Bellazzini et al. (2012) was expected because their sample does not include young and metal-rich stars.

3.3 M54 Kinematics with *Gaia DR2*

The recent availability of precision astrometry led by *Gaia DR2* (Gaia Collaboration et al., 2016, 2018) opened the possibility of studying the kinematics of GCs in 3D (e.g., Sollima et al., 2019). Here we exploit for the first time the available *Gaia* proper motions with the goal of characterizing the intrinsic dynamical properties of M54's subpopulations.

We cross-match our MUSE M54 stellar sample with the *Gaia DR2* catalog (Gaia Collaboration et al., 2016, 2018) finding a total of 638 OMP stars, 109 YMR stars, and 32 IMR stars, for

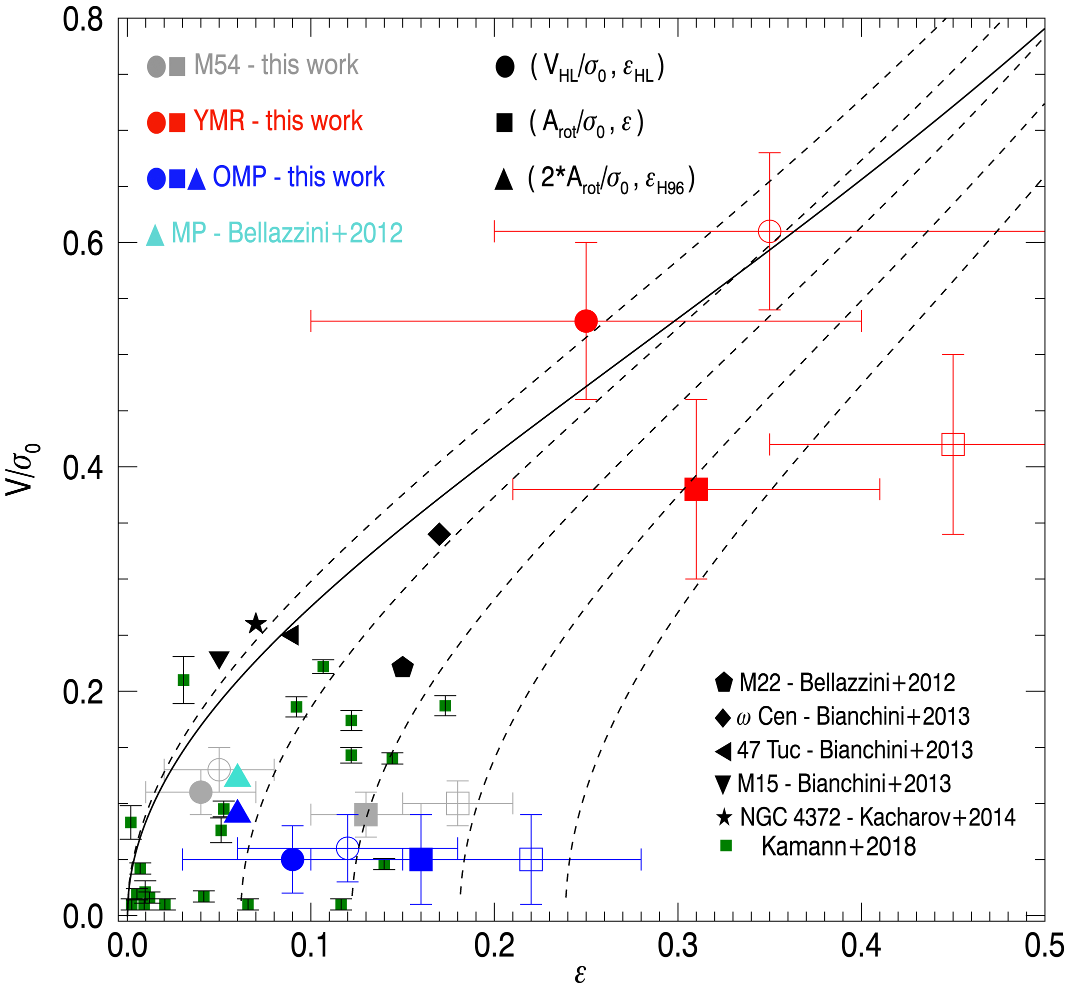

Figure 3.5 $(V/\sigma_0, \varepsilon)$ diagram. We present our estimates for the entire sample of stars (M54), the YMR and OMP subpopulations in gray, red, and blue, respectively. The filled circles show the estimates based on the rotation and ellipticity at the half-light radius $(V_{\rm HL}/\sigma_0, \varepsilon_{\rm HL})$, the filled squares, on the rotation amplitude and ellipticity over the entire FOV $(A_{rot}/\sigma_0, \varepsilon)$, and the filled triangle two times the rotation amplitude and ellipticity from the Harris (1996, 2010 edition) catalog $(2 \times A_{rot}/\sigma_0, \varepsilon_{\rm H96})$. The empty symbols show the corrected value for an inclination of 60° using the equation by Cappellari et al. (2007). We include the value from Bellazzini et al. (2008, 2012) for the metal-poor population as a turquoise triangle, whose value was estimated using $2 \times A_{rot}$ and the ellipticity from the Harris (1996, 2010 edition) catalog. For comparison, we include values for GCs from the literature (e.g., Bellazzini et al., 2012; Bianchini et al., 2013; Kacharov et al., 2014) and in green squares the GC sample from Kamann et al. (2018). The solid black line gives the relation for an isotropic oblate rotator presented in Binney (2005). The dashed black lines show the relation for an isotropic oblate rotator and with anisotropy parameters of $\delta = 0.05, 0.1, 0.15, 0.2$, from left to right (Cappellari et al., 2007)

.

which the full 3D velocity vector is measured. These stars have magnitudes $G < 20$, and are within $\sim 2\farcm0$ from M54's center. However, M54 represents a challenging environment for *Gaia* astrometry due to the high crowding of the FOV and the large distance of the cluster. To obtain reliable measurements, we need to further restrict the sample to only stars with high-quality proper motion measurements. For this purpose, we perform quality cuts, following some of the procedures illustrated in Lindegren et al. (2018) and Vasiliev (2019), to eliminate stars with bad astrometric measurements and strongly affected by crowding. These cuts, based on parameters provided in the *Gaia DR2* catalog, include:

- `astrometric_gof_al` < 0.5
- `astrometric_excess_noise` < 1
- unit weight error, $uw =< 1.2$ (see Lindegren et al., 2018 for definition)
- `phot_bp_rp_excess_factor` $< 2.0 + 0.06\,(\texttt{bp-rp})^2$, with `bp-rp` the color in *Gaia* filters.
- proper motions errors < 0.5 mas yr^{-1} (corresponding to ~ 60 km s^{-1} at M54 distance).

Our final sample consists of a total of 108 OMP stars and 15 for the YMR subpopulation, with an average uncertainty in proper motion measurements of 0.19 mas yr^{-1} (corresponding to $\sim$25 km s^{-1}). The final sample for the IMR subpopulations consist in 2 stars only. Since this is not sufficient to perform the analysis, we will just consider the YMR and OMP subpopulation.

3.3.1 Rotation with *Gaia DR2*

We transform the positions and velocities from celestial to Cartesian coordinates using Eq. 2 from Gaia Collaboration et al. (2018) and Eq. 1 of van de Ven et al. (2006) (see also Bianchini et al. 2018). We correct the LOS velocities and proper motions by perspective rotation following Eq. 6 in van de Ven et al. (2006). Finally, when converting proper motions from mas yr^{-1} to km s^{-1}, we assume a distance of 28.4 kpc (Siegel et al., 2011). As a further test, we also assume a distance of 26.5 kpc (Harris, 1996, 2010 edition) obtaining consistent results.

We measure the mean motions of the two proper motion components using the likelihood employed in Bianchini et al. (2018, Eq. 2 and 3). For the OMP stars we obtain mean motions of $(\mu_x, \mu_y) = (2.80 \pm 0.03, 1.40 \pm 0.02)$ mas yr^{-1}, and $(\mu_x, \mu_y) = (2.77 \pm 0.09, 1.48 \pm 0.08)$ mas yr^{-1} for the YMR stars. These values are consistent with each other and with the value reported by Vasiliev (2019), who made no distinction between subpopulations in M54. Together with the fact that the mean LOS velocities of the OMP and YMR components are also consistent with each other, this further indicates that the two stellar populations are comoving and therefore they belong to the same bound stellar system.

To search for a signature of rotation we consider polar coordinates on the plane of the sky and analyze the tangential component of proper motions (μ_t). Both populations show a mean

Table 3.2. 3D modeling of the intrinsic rotation using the three velocity components.

subpopulations	θ_0 (deg)	A_{rot} (km s^{-1})	i (deg)
YMR	$29.8^{+18.9}_{-20.1}$	$13.5^{+6.4}_{-5.8}$	$80.8^{+6.9}_{-14.3}$
OMP	$-40.1^{+78.5}_{-134.1}$	$2.0^{+1.4}_{-1.8}$	$29.8^{+19.5}_{-33.2}$

value of μ_t consistent with zero ($\mu_{t,OMP} = 0.012 \pm 0.030$ mas yr^{-1} and $\mu_{t,YMR} = -0.058 \pm 0.113$ mas yr^{-1}), indicating no signal of rotation, within the 1σ error. However, we note that the sample size of the YMR population is composed of only 15 stars and, moreover, the putative rotation signal that we are trying to measure (< 10 km s^{-1}) is below the nominal systematic uncertainties for *Gaia DR2* data (0.07 mas yr^{-1}, Lindegren et al., 2018). Therefore a presence of rotation on the plane of the sky cannot be excluded with this analysis and the current data.

3.3.2 Rotation from 3D Kinematics

Since our sample consists of the full three-dimensional velocity vectors, we can estimate the intrinsic rotation exploiting simultaneously the three velocity components, following the likelihood method described by Sollima et al. (2019, likelihood in Eq. 3). We assume a constant rotation amplitude[1] within the cluster and take into consideration the discrete velocity measurements, their uncertainties and their covariance matrix. We sample the likelihood and derive the $1-\sigma$ errors using `emcee` by Foreman-Mackey et al. (2013) keeping as free parameters the position angle of the rotation axis on the plane of the sky (θ_0, measured from west of north), the inclination angle of the rotation axis with respect to the LOS (i, with $i = \pi/2$, corresponding to an edge-on view), and the amplitude of the intrinsic rotation (A_{rot}, measured in km s^{-1}). We fix a velocity dispersion of 13 km s^{-1} (as derived globally from LOS velocities only) for the modeling.

The results obtained for the OMP and YMR components are shown in Figure 3.6 and reported in Table 3.2. We do not detect intrinsic rotation in the OMP component ($2.0^{+1.4}_{-1.8}$ km s^{-1}). On the other hand, the YMR population shows a strong signature of rotation ($13.5^{+6.4}_{-5.8}$ km s^{-1}), predominantly along the LOS, since the recovered inclination angle i is consistent with an edge-on view. In Figure 3.7, we show the result of the simultaneous modeling of the three velocity components for the YMR component.

---

[1] This assumption is motivated by fact that when doing the 3D analysis, we only have a few tens of stars. Then, the discrepancies that we see for the YMR subpopulation is likely due to this small data set.

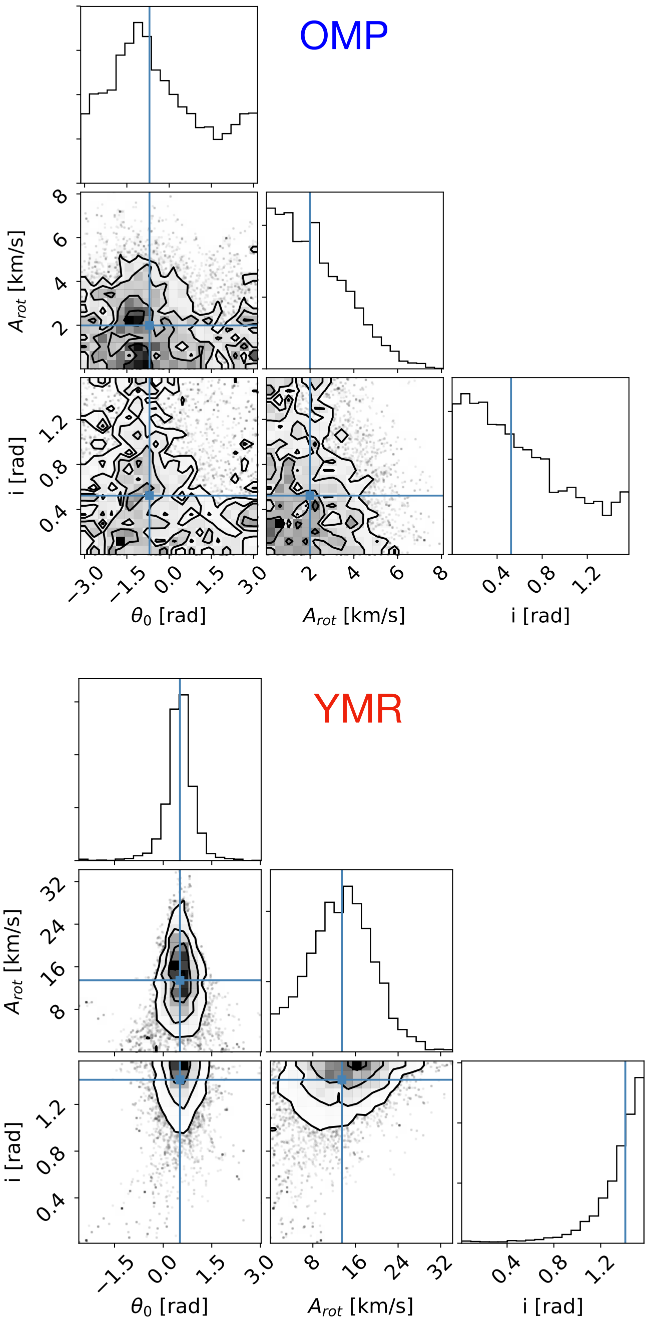

Figure 3.6 Results of the MCMC sampling of intrinsic 3D rotation of the OMP component (top panel; 108 data points) and of the YMR component (bottom panel; 15 data points). The sampled parameters are the position angle of the rotation axis in the plane of the sky (θ_0), the amplitude of the rotation (A_{rot}), and the inclination angle of the rotation axis with respect to the LOS (i). No rotation is observed for the OMP stars, while clear rotation, mostly in the LOS velocity component, is measured for the YMR stars. The blue lines show the mean of the respective axis parameter.

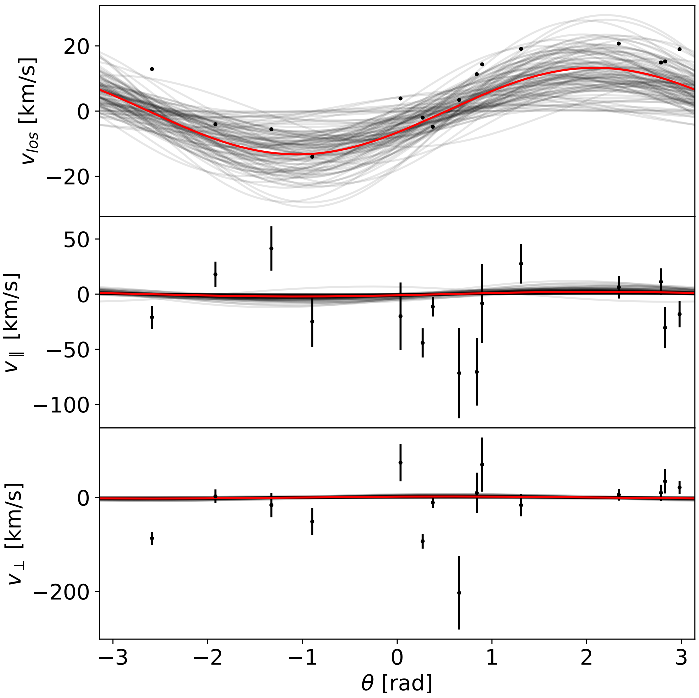

Figure 3.7 Result of the fit for the YMR stars shown for the three components of the velocity vector, namely the LOS component, the proper motion component parallel to the rotation axis, and the proper motion component perpendicular to the rotation axis. The red line indicates the result of the MCMC and the grey lines are 100 samples from the chain.

3.4 Comparison with N-body Simulations

To understand the origin of the morphological and kinematical structure of the system, we simulated a two-component M54-like cluster with a total mass equal to $1.4 \times 10^6 M_\odot$. The modeled cluster is characterized by a YMR/OMP mass ratio of 0.20 (based on the number ratio of stars), as suggested by the observations. The OMP population is represented by a non-rotating, spherical King (1966) profile with a total mass of $1.17 \times 10^6 M_\odot$, $W_0 = 8.6$, and a core radius of 0.71 pc (Harris, 1996). The remaining mass of the cluster is included as a flattened and centrally-concentrated YMR population (50% of the mass is enclosed within 3 pc from the center of the cluster), to represent the young stellar component formed in situ from gas that flowed into the center of the cluster conserving its angular momentum. This disk-like component has an ellipticity ranging from $\varepsilon \approx 0.1$ in the central region and to $\varepsilon = 0.6 - 0.7$ at radii larger than 6 pc. The YMR population initially rotates with a peak velocity of 15 km s^{-1}, a value similar to the maximum rotational velocity of the YMR population observed in M54.

The N-body system was modeled using a total number of $N = 50000$ ($N_{OMP} = 41786$ and $N_{YMR} = 8214$) of single mass particles. The mass of each particle is $m_* \approx 28 M_\odot$ and we adopted a softening length of 0.01 pc to smooth the close encounters between particles. Taking into account both of these approximations, the simulation time was rescaled to the evolutionary time of the system formed by the actual number of stars, assuming an average stellar mass of $0.5 M_\odot$, by using the ratio between the relaxation times of the real and simulated system as described in Mastrobuono-Battisti & Perets (2013). The initial conditions were built using the NEMO toolkit (Teuben, 1995). We evolved the system for 2 Gyr – the age of the YMR population – using a version of the direct N-body code phiGRAPE adapted to run on GPUs (Harfst et al., 2007; Gaburov et al., 2009). The coevolution of the two populations and, in particular, the relaxation of the initially flattened YMR component, contributes to modify the final shape and kinematics of the whole cluster.

To evaluate the ellipticity of the different populations at the end of the simulation, we calculated their axial ratios using the inertia moments, as detailed in Katz (1991). The b/a ratio between the intermediate and major axis is approximately equal to 1.0 at all radii, and the ellipticity is defined as $\varepsilon = 1 - c/a$, where c is the minor axis of the system. The final ellipticity of the YMR population varies significantly with the distance from the center of the cluster; the YMR stars are still in a significantly flattened configuration with ellipticity close to the initial one. In particular, the young component is almost spherical in the central regions of the cluster, while the ellipticity increases up to $\varepsilon = 0.65$ at radii larger than 5 pc. The ellipticity is ≈ 0.5 at 5.5 pc, which is the half-mass radius of the cluster. The slight decrease in the ellipticity of the young population corresponds to an increase of flattening in the old stellar component. After 2 Gyr of coevolution with the younger component, the initially-spherical OMP population becomes more flattened, reaching a maximum ellipticity of around 0.1. The ellipticity of this population decreases steadily with the distance from the cluster center (see top panel of Figure 3.8).

The change in morphology corresponds to a slight increase in the velocity anisotropy, whose amount is parametrized by the quantity $\beta_z = 1 - (\sigma_z/\sigma_R)^2$ in cylindrical coordinates with the z axis parallel to the angular momentum vector of the system (see bottom panel of Figure 3.8). While, after 2 Gyr, the YMR disc still rotates with a peak velocity of around 12.5 km s^{-1}, the OMP population only shows a weak rotation pattern, with a peak velocity of $\sim$ 1 km s^{-1} (see Figure 3.9). As already found by Mastrobuono-Battisti & Perets (2013, 2016), this result suggests that the coevolution of an initially spherical system with an embedded disc leads to an angular momentum redistribution between the flattened YMR and the OMP population. From this process follows the mixing of the YMR and the OMP populations and the increased flattening of the OMP population (see top panel of Figure 3.10 for the angular momentum evolution of the two populations). The growing flattening is accompanied by only a slight increase in the rotation speed of the OMP population. The two populations, after 2 Gyr of evolution, are not yet fully mixed, with the YMR population still more centrally concentrated and less extended than the OMP population (see bottom panel of Figure 3.10).

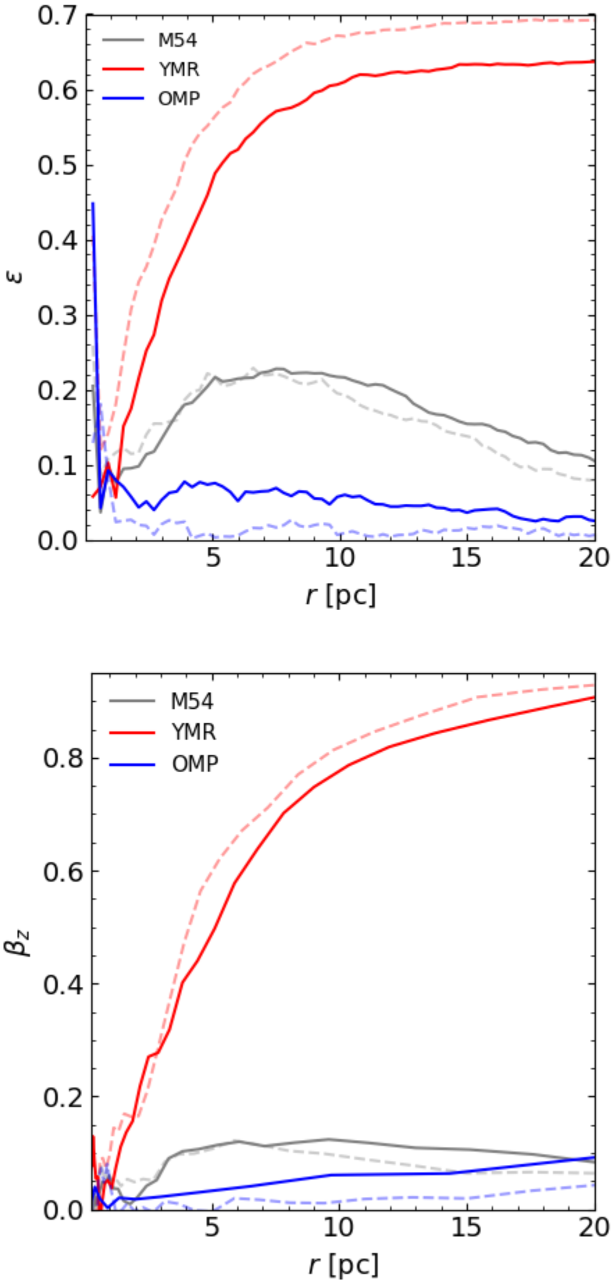

Figure 3.8 Ellipticity (top panel) and anisotropy parameter β_z (bottom panel) as a function of radius for the whole system M54 (gray), the OMP (blue), and YMR (red) populations at 0 Gyr (dashed lines) and after 2 Gyr of evolution (solid lines) as obtained from the N-body simulation. The angular momentum lost by the YMR population is acquired by the OMP population, that becomes slightly flattened and acquires a small amount of velocity anisotropy along the z axis. Plots are obtained considering the edge-on view of the cluster.

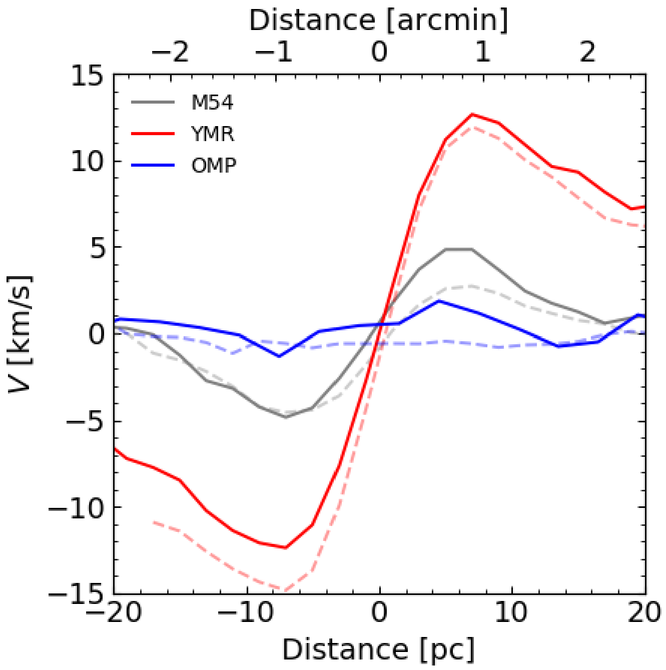

Figure 3.9 Rotation curves for the whole system M54 (gray), the OMP (blue), and YMR (red) populations at 0 Gyr (dashed lines) and after 2 Gyr of evolution (solid lines) as obtained from the N-body simulation. While the YMR population still rotates significantly, the OMP population has acquired a small ($\sim$ 1 km s^{-1}) rotational speed. The cluster is seen edge-on.

3.5 Discussion

3.5.1 Kinematic Comparison

As mentioned in Chapter 2 and shown in detail in the previous sections, the LOS velocity measurements we observe for a large sample of stars show that all subpopulations are in spatial coincidence, as also suggested by Da Costa & Armandroff (1995); Ibata et al. (1997); Monaco et al. (2005a); Bellazzini et al. (2008). We observe that the three subpopulations display different velocity dispersion profiles. The profiles are close to flat for the YMR and IMR subpopulations. For the OMP subpopulation, the observed velocity dispersion is well described by a Plummer profile, with a median central velocity dispersion of $\sigma_0 = 15.22 \pm 0.52$ km s^{-1} and $\sigma \sim 10$ km s^{-1} at $r = 1\overset{'}{.}6$. This is in good agreement with the velocity dispersion estimates by previous studies (e.g., Bellazzini et al., 2008; Baumgardt & Hilker, 2018).

From our MUSE data set we find that the YMR subpopulation rotates ($A_{rot} = 5.01 \pm 1.04$ km s^{-1} and $V_{max} = 7.70 \pm 1.31$ km s^{-1}) at a considerably higher speed than the OMP, which shows a weak sign of rotation ($A_{rot} = 0.72 \pm 0.54$ km s^{-1} and $V_{max} = 1.57 \pm 1.13$ km s^{-1}). Consistently, through 3D rotation modeling based on selected high-quality *Gaia DR2* data combined with our MUSE data set, we detect rotation for the YMR component and no rotation for the OMP.

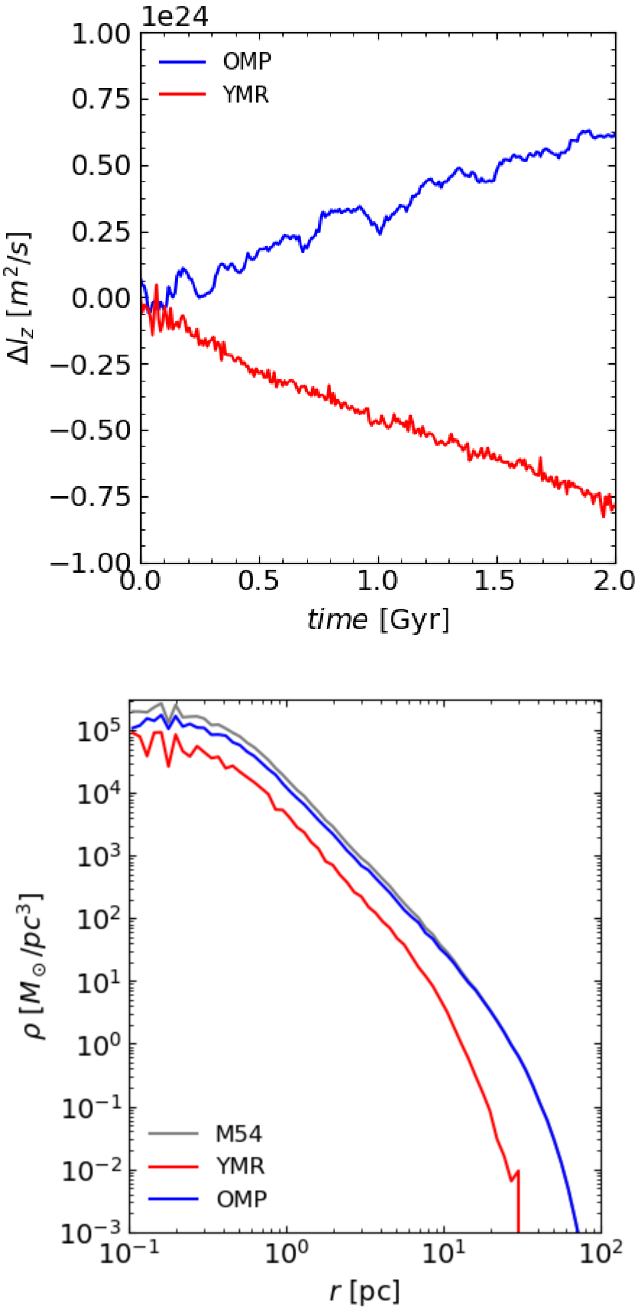

Figure 3.10 Top: Evolution of the average angular momentum per unit mass perpendicular to the maximum rotation plane for the YMR (red) and OMP (blue) populations. The angular momentum lost by the YMR stars is redistributed among the OMP stars that, consequently, acquire a coherent rotational pattern and settle on a slightly flattened configuration. Bottom: Spatial density profiles of the system, from the N-body simulations, considered as a whole (gray), and of the YMR (red) and OMP (blue) components taken separately as obtained from the N-body simulation.

Although we find consistency between our measurements, the interpretation of the 3D rotation modeling should be phrased with caution. *Gaia* proper motions are affected by systematic errors, which have the same order of magnitude of the rotation signal we are trying to measure (0.07 mas/yr, $8-9$ kpc at M54 distance). Due to large distances, crowding, and high densities in the center of compact stellar systems, the *Gaia* data have large uncertainties. This reduces the number of good quality and accurate proper motions measurements, which are typically found to have errors on the order of $\sim$20 km s^{-1}. All of these factors can effectively hide any rotation signal present on the plane of the sky. Future *Gaia* data releases are needed to confirm these results.

We found that the YMR and OMP subpopulations display different kinematics. Nevertheless, using *Gaia DR2* data for stars in both subpopulations we found they are comoving in 3D space. This suggests these two subpopulations are dynamically bound, adding substantial evidence against a chance alignment between them.

3.5.2 YMR: Evidence of In-situ Formation

Young sub-components in NSCs have been detected in different types of galaxies (e.g., early- and late-type). These young structures are more centrally concentrated and flattened (Seth et al., 2006; Carson et al., 2015; Feldmeier-Krause et al., 2015; Nguyen et al., 2017). A similar central concentration is found in ω Cen (van de Ven et al., 2006), a presumed former NSC.

In Chapter 2, we found evidence to suggest that the YMR subpopulation formed $\sim$3 Gyr ago likely in situ in a star-formation gas disk. In addition, we found that this subpopulation is the most centrally concentrated and the most flattened, with an ellipticity of 0.31±0.10.

In this chapter, we add that the YMR subpopulation has a rotation amplitude of $\sim$5 km s^{-1}, reaching a maximum rotation of $\sim$ 8 km s^{-1}, consistent with the high degree of flattening that we found. In contrast, the OMP subpopulation shows a small rotation of 0.7 km s^{-1}, but it shows an amount of flattening similar to other clusters with higher rotation ($\varepsilon \sim 0.15$). We will discuss this in the next section. From N-body simulations, Mastrobuono-Battisti & Perets (2013, 2016) found that the young structures can survive despite being embedded in an older population. Moreover, they are found to rotate faster than the population in which they are embedded in. Given the significant different kinematics of these populations it appears likely that the small difference observed in ellipticity is a real one. A representative case of a young stellar disk is observed in the Milky Way NSC (Feldmeier-Krause et al., 2015).

3.5.3 Kinematic Effects on the OMP Stars by the YMR

The formation and kinematics of the YMR subpopulation can affect the kinematics and shape of the population in which they were born. We found that the OMP subpopulation has a low rotation of $A_{rot} = 0.72 \pm 0.54$ km s^{-1}, with an ellipticity of $\varepsilon = 0.16 \pm 0.06$. In the $(V/\sigma_0, \varepsilon)$

diagram we observe that the OMP subpopulation (blue filled square) is more flattened than most of the GCs rotating at similar speed, and is similar to the most flattened clusters, e.g., ω Cen (black diamond), M22 (black pentagon), which seem to rotate even faster.

We perform simulations considering a disk-like centrally concentrated YMR population, embedded in an initially spherical and five times more massive OMP population. The two populations co-evolve for 2 Gyr, which is the estimated age for the young population observed in M54. At the end of the simulation, the YMR population, which is born in a disc because of the angular momentum of the progenitor gas, relaxes evolving towards a more spherical configuration and redistributing its angular momentum among the OMP stars. As a consequence of this process, the YMR disc slows down its rotation. At the same time, the OMP population acquires the angular momentum lost by the younger stars, decreases its velocity dispersion in the z direction and becomes slightly more flattened. This phenomenon could, at least partially, explain the ellipticity observed for the OMP population. Previous stellar populations, born in a disc, could have also contributed to the flattening of the OMP population leading to a more significant final effect, and shaping the present morphology of the OMP population.

Past mergers could have increased the ellipticity of the system, but would have also significantly affected its kinematics, producing a higher rotational signal than that observed in M54 (Tsatsi et al., 2017; Mastrobuono-Battisti et al., 2019). If the YMR subpopulation formed in a central disc that relaxed, leading to the observed OMP population flattening, we predict a radially-increasing velocity anisotropy for the YMR population, with β_z down to values smaller than 0.6 outside the half-mass radius of the cluster. The OMP population has a slight radial increase in the anisotropy profile. Future *Gaia* observations will be able to verify these predictions at least in the outskirts of the cluster.

In Chapter 2, we found different spatial distributions for the OMP and YMR subpopulations, with the YMR being the most centrally concentrated. Mastrobuono-Battisti & Perets (2013, 2016) also found that after 12 Gyr these two structures are not fully mixed, thus showing different distributions. In the simulations presented in this work we also observe that after 2 Gyr of evolution (close to the age of the YMR subpopulation) the two populations are not yet fully mixed, and the YMR subpopulation is found to be still more centrally concentrated than the OMP subpopulation.

3.5.4 OMP: Remnant of a Cluster Merger

In Chapter 2, we found that the OMP subpopulation displays a large spread in both metallicity and age. A large spread in metallicity alone can be explained by self-enrichment during the formation (Bailin, 2018), but it does not explain the large spread in age. Thus, we suggested that this could be the result of a merger event between two or more clusters that fell into the central region of the host, as suggested through simulations (e.g., Amaro-Seoane et al., 2013; Gavagnin et al., 2016; Bekki & Tsujimoto, 2016; Khoperskov et al., 2018; Mastrobuono-Battisti et al., 2019).

From the simulations point of view presented in this chapter, the formation and evolution of the YMR subpopulation alone could explain the shape and kinematics of the OMP. However, this does not explain the large spread in both age and metallicity we found in this subpopulation.

The final rotation of two merged clusters strongly depends on the conditions, as the orbital configuration and relaxation conditions of the merging clusters, do not always result in a high-rotating structure (Mastrobuono-Battisti et al., 2019). From the kinematics, we cannot be sure that two merging clusters were actually involved in the formation of the OMP subpopulation, but neither discard this possibility. Further high precision observations and more detailed simulations appropriate to mergers in the Sgr potential may help shed light on whether this process may have contributed to the build-up of the OMP population in the Sgr dSph.

3.5.5 Comparison with ω Cen

The similarities between NSCs in dwarf galaxies and high-mass, metal complex GCs suggest that such GCs might be former nuclei of dwarf galaxies accreted by the Milky Way (Zinnecker et al., 1988; Böker, 2008; Da Costa, 2016). One of the most likely former nuclei is ω Cen, which is the most massive GC in the Milky Way ($3.55 \pm 0.03 \times 10^6 M_\odot$, Baumgardt & Hilker, 2018). It presents a large spread in both iron (Johnson & Pilachowski, 2010) and age (Hilker et al., 2004; Villanova et al., 2014) and multiple stellar populations (Milone et al., 2017a; Bellini et al., 2017b), which present different kinematics (Bellini et al., 2018). These properties, and their similarity to what we have found in M54, make a strong case for ω Cen to be a stripped NSC that once resided in a dwarf galaxy now accreted by the Milky Way (Lee et al., 1999; Majewski et al., 2000; Bekki & Freeman, 2003; Carretta et al., 2010b). Using N-body simulations, Ibata et al. (2019a) found that the “Fimbulthul” structure detected with the *Gaia DR2* observations (Ibata et al., 2019b) could be a tidal stream of ω Cen. This provides important hints for the search of the escaped ω Cen stars, and to find potentially stars that likely belonged to its progenitor.

Observations of ω Cen and M54 suggest that ω Cen could be in a more advanced “stripped nuclei stage” than M54 (e.g., Carretta et al., 2010b; Bellazzini et al., 2008), since M54 is still observed at the photometric center of its host galaxy (Ibata et al., 1994) which is in ongoing disruption by the tidal field of the Milky Way (Ibata et al., 1997).

As other GCs, ω Cen presents ellipticity variations as a function of radius (Geyer et al., 1983), and is found to be one of the most flattened Milky Way GCs (Meylan, 1987). As we mentioned in Section 3.2.3, there is a correlation between the amount of rotation of a cluster and its ellipticity (Fabricius et al., 2014; Kamann et al., 2018), which has been detected for ω Cen (e.g., Meylan & Mayor, 1986; Bianchini et al., 2013, 2018; Kamann et al., 2018). ω Cen behaves close to an isotropic oblate rotator in the inner parts ($< 10\farcm$), becoming more anisotropic at larger radii, probably due to the tidal effects by the Milky Way (van de Ven et al., 2006) which do not affect the inner parts of the cluster. For M54, we find a difference of $\Delta\varepsilon = 0.09$ between the ellipticity estimated over the entire FOV ($\sim 2.5\times$ $\mathrm{R_{HL}}$) and at the half-light radius. Being cautious with the ellipticity uncertainties, this might suggest how the ellipticity for M54 varies as a function of radius, becoming more flattened at larger radii. From our $(V/\sigma_0, \varepsilon)$ diagram (see Figure 3.5) we observe that M54 is close to the isotropic oblate rotator relation when looking at its half-light radius, showing low rotation with a small degree of flattening. Watkins et al. (2015a) used proper motions to show that M54 is isotropic out to the half-light radius. However, this does not imply that the cluster cannot display anisotropy at larger radii. We observe that M54 becomes more anisotropic when measuring these values over the entire FOV ($\sim 2.5\times$ $R_{\rm HL}$). For the observations of M54, further analysis and information are needed to confirm and constrain its presumed radial anisotropy.

Additionally, a disk-like component was detected in ω Cen by van de Ven et al. (2006). We found a similar structure in M54 corresponding to the YMR subpopulation.

Although small differences exist between ω Cen and M54, the similarity of their subpopulations and their morphology and kinematics provides additional evidence that ω Cen is, in fact, the nucleus of a stripped dwarf galaxy.

3.6 Conclusion

In this chapter, we continued the characterization of the stellar subpopulations in M54 with the kinematic extraction. M54 is the closest extragalactic NSC, at a distance where stars can be resolved and characterized, enabling the distinction of the stellar subpopulations. In studies of extragalactic NSCs, the different stellar populations cannot be easily resolved, restricting the kinematic analysis to the nucleus as one single structure. In M54 we have the opportunity to directly compare the kinematics for the nucleus considering all the stars in the sample (i.e. like one single structure), as is usually done for extragalactic NSCs, and for the different subpopulations. We present the kinematics for two cases: (i) all M54 star members with no distinction, and (ii) for the subpopulations detected in M54 in Chapter 2.

We found that all three subpopulations show different velocity dispersion profiles, with the YMR and IMR subpopulations following a flat distribution. On the contrary, the OMP subpopulation is well-defined by a Plummer profile. We find that all populations show a different amount of rotation. The YMR subpopulation shows a considerable amount of rotation, followed by the IMR subpopulation which also rotates but more slowly. We detect a weak signal of rotation for the OMP subpopulation (< 1 km s^{-1}). Hence, the findings from the kinematic analysis suggest that the subpopulations do not have a common origin, as we previously suggested based on our findings in Chapter 2.

From these findings together with those in Chapter 2, we suggest the following conclusions:

- From our large sample of stars, we find that all populations have the same systemic velocity, proving they are spatially coincident. Additionally, cross-matching with the data from *Gaia DR2*, we find that the stars in the OMP and YMR are comoving in 3D space, discarding chance alignment.

- The YMR subpopulation displays a high amount of rotation. This added to the fact that it is more flattened and more centrally concentrated, strongly favors the in-situ formation scenario from enriched gas accreted at the center of M54.
- The OMP subpopulation appears more flattened than typical GCs rotating at the same speed. The *N*-body simulation emulating the YMR-OMP system in M54 presented in this Chapter suggests that this could result from the angular momentum lost by the YMR stars which is subsequently acquired by the OMP population, thus decreasing its velocity dispersion in the z direction and becoming more flattened. However, this alone does not explain the high iron and age spread this population presents, which we suggested to be signs of a merger event between two or more GCs in the center of the host. The merger scenario cannot be ruled out since depending on the initial conditions the merger of GCs can or cannot end in a rotating structure.
- The current information we obtain from the IMR subpopulation does not allow us to constrain if its stars are dynamically bound to the nucleus. However, the kinematics of this population is consistent with these stars being part of the field of the Sgr dSph.

From the kinematic analysis of M54, for the whole sample of stars, we observe that either by radial velocity, rotation or velocity dispersion information it would not be possible to realize that M54 actually host multiple populations. Kinematics provide valuable information, but here we show how crucial it is to resolve the stars and characterize them. The possibility of performing both analyses has surely provided valuable knowledge of the properties of each subpopulation and the history of M54.

The kinematic analysis presented in this chapter certainly adds an essential piece of information to the understanding of M54 and its subpopulations.

Chapter 4

Discrete Dynamical Modeling of M54

The kinematic properties of stellar systems contain a record of the events that they experienced throughout their evolution, that could be revealed via comprehensive dynamical modeling. Stars follow certain orbits which are determined by the gravitational potential. Hence, knowing the details of these orbits we can trace the mass of the system and how it is distributed.

This is the idea behind the modeling approach developed by Martin Schwarzschild 1979. It uses the superposition of a library of representative orbits in a spherical or axisymmetric galactic potential, to model and interpret the line-of-sight velocity profiles of galaxies (e.g., Rix et al., 1997; van der Marel et al., 1998; Cappellari et al., 2002; Verolme et al., 2002; Gebhardt et al., 2003). This allows for much more general models that are not restricted to spherical shapes or isotropic velocity distributions, as previous models required. This was not in line with observations. Pushing forward, van de Ven et al. (2006) applied this method, also including proper motion information for the globular cluster ω Cen, getting the three-dimensional velocities of the stars, and being able to constrain the distance to the cluster accurately. With the large amount of highly accurate data available today, it becomes possible to combine the line-of-sight velocities and proper motions for a large amount of targets (e.g., Watkins et al., 2015b). This combination helps to break the degeneracy between mass and orbital anisotropy and thus improves the recovery of mass profiles in spherical systems (Binney & Mamon, 1982).

The Schwarzschild orbit superposition approach is a direct and accurate approach to the modeling of the dynamics of stellar systems, however, it is computationally expensive and presently requires spatial binning of the data. This could become problematic and lead to loss of information, especially in small data sets. An alternative modeling approach is based on the Jeans equations (Cappellari, 2008). It requires more a priori assumptions about the modeled system, but is much faster and can easily be discretisized to take full advantage of the available observations. Watkins et al. (2013) presented a discrete implementation of the Jeans modeling approach using maximum-likelihood methods. In Watkins et al. (2013), the technique was applied to ω Cen, and a similar application was presented for the globular cluster M15 in den Brok et al. (2014a).

Due to the discrete nature of this technique, Watkins et al. (2013) showed that it is effective for cleaning the contamination of foreground stars from the sample, which used to be a problem for integrated line-of-sight velocity maps.

Studies revealed that dwarf galaxies host multiple populations, that exhibit clear differences in their metallicity and phase-space distribution (e.g., Battaglia et al., 2008; Walker & Peñarrubia, 2011; Amorisco & Evans, 2012). It is observed that the metal-rich population is more centrally concentrated than the metal-poor one. The kinematics of these populations can provide important insights to understand how they formed. Under this motivation, to fit a dynamical model and to separate the multiple populations together, Zhu et al. (2016a) presented chemo-dynamical models. To this aim, the authors extended the discrete Jeans anisotropic models presented in Watkins et al. (2013) to include multiple populations, all under the same gravitational potential, but characterized with their own spatial, chemical and dynamical distributions. Chemo-dynamical models show to be an exquisite tool to separate the contribution of each population in the galaxy, extracting their kinematics and providing accurate constraints of the galaxy parameters (e.g., rotation, anisotropy, dark matter). For another application of this technique see Zhu et al. (2016b), where the authors include three stellar populations for the giant elliptical galaxy NGC 5846.

Dynamical models applied to the central region of GCs can detect the presence of an intermediate mass black hole. However, this low-mass black holes are difficult to detect and accurate high resolution data are crucial, especially within the small sphere of influence of the black hole. So far, no definitive proof of their existence in GCs has been achieved. However, studies suggest that some GCs are strong IMBH host candidates: e.g., ω Cen (Noyola et al., 2008; Jalali et al., 2012; Baumgardt, 2017), G1 Gebhardt et al. (2005), NGC 6388 (Lützgendorf et al., 2011). Additionally, in M54, two studies have reported a possible detection ($M_{BH} \sim 10^4 M_\odot$, Ibata et al. 2009; Baumgardt 2017). These are all high mass and complex globular clusters that are likely to be stripped galactic nuclei. Confirming the presence of an IMBH at their center would add another piece of evidence to this suggested stripping scenario.

As presented in Chapter 2 and 3, we have characterized the multiple populations in M54 by age-metallicity and kinematics: YMR, IMR, and OMP. In this chapter, we present the preliminary results on the discrete dynamical models of M54. To start, we will model a subset of the stars that we have identified as members of M54 (see Section 2.2.2). However, making use of our chemical and line-of-sight velocity information for the stars from the MUSE data presented in Chapter 2, the goal is to perform chemo-dynamical models including all three sub-populations in a similar approach to Zhu et al. (2016a,b). Through the dynamical modeling we aim to constrain the existence and mass of the putative IMBH in M54 (see Section 5.2.1).

4.1 Data

4.1.1 Stellar Sample

For the dynamical modeling, we use the data set presented in Chapter 2. We use the coordinates and line-of-sight velocity information (see Section 2.2.1). In this chapter, we present two tests: (i) for all member stars within $1'\!.0$ radius where we fit for the mean line-of-sight velocity of the cluster and its M/L ratio, under the assumption of a non-rotating isotropic cluster; (ii) for a randomly selected sample of 500 stars within $1'\!.0$ radius, where we also fit for rotation and anisotropy of the cluster in an axisymmetric potential in addition to the before-mentioned parameters. We restrict ourselves to this small subsample for the models including rotation which is significantly more computationally heavy to keep the computation time reasonable for our initial tests.

4.1.2 Multi-Gaussian Expansion

To perform the dynamical modeling we need a simple description of the spatial stellar distribution of the cluster. For this purpose, we apply the Multi-Gaussian expansion (MGE) technique, a method that has been widely used to obtain a well-described surface brightness profile of stellar systems, such as galaxies and star clusters (Emsellem et al., 1994; Cappellari, 2002). The model consists of a superposition of Gaussian components, where each of them is defined by a central brightness, a major-axis dispersion and flattening (q).

This method can be applied to images (two-dimensional) or a radial surface density profile (one-dimensional). For M54, we use the one-dimensional surface brightness profile published by Noyola & Gebhardt (2006). The authors obtained the profile based on photometric *HST* WFPC2 data in the filter F555W. We obtain the MGE model using the MGE-Fit-Sectors method[1] (Cappellari, 2002). The best fitting MGE parameters are presented in Table 4.1, and Figure 4.1 illustrates the decomposition of the observed surface brightness profile into our best-fitting MGE components. The blue lines show the individual Gaussian components. The red and black lines represent the total surface brightness and the surface brightness profile from Noyola & Gebhardt (2006). The coincidence between these two lines show the good performance of the MGE method.

4.2 Maximum-likelihood Analysis

The main point of discrete dynamical modeling is to avoid the consequences of binning the data, therefore, the comparison between the models and the data is based on a maximum-likelihood approach.

---

[1] `https://www-astro.physics.ox.ac.uk/~mxc/software/#mge`

Table 4.1. MGE for M54.

k	L_k ($L_\odot$ pc^{-2})	σ (arcsec)	q_k
1	8854.212	0.351	1.0
2	13275.344	1.046	1.0
3	30213.074	2.430	1.0
4	28631.904	4.975	1.0
5	12924.703	9.737	1.0
6	3761.448	18.218	1.0
7	1111.804	31.971	1.0
8	289.285	57.744	1.0
9	58.177	114.761	1.0
10	9.080	287.720	1.0

Note. — L_k: central surface brightness. σ: dispersion along major axis. q_k: Projected fattening for the respective Gaussian component. In this case is spherical ($q = 1$) since we are using a one dimensional fit.

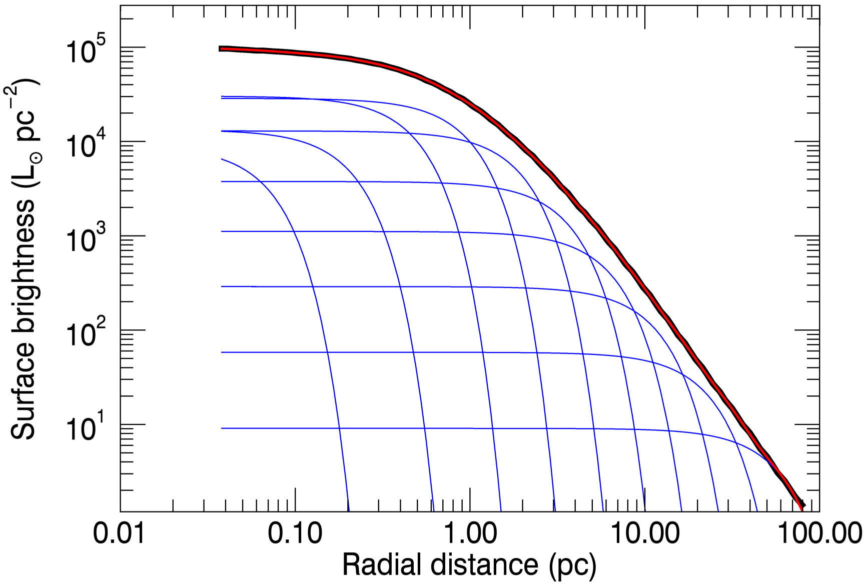

Figure 4.1 Surface brightness profile from the MGE model. The blue lines show the individual Gaussian components. The red line represents the total surface brightness, and the black line shows the surface brightness profile from Noyola & Gebhardt (2006).

Based on the detailed description on the likelihood function for the three-dimensional velocities presented by Watkins et al. (2013), here we briefly describe our case, when only line-of-sight information is available. For all the stellar sample we have coordinate information, which for the ith star is defined as (x_i, y_i). Since we do not have proper motions for M54, with only the velocity of each star – $v_{x_i} \pm \sigma_{v_i}$ – the velocity vector is reduced to $v_i = v_{z,i}$.

Defining Θ as a set of models to compare with the observed data, and Θ_j as the current model under comparison, the likelihood of the star i for a certain model j is defined as:

$$\mathscr{L}_{ij} = p(v_i, \sigma_{vi}, x_i, y_i | \Theta_j) \tag{4.1}$$

The total likelihood of the model ($\mathscr{L}_j$) correspond to the product of the likelihood of the model for each of the stars in the sample, thus:

$$\mathscr{L}_j = \Pi_{i=1}^{N} \mathscr{L}_{ij} \tag{4.2}$$

We find the maximum likelihood model by using the likelihood logarithm as $\ln L = \Sigma(\ln \mathscr{L}_j)$.

4.3 Performing Jeans Models

Watkins et al. (2013) demonstrated that this approach can easily account for contaminants (i.e., non-member stars) in the sample. However, in our first tests, we only include M54 member stars as derived in Chapter 2 (See Section 2.2.2).

When provided with only line-of-sight velocity data, the models constrain the first and second velocity moments at the coordinates of each star in the sample and make predictions for the proper motions. For running the models, we first compute the positions of the stars “x” and “y” from the center of M54 using the coordinate information of the stars and Eq. 1 in van de Ven et al. (2006), both expressed in units of arcseconds. The other three minimum inputs for the models are the projected tracer number density profile obtained from the MGE, the projected mass density profile, also from the MGE, and the distance. We set a distance of 28.4 kpc (Siegel et al., 2011). We work under the assumptions that the mass follows light as observed for GCs. For the mass component we use the same MGE as for the light component but we scale it with a mass-to-light ratio.

For our final models, we aim to include: anisotropy, rotation, inclination angle, black hole mass, and black hole scale length. For now, we present two tests where we fit: (i) for mean line-of-sight velocity of the entire cluster and mass-to-light ratio for all the member stars of M54 within a $1\farcm0$ radius, this means assuming a simple spherical, isotropic, non-rotating cluster; (ii) for a mean line-of-sight velocity, mass-to-light ratio, anisotropy (β), and rotation (κ) for a subsample of 500 member stars of M54 randomly selected within a 1.′0 radius. We only use a subsample of stars in the test (ii) since including the rotation parameter slows down the computation considerably.

In Figure 4.2 we present the parameters' posterior distributions as obtained via MCMC sampling for the first test. The MCMC sampled 1000 steps with 80 walkers considering all the member stars within a 1.′0 radius using `emcee` by Foreman-Mackey et al. (2013). The scatter plots show the two-dimensional distributions and the histograms represent the one-dimensional distribution for each parameter: mass-to-light ratio and mean velocity. From the converged part of the MCMC, we obtain a mean line-of-sight velocity of 141.4 ± 0.3 km s^{-1} and a median mass-to-light ratio of $2.70 \pm 0.07 M_\odot / L_\odot$.

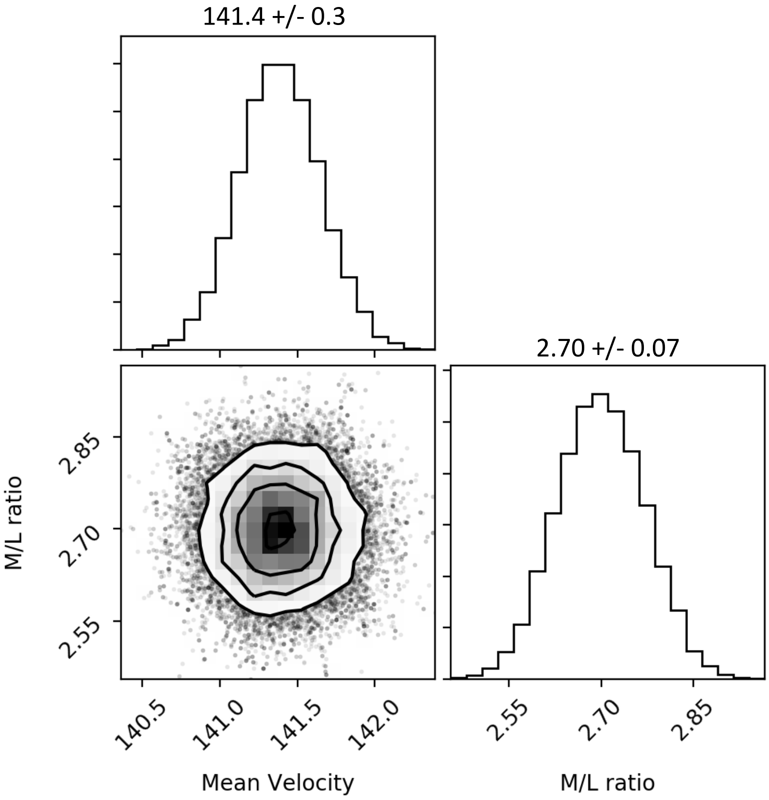

Figure 4.2 MCMC distribution for all M54 member stars within a 1.′0 radius. The scatter plots show the two-dimensional distributions. The histograms represent the one-dimensional distribution for each parameter: mass-to-light ratio and mean velocity.

We present in the top panel of Figure 4.3 the two-dimensional velocity dispersion profile from the predicted best-fitting model. The bottom panel shows the comparison of the one-dimensional velocity dispersion profiles from the model (solid red line) and from the data estimated in radial bins (blue circles).

In Figure 4.4 we present the MCMC distribution for the second test. This is for 400 steps with 80 walkers considering 500 member stars in a 1.′0 radius using `emcee` by Foreman-Mackey et al. (2013). The scatter plots show the two-dimensional distributions and the histograms represent the one-dimensional distribution for each parameter: mass-to-light ratio, mean velocity,

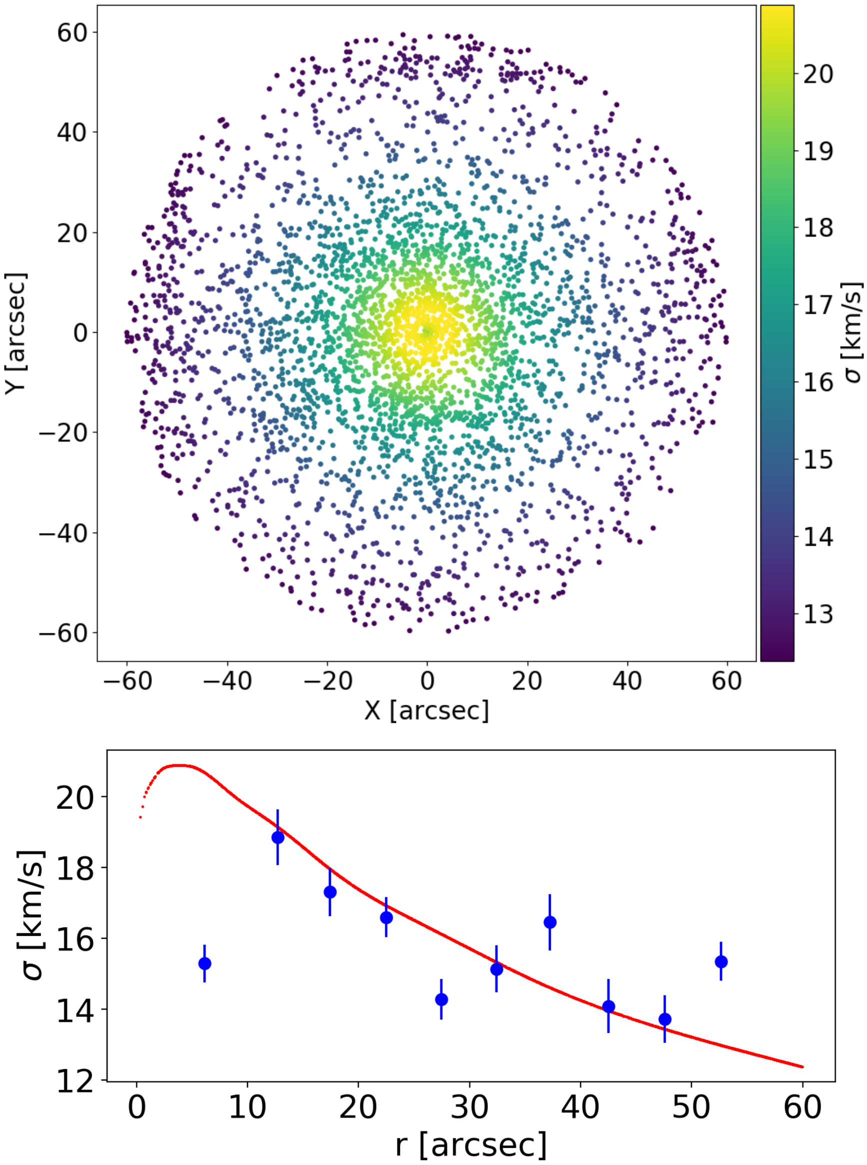

Figure 4.3 Top panel: two-dimensional velocity dispersion profile in z predicted by the best model for the sample of all members of M54 within 1′.0 radius. Bottom panel: one-dimensional velocity dispersion profile. The red solid line shows the velocity dispersion for the predicted model. The blue circles show the velocity dispersion profile estimated in radial bins from the data. The drop in observed velocity dispersion towards the center is due to crowding effects of the stars that limit the spatial resolution of our observations.

anisotropy (β), and κ (rotation). We obtain a mean line-of-sight velocity of 141.1 ± 1.4 km s^{-1}, a median mass-to-light ratio of $2.66 \pm 0.33 M_{\odot}/L_{\odot}$, median anisotropy of $\beta = -0.04 \pm 0.09$, and median $\kappa = -0.32 \pm 0.39$. We include in the top panel of Figure 4.5 the two-dimensional velocity dispersion profile (σ_z), and in the bottom panel, the comparison of the one-dimensional velocity dispersion profile from the model (red line) and the data (blue circles). In Figure 4.6, we present in the top panel the velocity (V_z) map based on the preliminary best-fitting model. The bottom panel shows the rotation profile from the best-fitting model (red line) and the data (blue circles).

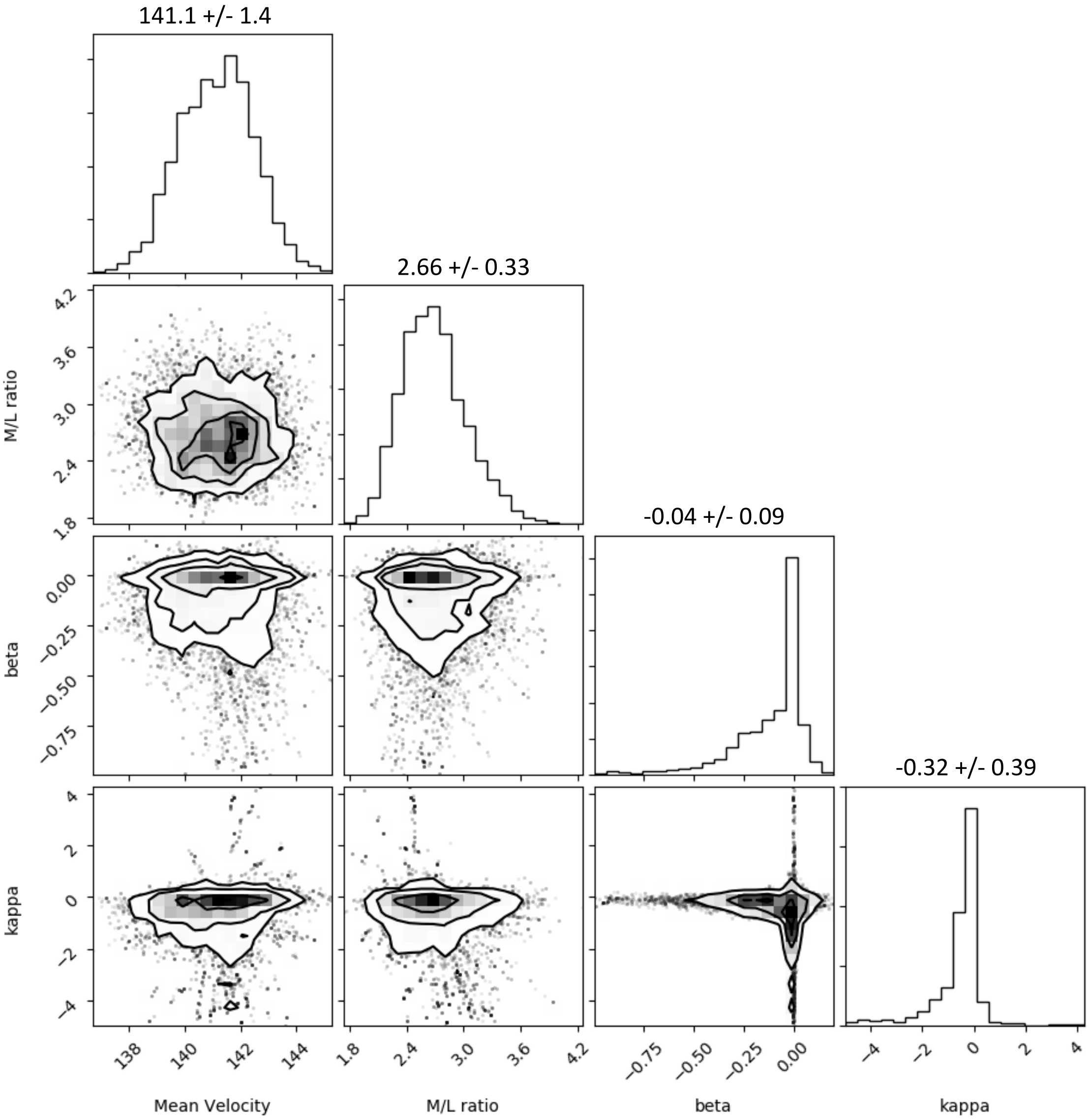

Figure 4.4 MCMC distribution for a subsample of 500 member stars in 1.′′0 radius. The scatter plots show the two-dimensional distributions. The histograms represent the one-dimensional distribution for each parameter: mass-to-light ratio, mean velocity, anisotropy, and rotation.

4.4 Discussion and Conclusion

In test (i), we assumed a simple spherical, isotropic, non-rotating cluster, thus fitting only for mean line-of-sight velocity of the entire cluster and mass-to-light ratio for all member stars inside 1.′0 radius. In test (ii) we selected 500 random member stars inside 1.′0 radius and fit a mean line-of-sight velocity, mass-to-light ratio, anisotropy (β), and rotation (κ).

We observe that in both tests the MCMC distribution has nicely converged giving a best-fitting model for M54. The mean line-of-sight velocity and mass-to-light ratio values are consistent between both cases. Their mean velocity are consistent with the value we obtain in the previous chapter (141.34 ± 0.18 km s^{-1}) for all M54 member stars. The mass-to-light ratio is consistent

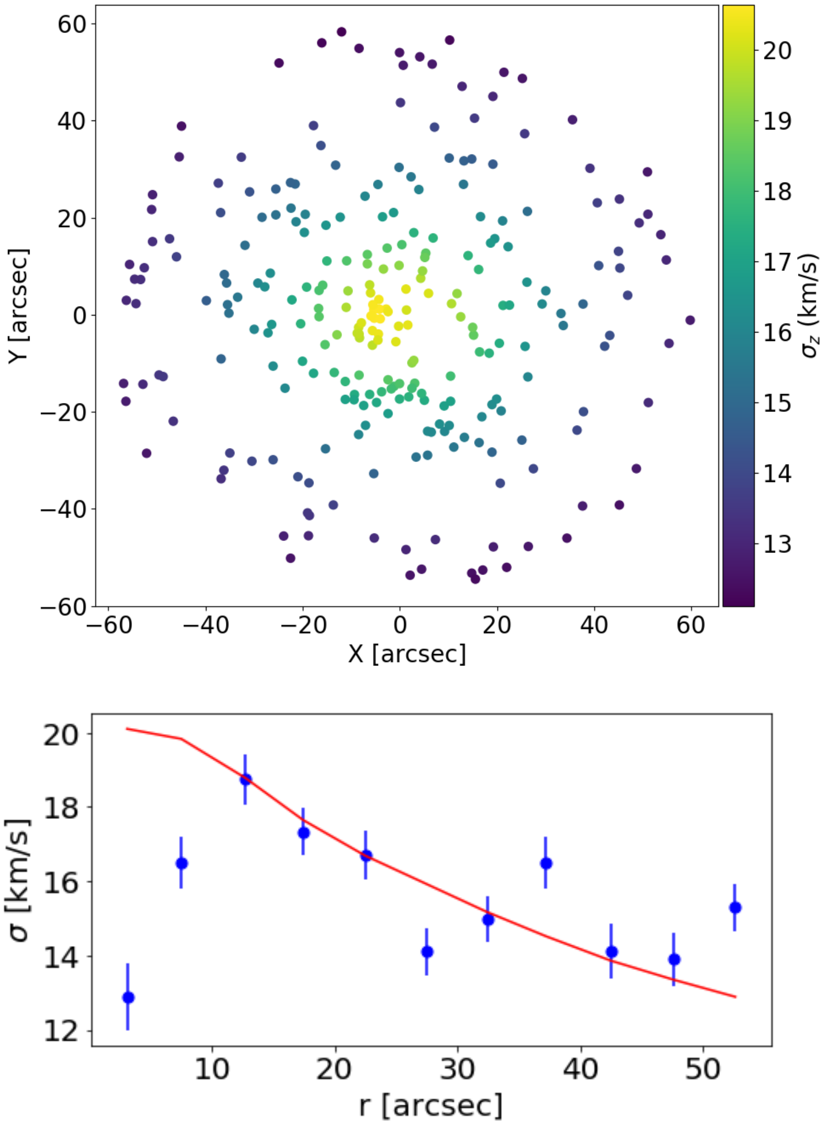

Figure 4.5 Top panel: two-dimensional Velocity dispersion profile in z. Bottom panel: one-dimensional velocity dispersion profile from the model for a subsample of 500 member stars of M54 (red line) and the data (blue circles). The drop in observed velocity dispersion towards the center is due to crowding effects of the stars that limit the spatial resolution of our observations.

with what is expected for old stellar systems that are not dark matter dominated. Our mass-to-light ratio in both tests are slightly higher than the value estimated by Baumgardt (2017) of $\mathrm{M/L} = 2.18 \pm 0.20$ (V-band).

The velocity dispersion in the innermost 20.″0 show a high peak at ~ 20 km s^{-1} in both tests. As presented in the model and data velocity dispersion profiles, we observe that they are highly consistent outside of 10.″0 radius. The differences in the central 20.″0 might be a consequence of the crowding effects in the center, where we are not able to extract all the stars that reside in this dense region. The lack of stars in the innermost region can affect the velocity dispersion

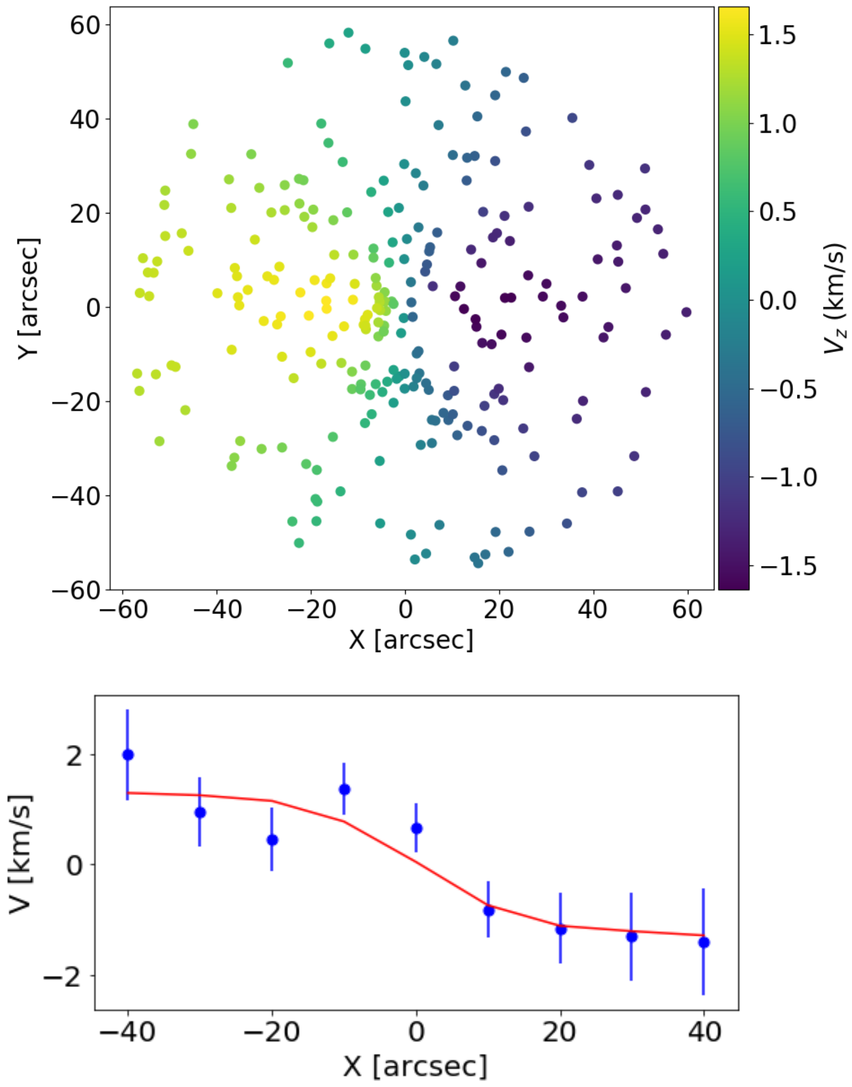

Figure 4.6 Top panel: velocity (V_z) map from the best-fitting model for a subsample of 500 member stars of M54 (red line). Bottom panel: rotation profile from the best-fitting model (red line) and from the data (blue circles).

estimate there. Extra data with better spatial resolutions is needed to address this issue. We will discuss this further in the Outlook (see Section 5.2.1).

In our tests, the models show evidence for a good recovery of the dynamical properties of M54 compared to the values from our work and the literature. The common parameters between the two tests are consistent showing that with 500 stars we are obtaining good estimates for the dynamical properties of M54. The tests are promising, and make us confident that we will be able to obtain accurate and precise constraints on the properties of M54 once we include our entire sample. The next step will then be to construct a chemo-dynamical model for the different subpopulations of M54 using the stellar properties we have derived in Chapter 2.

Chapter 5

Conclusions & Outlook

5.1 Conclusions

The fraction of galaxies hosting a nucleus reaches a maximum for galaxies with stellar masses between 10^8 and $10^9 M_\odot$. Most of the NSCs studies are dedicated to this galaxy mass range, providing a vast amount of information about those nuclei. However, there are not many studies on NSCs in the low-mass regime, so we have limited knowledge about their structural and stellar population properties.

The hierarchical build-up scenario for galaxies suggests that large galactic structures are formed by the accretion of smaller ones. The large number of stellar streams surrounding the Milky Way provides proof of this scenario, showing the past or current accretion of dwarf galaxies together with their GC system (in different stages of their disruption process). From the nucleation fraction studies, we know that a high number of these galaxies host an NSC which is expected to survive the disruption of its host, due to its high stellar density. Thus, it is presumed that the NSC remnants of accreted dwarf galaxies are observed today as the most massive, metal complex GCs (e.g., ω Cen in the Milky Way, and G1 in Andromeda).

In this context, the nucleated Sgr dSph provides a unique laboratory to understand the unknown nature of low-mass galaxy nuclei. The Sgr dSph is under the strong effects of the tidal field of the Milky Way. It shows an advanced stage of disruption, evidenced by the large stellar stream around the Milky Way extending over more than 360°. In spite of this advanced stage of disruption, it hosts an NSC in its photometric center: M54.

M54 has been classified as a GC since its discovery by Messier in 1778, long before the detection of its host by Ibata in 1994. In the literature, the name M54 is attributed only to the metal-poor stars observed in the system, while the metal-rich stars are referred to as the nucleus of the Sgr dSph. To explain the spatial coincidence, it was suggested that M54 was a typical GC that fell into the center of its host by dynamical friction effects. However, in extragalactic NSCs the distinction of multiple populations coming from accreted GCs or from stars formed in situ is not an easy task, and our findings suggest that referring only to the metal-poor population as M54 might not be the ideal approach.

In this Thesis, we presented an unprecedented data set of M54 from MUSE, a 4×4 mosaic covering out to ~ 2.5 times the effective radius. We extracted over 7 000 stellar spectra, with ~ 6600 being members of M54. Through Gaussian mixture models, we were able to disentangle three subpopulations with clear differences in metallicity and age, constraining the SFH of this nucleus. From this analysis we recovered (i) a young metal-rich (YMR) subpopulation, with ages of 2.2 Gyr and average metallicity $[\mathrm{Fe/H}] = -0.04$; (ii) an intermediate-age metal-rich (IMR) subpopulation, with ages of 4.3 Gyr and metallicity $[\mathrm{Fe/H}] = -0.29$; and (iii) an old metal-poor (OMP) subpopulation, with ages of 12.2 Gyr and metallicity $[\mathrm{Fe/H}] = -1.41$. Using this characterization, we extracted the kinematics of these subpopulations and found that they present clear mutual differences. The SFH and kinematics that we obtain for the different subpopulations suggest they have different origins and that the formation of this nucleus stopped ~ 2 Gyr ago.

Through this large stellar sample, we found that all the subpopulations show the same systemic velocities within their uncertainties. We estimate that the OMP and YMR subpopulations have the same centroid, and while we could not converge to a centroid value for the IMR subpopulation, it is still possible that all three subpopulations have the same centroid. Additionally, through *Gaia DR2* data, we observe that the stars in both the YMR and OMP subpopulations are comoving in 3D space. This evidence strongly supports that these populations are spatially coincident, discarding chance alignment by projection effects between the multiple populations.

From all the evidence we presented in this Thesis, we suggest to the astronomical community to return to the original naming of “M54”, as in the time of its discovery by Messier, when no distinction between the populations was possible. The evidence suggests that M54 does not behave as a normal metal-poor GC but rather as a complex NSC.

The main conclusions from our findings for the subpopulations in M54 are as follows:

- The YMR subpopulation is more flattened and more centrally concentrated than the other two subpopulations. It displays a strong signature of rotation and follows a flat velocity dispersion profile. Being cautious about the uncertainties in the ellipticity, our findings suggest consistency with the observations in other stellar clusters, in which faster rotators display a higher degree of flattening. All these characteristics strongly suggest that the formation of the YMR subpopulation occurred in situ from gas retained in the deep potential of M54 around 3 Gyr ago. There are two possible scenarios that favor the in-situ formation of the YMR subpopulation. First, since it is presumed that the first big encounter between the Sgr dSph and the Milky Way occurred around 3 Gyr ago, this process could have channeled gas into the nucleus. Hence, forming this new population before the total stripping of the gas after the second encounter $\sim$1 Gyr ago. In the second scenario, the YMR subpopulation could have formed from gas ejected from high-mass and metal-enriched IMR stars at larger radii retained in the potential well of the OMP subpopulation.

This type of young metal-rich structures embedded in older metal-poor populations are commonly found in NSCs (e.g., the Milky Way). In these systems, the young metal-rich structure is more centrally concentrated and displays high rotation in comparison to the old metal-poor structure.

- The OMP subpopulation presents a high spread in both metallicity ([Fe/H]) and age. It also appears considerably flattened. We detect a weak signal of rotation in this population and the velocity dispersion profile is well-represented by a Plummer model. In comparison with typical GCs, the OMP subpopulation displays a similar amount of rotation but with a higher degree of flattening. To explain the high spread in metallicity and age, we suggest that this population is the remnant of the merger of two or more GCs that spiraled into the center of the galaxy by dynamical friction effects. We emulate the YMR-OMP system of M54 using N-body simulations obtaining similar results to the observations of these two subpopulations. These results show consistency with the YMR subpopulation being formed in situ in the center of the OMP subpopulation. In the simulations, we found that the angular momentum of the YMR population is transferred to the OMP subpopulation. Hence, the OMP subpopulation decreases its velocity dispersion in the z direction and becomes more flattened. This alone can explain the flattening and low rotation observed in the OMP subpopulation, however, it does not explain the high spread in metallicity and age. We cannot discard that a merger between GCs has contributed to the rotation and flattening of this subpopulation since such events could also not end in a rotating final structure, depending on the initial conditions.
- The IMR subpopulation displays a broad range of ages and metallicities, which are consistent with the stars in the field of the Sgr dSph. We observe that this population is the least centrally concentrated, but still significantly centrally peaked as expected for stars in the central regions of galaxies (including non-nucleated ones). This population displays a certain degree of rotation and follows a flat velocity dispersion profile. With the current information, we cannot constrain if these stars are actually dynamically bound to M54.

M54 has proven to be a complex system, but at the same time, an excellent and unique test case. In this NSC, we observe evidence that two formation mechanisms have occurred: (i) infall of two or more GCs, which merge to form a single high-mass cluster with a large metallicity spread (OMP subpopulation), and (ii) in-situ star formation from enriched gas in the nucleus (YMR subpopulation). For M54, it seems that the first scenario is the key for the second to be able to occur. The SFH of M54 allows us to understand the formation and growth processes of NSCs in low-mass galaxies. It shows us observational evidence which suggests that in spite of the strong tidal field of the Milky Way and the advanced stage of the disruption of its host, M54 still found a way to form a new population of young and metal-enriched stars.

Our dynamical modeling seems promising to constrain the dynamics of M54 and its subpopulations. For our initial tests, we found that the models converge, and the parameters values are consistent with what we expect for this object. The chemical characterization presented in this Thesis will be crucial for the chemo-dynamical modeling and to constrain the existence and mass of the IMBH that is presumed to reside at the center of M54.

5.2 Outlook

With the work presented in this Thesis, we have contributed detailed information on M54 and its star formation history to the astronomical community. This study importantly contributes to the understanding of low-mass galaxy nuclei through an exemplary case study. Furthermore, this MUSE data set is a rich source of information with a strong potential that can be further exploited. It offers a broad spectrum of opportunities, from using the information we presented for the stars and their respective subpopulation to new projects beyond the goal of this Thesis.

5.2.1 An IMBH Hosted by M54?

The hunt for IMBHs in GCs is ongoing, as their detection has been suggested but not yet confirmed (e.g., Gebhardt et al., 2005; Noyola et al., 2008; Lützgendorf et al., 2011; Baumgardt, 2017). The existence of these IMBH in high-mass, metal complex GCs would strongly support the stripped nuclei scenario. The fact that GCs and NSCs are such dense objects leads to one of the major limiting factors for the detection of IMBHs, the highly crowded central regions. This makes it difficult for current observational facilities to reach and resolve individual stars in the innermost region, the sphere of influence of the putative IMBH. For an accurate constraint on the existence and the mass of this IMBH in the center of M54 – where the crowding is a limiting factor – better spatial resolution in the innermost center is crucial.

Our initial tests on the dynamical modeling of M54 presented in Chapter 4 are promising and suggest a good constraint on the dynamical properties of M54 and its subpopulations. M54 is presumed to host an IMBH of $\sim 10^4 M_\odot$ (Ibata et al., 2009; Baumgardt, 2017), and this modeling technique can potentially reveal its existence and constrain its mass. To this aim, we acquired two new central MUSE pointings on M54 with adaptive optics assistance which considerably help with the crowding issues in the innermost center of M54 (see Figure 5.1).

In addition to the 4×4 M54 mosaic acquired with MUSE with the wide field mode (WFM), we observed two extra MUSE pointings: (i) one pointing with the wide field mode plus adaptive optics (WFM-AO) for ground level correction, and (ii) one pointing with the narrow field mode (NFM) which provides diffraction limited observations. The MUSE WFM-AO pointing was acquired as part of the science verification programme 60.A-9181(A) (PI: Alfaro-Cuello) in August 2017. This mode has the same main characteristics (i.e., FOV, spatial sampling) as the WFM but the addition of adaptive optics that improves the quality of the observations. The MUSE NFM data were acquired under the science verification programme 60.A-9486(A) (PI: Alfaro-Cuello). This mode has a FOV of $7\farcs5 \times 7\farcs5$ with a spatial sampling of $0\farcs025$. In Figure 5.1 we show the comparison of the pointings: the WFM 4×4 M54 mosaic in the top panel; the WFM-AO in the bottom left panel; and the NFM in the bottom right panel. In these images, we see the stunning improvement reached with the NFM. We estimate a PSF size of $0\farcs65$ (mean value of the 16 pointings), $0\farcs53$, and $0\farcs08$, for the WFM, WFM-AO, and NFM, respectively.

With a preliminary analysis on the NFM data, we extract good quality stellar spectra for ~ 400 stars, reaching magnitudes of $I \sim 19$. Around ~ 220 stars are in the innermost $3\farcs0$ (~ 0.4 pc) of M54. This is three times the number of stars extracted from the WFM and WFM-AO data sets at this radius (~ 70 stars).

The new capabilities of MUSE with the NFM mode allow us to improve the extraction of stars in the innermost central region, where crowding is a serious issue for seeing limited data. We are able to considerably increase the number of stars for the three central arcseconds of M54, where kinematical data up to now have been affected by blending and thus highly uncertain velocity dispersion measurements. The inclusion of these data in the dynamical modeling will help us to detect or refute the existence of the putative IMBH in M54.

5.2.2 Star Formation History from Integrated Spectrum

Boecker et al. (2019) presented a new method to recover the accretion history of a galaxy based on its integrated spectrum. They derive the mass distribution of the galaxy in age-metallicity space, which allows them to separate the different populations considering chemical differences. Through empirical age-metallicity relations for galaxies at different masses they were able to identify the accreted stellar populations, moreover to constrain the stellar mass of their progenitor.

M54 is a good candidate to test this method because we can compare the star formation history obtained from the integrated spectrum with the one we obtained from the analysis of individual stars presented in this Thesis. The technique presented by Boecker et al. (2019) can be tested on the integrated good-quality spectra of the $\sim 6\,600$ member stars of M54 (in different phases of stellar evolution), and as a comparison, on the integrated MUSE cubes from which they were extracted. The available data represent a pool of possible test cases. Additionally, in the case of the integrated spectra from single stars, the recovery can be tested using different subpopulations or types of stars to evaluate their contribution.

Several tests have been carried out by Boecker et. al (in prep.) to constrain the best recovery of the star formation history of M54. Preliminary results are in agreement with the star formation history presented in this Thesis for individual stars.

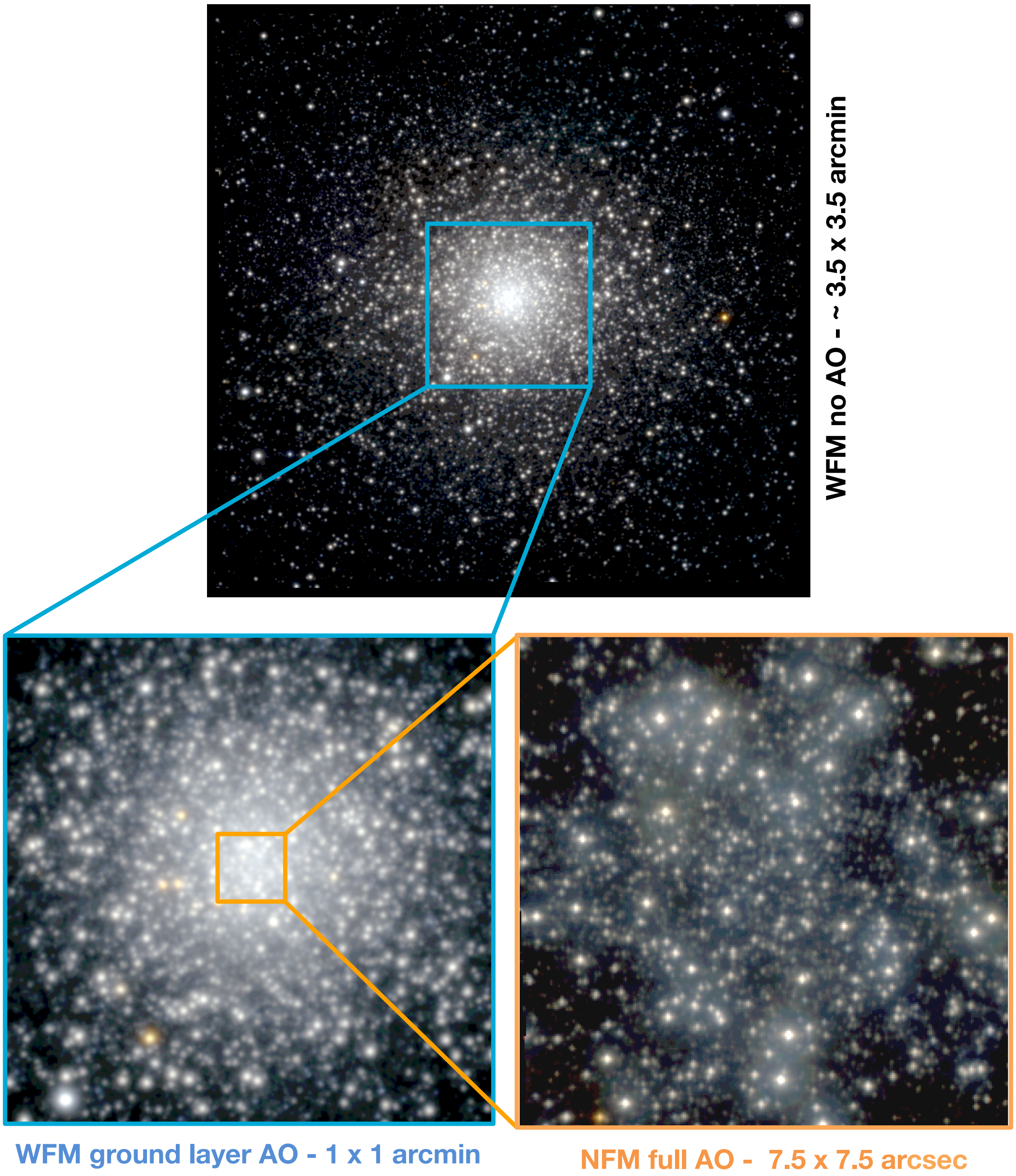
WFM no AO - ~ 3.5 x 3.5 arcmin
WFM ground layer AO - 1 x 1 arcmin
NFM full AO - 7.5 x 7.5 arcsec

Figure 5.1 Color images obtained from the MUSE data of M54 using synthetic *i*, *r*, and *z* filters. The images correspond to: the WFM 4 × 4 mosaic (top panel), the WFM-AO (bottom left panel), and the NFM (bottom right panel). North is up and east is to the left.

5.2.3 Photo-chemical Evolution Model

Vincenzo et al. (2016) presented a photo-chemical model to recover the observed color-magnitude diagram of galaxies. The authors applied this model to the Sculptor dSph and found a good reproduction of the observed properties. They show that the model reproduces the features of stars in different evolutionary phases in the galaxy, in particular those of red giant branch, horizontal branch, and asymptotic giant branch stars.

Considering that we have metallicity information for a large sample of stars in M54, this model is an interesting technique to apply to our data set. The goal of our new collaboration is to use this photo-chemical evolution model to reproduce the characteristics we observe in the stellar populations of M54 (see the details of this approach in Vincenzo et al., 2016).

Bibliography

Afanasiev, A. V., Chilingarian, I. V., Mieske, S., et al. 2018, MNRAS, 477, 4856

Ahn, C. P., Seth, A. C., den Brok, M., et al. 2017, ApJ, 839, 72

Ahn, C. P., Seth, A. C., Cappellari, M., et al. 2018, ApJ, 858, 102

Akaike, H. 1974, IEEE Transactions on Automatic Control, 19, 716

Amaro-Seoane, P., Konstantinidis, S., Brem, P., & Catelan, M. 2013, MNRAS, 435, 809

Amorisco, N. C., & Evans, N. W. 2012, MNRAS, 419, 184

Antonini, F. 2013, ApJ, 763, 62

Antonini, F., Barausse, E., & Silk, J. 2015, ApJ, 812, 72

Arca-Sedda, M., & Capuzzo-Dolcetta, R. 2014, MNRAS, 444, 3738

Armandroff, T. E., & Zinn, R. 1988, AJ, 96, 92

Bacon, R., Vernet, J., Borisova, E., et al. 2014, The Messenger, 157, 13

Bailey, M. E. 1980, MNRAS, 191, 195

Bailin, J. 2018, ApJ, 863, 99

Balbinot, E., & Gieles, M. 2018, MNRAS, 474, 2479

Barnes, J. E., & Hernquist, L. 1996, ApJ, 471, 115

Bastian, N., & Lardo, C. 2018, Annual Review of Astronomy and Astrophysics, 56, 83

Battaglia, G., Helmi, A., Tolstoy, E., Irwin, M., Hill, V., & Jablonka, P. 2008, ApJ, 681, L13

Baumgardt, H. 2017, MNRAS, 464, 2174

Baumgardt, H., & Hilker, M. 2018, MNRAS, 478, 1520

Bekki, K., Couch, W. J., Drinkwater, M. J., & Shioya, Y. 2003, MNRAS, 344, 399

Bekki, K., & Freeman, K. C. 2003, MNRAS, 346, L11

Bekki, K., & Tsujimoto, T. 2016, ApJ, 831, 70

Bellazzini, M., Bragaglia, A., Carretta, E., Gratton, R. G., Lucatello, S., Catanzaro, G., & Leone, F. 2012, A&A, 538, A18

Bellazzini, M., Correnti, M., Ferraro, F. R., Monaco, L., & Montegriffo, P. 2006a, A&A, 446, L1

Bellazzini, M., Ferraro, F. R., & Ibata, R. 2003, AJ, 125, 188

Bellazzini, M., Newberg, H. J., Correnti, M., Ferraro, F. R., & Monaco, L. 2006b, A&A, 457, L21

Bellazzini, M., Ibata, R. A., Chapman, S. C., Mackey, A. D., Monaco, L., Irwin, M. J., Martin, N. F., Lewis, G. F., & Dalessandro, E. 2008, AJ, 136, 1147

Bellini, A., Bianchini, P., Varri, A. L., Anderson, J., Piotto, G., van der Marel, R. P., Vesperini, E., & Watkins, L. L. 2017a, ApJ, 844, 167

Bellini, A., Milone, A. P., Anderson, J., Marino, A. F., Piotto, G., van der Marel, R. P., Bedin, L. R., & King, I. R. 2017b, ApJ, 844, 164

Bellini, A., Libralato, M., Bedin, L. R., Milone, A. P., van der Marel, R. P., Anderson, J., Apai, D., Burgasser, A. J., Marino, A. F., & Rees, J. M. 2018, ApJ, 853, 86

Belokurov, V., Zucker, D. B., Evans, N. W., et al. 2006, ApJ, 642, L137

Belokurov, V., Koposov, S. E., Evans, N. W., Peñarrubia, J., Irwin, M. J., Smith, M. C., Lewis, G. F., Gieles, M., Wilkinson, M. I., Gilmore, G., Olszewski, E. W., & Niederste-Ostholt, M. 2014, MNRAS, 437, 116

Bernard, E. J., Ferguson, A. M. N., Schlafly, E. F., et al. 2016, MNRAS, 463, 1759

Bianchini, P., Sills, A., & Miholics, M. 2017, MNRAS, 471, 1181

Bianchini, P., van de Ven, G., Norris, M. A., Schinnerer, E., & Varri, A. L. 2016, MNRAS, 458, 3644

Bianchini, P., van der Marel, R. P., del Pino, A., Watkins, L. L., Bellini, A., Fardal, M. A., Libralato, M., & Sills, A. 2018, MNRAS, 481, 2125

Bianchini, P., Varri, A. L., Bertin, G., & Zocchi, A. 2013, ApJ, 772, 67

Binney, J. 2005, MNRAS, 363, 937

Binney, J., & Mamon, G. A. 1982, MNRAS, 200, 361

Boecker, A., Leaman, R., van de Ven, G., Norris, M. A., Mackereth, T., & Crain, R. A. 2019, arXiv e-prints, arXiv:1903.11089

Böker, T. 2008, ApJ, 672, L111

Böker, T. 2010, in IAU Symposium, Vol. 266, Star Clusters: Basic Galactic Building Blocks Throughout Time and Space, ed. R. de Grijs & J. R. D. Lépine, 58

Böker, T., Laine, S., van der Marel, R. P., Sarzi, M., Rix, H.-W., Ho, L. C., & Shields, J. C. 2002, AJ, 123, 1389

Böker, T., Sarzi, M., McLaughlin, D. E., van der Marel, R. P., Rix, H.-W., Ho, L. C., & Shields, J. C. 2004, AJ, 127, 105

Bonaca, A., Hogg, D. W., Price-Whelan, A. M., & Conroy, C. 2018, arXiv e-prints, arXiv:1811.03631

Bovy, J., Bahmanyar, A., Fritz, T. K., & Kallivayalil, N. 2016, The Astrophysical Journal, 833, 31

Brodie, J. P., Romanowsky, A. J., Strader, J., & Forbes, D. A. 2011, AJ, 142, 199

Brodie, J. P., & Strader, J. 2006, Annual Review of Astronomy and Astrophysics, 44, 193

Brown, J. A., Wallerstein, G., & Gonzalez, G. 1999, AJ, 118, 1245

Brüns, R. C., Kroupa, P., Fellhauer, M., Metz, M., & Assmann, P. 2011, A&A, 529, A138

Cappellari, M. 2002, MNRAS, 333, 400

—. 2008, MNRAS, 390, 71

Cappellari, M., Verolme, E. K., van der Marel, R. P., Verdoes Kleijn, G. A., Illingworth, G. D., Franx, M., Carollo, C. M., & de Zeeuw, P. T. 2002, ApJ, 578, 787

Cappellari, M., Emsellem, E., Bacon, R., Bureau, M., Davies, R. L., de Zeeuw, P. T., Falcón-Barroso, J., Krajnović, D., Kuntschner, H., McDermid, R. M., Peletier, R. F., Sarzi, M., van den Bosch, R. C. E., & van de Ven, G. 2007, MNRAS, 379, 418

Carballo-Bello, J. A. 2019, arXiv e-prints, arXiv:1904.02177 [astro-ph.SR]

Carlin, J. L., Majewski, S. R., Casetti-Dinescu, D. I., Law, D. R., Girard, T. M., & Patterson, R. J. 2012, ApJ, 744, 25

Carollo, C. M., Stiavelli, M., & Mack, J. 1998, AJ, 116, 68

Carraro, G., Zinn, R., & Moni Bidin, C. 2007, A&A, 466, 181

Carrera, R., Pancino, E., Gallart, C., & del Pino, A. 2013, MNRAS, 434, 1681

Carretta, E., Bragaglia, A., Gratton, R., & Lucatello, S. 2009a, A&A, 505, 139

Carretta, E., Bragaglia, A., Gratton, R. G., Recio-Blanco, A., Lucatello, S., D'Orazi, V., & Cassisi, S. 2010a, A&A, 516, A55

Carretta, E., Bragaglia, A., Gratton, R. G., Lucatello, S., Catanzaro, G., Leone, F., Bellazzini, M., Claudi, R., D'Orazi, V., Momany, Y., Ortolani, S., Pancino, E., Piotto, G., Recio-Blanco, A., & Sabbi, E. 2009b, A&A, 505, 117

Carretta, E., Bragaglia, A., Gratton, R. G., Lucatello, S., Bellazzini, M., Catanzaro, G., Leone, F., Momany, Y., Piotto, G., & D'Orazi, V. 2010b, A&A, 520, A95

—. 2010c, ApJ, 714, L7

Carson, D. J., Barth, A. J., Seth, A. C., den Brok, M., Cappellari, M., Greene, J. E., Ho, L. C., & Neumayer, N. 2015, AJ, 149, 170

Chatzopoulos, S., Fritz, T. K., Gerhard, O., Gillessen, S., Wegg, C., Genzel, R., & Pfuhl, O. 2015, MNRAS, 447, 948

Chen, C. W., & Chen, W. P. 2010, ApJ, 721, 1790

Chiboucas, K., Karachentsev, I. D., & Tully, R. B. 2009, AJ, 137, 3009

Colucci, J. E., Bernstein, R. A., & Cohen, J. G. 2014, ApJ, 797, 116

Cordero, M. J., Hénault-Brunet, V., Pilachowski, C. A., Balbinot, E., Johnson, C. I., & Varri, A. L. 2017, MNRAS, 465, 3515

Côté, P., Piatek, S., Ferrarese, L., Jordán, A., Merritt, D., Peng, E. W., Haşegan, M., Blakeslee, J. P., Mei, S., West, M. J., Milosavljević, M., & Tonry, J. L. 2006, ApJ, 165, 57

Da Costa, G. S. 2016, in IAU Symposium, Vol. 317, The General Assembly of Galaxy Halos: Structure, Origin and Evolution, ed. A. Bragaglia, M. Arnaboldi, M. Rejkuba, & D. Romano, 110

Da Costa, G. S., & Armandroff, T. E. 1995, AJ, 109, 2533

de Boer, T. J. L., Belokurov, V., & Koposov, S. 2015, MNRAS, 451, 3489

den Brok, M., van de Ven, G., van den Bosch, R., & Watkins, L. 2014a, MNRAS, 438, 487

den Brok, M., Peletier, R. F., Seth, A., et al. 2014b, MNRAS, 445, 2385

Di Matteo, P., Lehnert, M. D., Qu, Y., & van Driel, W. 2011, A&A, 525, L3

Do, T., Lu, J. R., Ghez, A. M., Morris, M. R., Yelda, S., Martinez, G. D., Wright, S. A., & Matthews, K. 2013, The Astrophysical Journal, 764, 154

Dotter, A., Chaboyer, B., Jevremović, D., Kostov, V., Baron, E., & Ferguson, J. W. 2008, ApJ, 178, 89

Dressler, A. 1980, ApJ, 236, 351

Drinkwater, M. J., Gregg, M. D., Couch, W. J., Ferguson, H. C., Hilker, M., Jones, J. B., Karick, A., & Phillipps, S. 2004, , 21, 375

Drinkwater, M. J., Jones, J. B., Gregg, M. D., & Phillipps, S. 2000, , 17, 227

Drlica-Wagner, A., Bechtol, K., Allam, S., et al. 2016, ApJ, 833, L5

Duffau, S., Zinn, R., Vivas, A. K., Carraro, G., Méndez, R. A., Winnick, R., & Gallart, C. 2006, ApJ, 636, L97

Emsellem, E., Monnet, G., & Bacon, R. 1994, A&A, 285, 723

Emsellem, E., Renaud, F., Bournaud, F., Elmegreen, B., Combes, F., & Gabor, J. M. 2015, MNRAS, 446, 2468

Emsellem, E., Cappellari, M., Krajnović, D., et al. 2011, MNRAS, 414, 888

Erwin, P., & Gadotti, D. A. 2012, Advances in Astronomy, 2012, 946368

Eyre, A., & Binney, J. 2009, MNRAS, 400, 548

Fabricius, M. H., Noyola, E., Rukdee, S., Saglia, R. P., Bender, R., Hopp, U., Thomas, J., Opitsch, M., & Williams, M. J. 2014, ApJ, 787, L26

Fakhouri, O., & Ma, C.-P. 2008, MNRAS, 386, 577

Fardal, M. A., van der Marel, R. P., Sohn, S. T., & del Pino Molina, A. 2019, MNRAS, 486, 936

Feldmeier, A., Neumayer, N., Seth, A., Schödel, R., Lützgendorf, N., de Zeeuw, P. T., Kissler-Patig, M., Nishiyama, S., & Walcher, C. J. 2014, A&A, 570, A2

Feldmeier-Krause, A., Kerzendorf, W., Neumayer, N., Schödel, R., Nogueras-Lara, F., Do, T., de Zeeuw, P. T., & Kuntschner, H. 2017a, MNRAS, 464, 194

Feldmeier-Krause, A., Zhu, L., Neumayer, N., van de Ven, G., de Zeeuw, P. T., & Schödel, R. 2017b, MNRAS, 466, 4040

Feldmeier-Krause, A., Neumayer, N., Schödel, R., Seth, A., Hilker, M., de Zeeuw, P. T., Kuntschner, H., Walcher, C. J., Lützgendorf, N., & Kissler-Patig, M. 2015, A&A, 584, A2

Fellhauer, M., Belokurov, V., Evans, N. W., Wilkinson, M. I., Zucker, D. B., Gilmore, G., Irwin, M. J., Bramich, D. M., Vidrih, S., Wyse, R. F. G., Beers, T. C., & Brinkmann, J. 2006, ApJ, 651, 167

Ferrarese, L., & Merritt, D. 2000, ApJ, 539, L9

Ferrarese, L., Côté, P., Dalla Bontà, E., Peng, E. W., Merritt, D., Jordán, A., Blakeslee, J. P., Haşegan, M., Mei, S., Piatek, S., Tonry, J. L., & West, M. J. 2006, ApJ, 644, L21

Ferraro, F. R., Massari, D., Dalessandro, E., Lanzoni, B., Origlia, L., Rich, R. M., & Mucciarelli, A. 2016, ApJ, 828, 75

Ferraro, F. R., Mucciarelli, A., Lanzoni, B., Pallanca, C., Lapenna, E., Origlia, L., Dalessandro, E., Valenti, E., Beccari, G., Bellazzini, M., Vesperini, E., Varri, A., & Sollima, A. 2018, ApJ, 860, 50

Filippenko, A. V., & Ho, L. C. 2003, ApJ, 588, L13

Forbes, D. A., & Bridges, T. 2010, MNRAS, 404, 1203

Foreman-Mackey, D., Hogg, D. W., Lang, D., & Goodman, J. 2013, PASP, 125, 306

Fuentes-Carrera, I., Jablonka, P., Sarajedini, A., Bridges, T., Djorgovski, G., & Meylan, G. 2008, A&A, 483, 769

Gaburov, E., Harfst, S., & Portegies Zwart, S. 2009, NewA, 14, 630

Gaia Collaboration, Prusti, T., de Bruijne, J. H. J., Brown, A. G. A., Vallenari, A., Babusiaux, C., Bailer-Jones, C. A. L., Bastian, U., Biermann, M., Evans, D. W., & et al. 2016, A&A, 595, A1

Gaia Collaboration, Brown, A. G. A., Vallenari, A., et al. 2018, A&A, 616, A1

Galleti, S., Federici, L., Bellazzini, M., Fusi Pecci, F., & Macrina, S. 2004, A&A, 416, 917

García-Burillo, S., Combes, F., Usero, A., et al. 2014, A&A, 567, A125

Gavagnin, E., Mapelli, M., & Lake, G. 2016, MNRAS, 461, 1276

Gebhardt, K., Rich, R. M., & Ho, L. C. 2005, ApJ, 634, 1093

Gebhardt, K., Bender, R., Bower, G., Dressler, A., Faber, S. M., Filippenko, A. V., Green, R., Grillmair, C., Ho, L. C., Kormendy, J., Lauer, T. R., Magorrian, J., Pinkney, J., Richstone, D., & Tremaine, S. 2000, ApJ, 539, L13

Gebhardt, K., Richstone, D., Tremaine, S., Lauer, T. R., Bender, R., Bower, G., Dressler, A., Faber, S. M., Filippenko, A. V., Green, R., Grillmair, C., Ho, L. C., Kormendy, J., Magorrian, J., & Pinkney, J. 2003, ApJ, 583, 92

Genzel, R., Eisenhauer, F., & Gillessen, S. 2010, Reviews of Modern Physics, 82, 3121

Georgiev, I. Y., & Böker, T. 2014, MNRAS, 441, 3570

Georgiev, I. Y., Hilker, M., Puzia, T. H., Goudfrooij, P., & Baumgardt, H. 2009, MNRAS, 396, 1075

Georgiev, I. Y., Neumayer, N., Lützgendorf, N., Böker, T., & Leigh, N. 2016, Monthly Notices of the Royal Astronomical Society, 457, 2122

Geyer, E. H., Hopp, U., & Nelles, B. 1983, A&A, 125, 359

Gibbons, S. L. J., Belokurov, V., & Evans, N. W. 2014, MNRAS, 445, 3788

—. 2017, MNRAS, 464, 794

Girardi, L. 2016, Annual Review of Astronomy and Astrophysics, 54, 95

Goodman, J., & Weare, J. 2010, Communications in Applied Mathematics and Computational Science, Vol. 5, No. 1, p. 65-80, 2010, 5, 65

Graham, A. W. 2012, MNRAS, 422, 1586

Graham, A. W., Erwin, P., Caon, N., & Trujillo, I. 2001, ApJ, 563, L11

Graham, A. W., & Spitler, L. R. 2009, MNRAS, 397, 2148

Grcevich, J., & Putman, M. E. 2009, ApJ, 696, 385

Grebel, E. K., Gallagher, III, J. S., & Harbeck, D. 2003, AJ, 125, 1926

Grillmair, C. J. 2009, ApJ, 693, 1118

Grillmair, C. J., & Dionatos, O. 2006, ApJ, 641, L37

Guillard, N., Emsellem, E., & Renaud, F. 2016, MNRAS, 461, 3620

Harfst, S., Gualandris, A., Merritt, D., Spurzem, R., Portegies Zwart, S., & Berczik, P. 2007, NewA, 12, 357

Häring, N., & Rix, H.-W. 2004, ApJ, 604, L89

Harris, W. E. 1996, VizieR Online Data Catalog, 7195

Hartmann, M., Debattista, V. P., Seth, A., Cappellari, M., & Quinn, T. R. 2011, MNRAS, 418, 2697

Hasselquist, S., Shetrone, M., Smith, V., et al. 2017, ApJ, 845, 162

Hasselquist, S., Carlin, J. L., Holtzman, J. A., et al. 2019, ApJ, 872, 58

Helmi, A., & White, S. D. M. 2001, MNRAS, 323, 529

Hénault-Brunet, V., Gieles, M., Agertz, O., & Read, J. I. 2015, MNRAS, 450, 1164

Hilker, M., Infante, L., Vieira, G., Kissler-Patig, M., & Richtler, T. 1999, A&A Supp., 134, 75

Hilker, M., Kayser, A., Richtler, T., & Willemsen, P. 2004, A&A, 422, L9

Hollyhead, K., Kacharov, N., Lardo, C., Bastian, N., Hilker, M., Rejkuba, M., Koch, A., Grebel, E. K., & Georgiev, I. 2017, MNRAS, 465, L39

Hollyhead, K., Lardo, C., Kacharov, N., Bastian, N., Hilker, M., Rejkuba, M., Koch, A., Grebel, E. K., & Georgiev, I. 2018, MNRAS, 476, 114

Hollyhead, K., Martocchia, S., Lardo, C., Bastian, N., Kacharov, N., Niederhofer, F., Cabrera-Ziri, I., Dalessandro, E., Mucciarelli, A., Salaris, M., & Usher, C. 2019, MNRAS, 484, 4718

Hopkins, P. F., Bundy, K., Croton, D., Hernquist, L., Keres, D., Khochfar, S., Stewart, K., Wetzel, A., & Younger, J. D. 2010, ApJ, 715, 202

Hubble, E. P. 1936, Realm of the Nebulae

Husser, T.-O., Kamann, S., Dreizler, S., Wendt, M., Wulff, N., Bacon, R., Wisotzki, L., Brinchmann, J., Weilbacher, P. M., Roth, M. M., & Monreal-Ibero, A. 2016, A&A, 588, A148

Ibata, R., Bellazzini, M., Malhan, K., Martin, N., & Bianchini, P. 2019a, arXiv e-prints, arXiv:1902.09544

Ibata, R., Irwin, M., Lewis, G., Ferguson, A. M. N., & Tanvir, N. 2001a, Nature, 412, 49

Ibata, R., Lewis, G. F., Irwin, M., Totten, E., & Quinn, T. 2001b, ApJ, 551, 294

Ibata, R., Bellazzini, M., Chapman, S. C., Dalessandro, E., Ferraro, F., Irwin, M., Lanzoni, B., Lewis, G. F., Mackey, A. D., Miocchi, P., & Varghese, A. 2009, ApJ, 699, L169

Ibata, R. A., Gilmore, G., & Irwin, M. J. 1994, Nature, 370, 194

Ibata, R. A., Lewis, G. F., Irwin, M. J., & Quinn, T. 2002, MNRAS, 332, 915

Ibata, R. A., Malhan, K., & Martin, N. F. 2019b, ApJ, 872, 152

Ibata, R. A., Wyse, R. F. G., Gilmore, G., Irwin, M. J., & Suntzeff, N. B. 1997, AJ, 113, 634

Jalali, B., Baumgardt, H., Kissler-Patig, M., Gebhardt, K., Noyola, E., Lützgendorf, N., & de Zeeuw, P. T. 2012, A&A, 538, A19

Jindal, A., Webb, J. J., & Bovy, J. 2019, arXiv e-prints, arXiv:1903.11070

Johnson, C. I., & Pilachowski, C. A. 2010, ApJ, 722, 1373

Johnston, K. V., Zhao, H., Spergel, D. N., & Hernquist, L. 1999, ApJ, 512, L109

Kacharov, N., Neumayer, N., Seth, A. C., Cappellari, M., McDermid, R., Walcher, C. J., & Böker, T. 2018, MNRAS, 480, 1973

Kacharov, N., Bianchini, P., Koch, A., Frank, M. J., Martin, N. F., van de Ven, G., Puzia, T. H., McDonald, I., Johnson, C. I., & Zijlstra, A. A. 2014, A&A, 567, A69

Kamann, S., Wisotzki, L., & Roth, M. M. 2013, A&A, 549, A71

Kamann, S., Husser, T.-O., Dreizler, S., Emsellem, E., Weilbacher, P. M., Martens, S., Bacon, R., den Brok, M., Giesers, B., Krajnović, D., Roth, M. M., Wendt, M., & Wisotzki, L. 2018, MNRAS, 473, 5591

Katz, N. 1991, ApJ, 368, 325

Kazantzidis, S., Łokas, E. L., Callegari, S., Mayer, L., & Moustakas, L. A. 2011, ApJ, 726, 98

Kazantzidis, S., Mayer, L., Callegari, S., Dotti, M., & Moustakas, L. A. 2017, ApJ, 836, L13

Khoperskov, S., Mastrobuono-Battisti, A., Di Matteo, P., & Haywood, M. 2018, A&A, 620, A154

Kimmig, B., Seth, A., Ivans, I. I., Strader, J., Caldwell, N., Anderton, T., & Gregersen, D. 2015, AJ, 149, 53

King, I. R. 1966, AJ, 71, 64

Kirby, E. N., Cohen, J. G., Guhathakurta, P., Cheng, L., Bullock, J. S., & Gallazzi, A. 2013, ApJ, 779, 102

Koch, A., Hanke, M., & Kacharov, N. 2018, A&A, 616, A74

Koleva, M., Prugniel, P., Bouchard, A., & Wu, Y. 2009, A&A, 501, 1269

Koposov, S. E., Rix, H.-W., & Hogg, D. W. 2010, ApJ, 712, 260

Koposov, S. E., Belokurov, V., Evans, N. W., Gilmore, G., Gieles, M., Irwin, M. J., Lewis, G. F., Niederste-Ostholt, M., Peñarrubia, J., Smith, M. C., Bizyaev, D., Malanushenko, E., Malanushenko, V., Schneider, D. P., & Wyse, R. F. G. 2012, ApJ, 750, 80

Koposov, S. E., Walker, M. G., Belokurov, V., Casey, A. R., Geringer-Sameth, A., Mackey, D., Da Costa, G., Erkal, D., Jethwa, P., Mateo, M., Olszewski, E. W., & Bailey, J. I. 2018, MNRAS, 479, 5343

Koposov, S. E., Belokurov, V., Li, T. S., et al. 2019, MNRAS, 485, 4726

Kormendy, J., & Bender, R. 2012, ApJ, 198, 2

Kormendy, J., & Richstone, D. 1995, Annual Review of Astronomy and Astrophysics, 33, 581

Kruijssen, J. M. D., Pfeffer, J. L., Reina-Campos, M., Crain, R. A., & Bastian, N. 2018, MNRAS, arXiv:1806.05680

Kundu, A., & Whitmore, B. C. 2001, AJ, 122, 1251

Lagos, C. d. P., Stevens, A. R. H., Bower, R. G., Davis, T. A., Contreras, S., Padilla, N. D., Obreschkow, D., Croton, D., Trayford, J. W., Welker, C., & Theuns, T. 2018, MNRAS, 473, 4956

Laporte, C. F. P., Minchev, I., Johnston, K. V., & Gómez, F. A. 2019, MNRAS, 485, 3134

Lardo, C., Salaris, M., Bastian, N., Mucciarelli, A., Dalessandro, E., & Cabrera-Ziri, I. 2018, A&A, 616, A168

Lardo, C., Pancino, E., Bellazzini, M., et al. 2015, A&A, 573, A115

Law, D. R., & Majewski, S. R. 2010a, ApJ, 718, 1128

—. 2010b, ApJ, 714, 229

Law, D. R., & Majewski, S. R. 2016, The Sagittarius Dwarf Tidal Stream(s), ed. H. J. Newberg & J. L. Carlin (Cham: Springer International Publishing), 31

Layden, A. C., & Sarajedini, A. 2000, AJ, 119, 1760

Leaman, R., VandenBerg, D. A., & Mendel, J. T. 2013, MNRAS, 436, 122

Lee, Y.-W., Joo, J.-M., Sohn, Y.-J., Rey, S.-C., Lee, H.-C., & Walker, A. R. 1999, Nature, 402, 55

Leon, S., Meylan, G., & Combes, F. 2000, A&A, 359, 907

Li, Y.-S., & Helmi, A. 2008, MNRAS, 385, 1365

Lindegren, L., Hernández, J., Bombrun, A., et al. 2018, A&A, 616, A2

Lu, J. R., Do, T., Ghez, A. M., Morris, M. R., Yelda, S., & Matthews, K. 2013, The Astrophysical Journal, 764, 155

Lützgendorf, N., Kissler-Patig, M., Noyola, E., Jalali, B., de Zeeuw, P. T., Gebhardt, K., & Baumgardt, H. 2011, A&A, 533, A36

Lützgendorf, N., Kissler-Patig, M., Neumayer, N., Baumgardt, H., Noyola, E., de Zeeuw, P. T., Gebhardt, K., Jalali, B., & Feldmeier, A. 2013, A&A, 555, A26

Lynden-Bell, D. 1967, MNRAS, 136, 101

Lynden-Bell, D., & Lynden-Bell, R. M. 1995, Monthly Notices of the Royal Astronomical Society, 275, 429

Lyubenova, M., van den Bosch, R. C. E., Côté, P., Kuntschner, H., van de Ven, G., Ferrarese, L., Jordán, A., Infante, L., & Peng, E. W. 2013, Monthly Notices of the Royal Astronomical Society, 431, 3364

Mackey, A. D., Da Costa, G. S., Ferguson, A. M. N., & Yong, D. 2013, ApJ, 762, 65

Majewski, S. R., Patterson, R. J., Dinescu, D. I., Johnson, W. Y., Ostheimer, J. C., Kunkel, W. E., & Palma, C. 2000, in Liege International Astrophysical Colloquia, Vol. 35, Liege International Astrophysical Colloquia, ed. A. Noels, P. Magain, D. Caro, E. Jehin, G. Parmentier, & A. A. Thoul, 619

Majewski, S. R., Skrutskie, M. F., Weinberg, M. D., & Ostheimer, J. C. 2003, ApJ, 599, 1082

Malhan, K., Ibata, R. A., & Martin, N. F. 2018, MNRAS, 481, 3442

Mapelli, M., Ripamonti, E., Battaglia, G., Tolstoy, E., Irwin, M. J., Moore, B., & Sigurdsson, S. 2009, MNRAS, 396, 1771

Mapelli, M., Ripamonti, E., Tolstoy, E., Sigurdsson, S., Irwin, M. J., & Battaglia, G. 2007, MNRAS, 380, 1127

Marín-Franch, A., Aparicio, A., Piotto, G., et al. 2009, ApJ, 694, 1498

Martin, N. F., Nidever, D. L., Besla, G., et al. 2015, The Astrophysical Journal, 804, L5

Martínez-Delgado, D., Peñarrubia, J., Jurić, M., Alfaro, E. J., & Ivezić, Z. 2007, ApJ, 660, 1264

Martocchia, S., Bastian, N., Usher, C., et al. 2017, MNRAS, 468, 3150

Martocchia, S., Cabrera-Ziri, I., Lardo, C., et al. 2018, MNRAS, 473, 2688

Massari, D., Mucciarelli, A., Ferraro, F. R., Origlia, L., Rich, R. M., Lanzoni, B., Dalessandro, E., Valenti, E., Ibata, R., Lovisi, L., Bellazzini, M., & Reitzel, D. 2014, ApJ, 795, 22

Mastrobuono-Battisti, A., Khoperskov, S., Di Matteo, P., & Haywood, M. 2019, A&A, 622, A86

Mastrobuono-Battisti, A., & Perets, H. B. 2013, ApJ, 779, 85

—. 2016, ApJ, 823, 61

Mastropietro, C., Moore, B., Mayer, L., Debattista, V. P., Piffaretti, R., & Stadel, J. 2005, MNRAS, 364, 607

Mateo, M. L. 1998, Annual Review of Astronomy and Astrophysics, 36, 435

Mateu, C., Read, J. I., & Kawata, D. 2017, Monthly Notices of the Royal Astronomical Society, 474, 4112

Mayer, L., Governato, F., Colpi, M., Moore, B., Quinn, T., Wadsley, J., Stadel, J., & Lake, G. 2001a, ApJ, 559, 754

—. 2001b, ApJ, 547, L123

Mayer, L., Kazantzidis, S., Mastropietro, C., & Wadsley, J. 2007, Nature, 445, 738

Mayer, L., Mastropietro, C., Wadsley, J., Stadel, J., & Moore, B. 2006, MNRAS, 369, 1021

Mayer, L., Moore, B., Quinn, T., Governato, F., & Stadel, J. 2002, MNRAS, 336, 119

McConnachie, A. W. 2012, AJ, 144, 4

Mészáros, S., Martell, S. L., Shetrone, M., et al. 2015, The Astronomical Journal, 149, 153

Meylan, G. 1987, A&A, 184, 144

Meylan, G., & Mayor, M. 1986, A&A, 166, 122

Meylan, G., Sarajedini, A., Jablonka, P., Djorgovski, S. G., Bridges, T., & Rich, R. M. 2001, AJ, 122, 830

Mieske, S., Frank, M. J., Baumgardt, H., Lützgendorf, N., Neumayer, N., & Hilker, M. 2013, A&A, 558, A14

Mieske, S., Hilker, M., & Infante, L. 2004, A&A, 418, 445

Mieske, S., Hilker, M., & Misgeld, I. 2012, A&A, 537, A3

Miholics, M., Webb, J. J., & Sills, A. 2014, MNRAS, 445, 2872

—. 2016, MNRAS, 456, 240

Mihos, J. C., & Hernquist, L. 1994, ApJ, 425, L13

—. 1996, ApJ, 464, 641

Milone, A. P. 2015, MNRAS, 446, 1672

Milone, A. P., Marino, A. F., Bedin, L. R., Anderson, J., Apai, D., Bellini, A., Bergeron, P., Burgasser, A. J., Dotter, A., & Rees, J. M. 2017a, MNRAS, 469, 800

Milone, A. P., Piotto, G., Renzini, A., et al. 2017b, MNRAS, 464, 3636

Milone, A. P., Marino, A. F., Renzini, A., et al. 2018, MNRAS, 481, 5098

Milosavljević, M. 2004, ApJ, 605, L13

Minniti, D., Kissler-Patig, M., Goudfrooij, P., & Meylan, G. 1998, The Astronomical Journal, 115, 121

Misgeld, I., & Hilker, M. 2011, MNRAS, 414, 3699

Momany, Y., Held, E. V., Saviane, I., Zaggia, S., Rizzi, L., & Gullieuszik, M. 2007, A&A, 468, 973

Monaco, L., Bellazzini, M., Bonifacio, P., Buzzoni, A., Ferraro, F. R., Marconi, G., Sbordone, L., & Zaggia, S. 2007, A&A, 464, 201

Monaco, L., Bellazzini, M., Bonifacio, P., Ferraro, F. R., Marconi, G., Pancino, E., Sbordone, L., & Zaggia, S. 2005a, A&A, 441, 141

Monaco, L., Bellazzini, M., Ferraro, F. R., & Pancino, E. 2004, MNRAS, 353, 874

—. 2005b, MNRAS, 356, 1396

Monaco, L., Ferraro, F. R., Bellazzini, M., & Pancino, E. 2002, ApJ, 578, L47

Muñoz, R. P., Eigenthaler, P., Puzia, T. H., et al. 2015, ApJ, 813, L15

Mucciarelli, A., Bellazzini, M., Ibata, R., Romano, D., Chapman, S. C., & Monaco, L. 2017, A&A, 605, A46

Mucciarelli, A., Dalessandro, E., Ferraro, F. R., Origlia, L., & Lanzoni, B. 2014, ApJ, 793, L6

Mucciarelli, A., Lapenna, E., Ferraro, F. R., & Lanzoni, B. 2018, ApJ, 859, 75

Mucciarelli, A., Origlia, L., Ferraro, F. R., & Pancino, E. 2009, ApJ, 695, L134

Murray, N. 2009, ApJ, 691, 946

Nardiello, D., Piotto, G., Milone, A. P., Rich, R. M., Cassisi, S., Bedin, L. R., Bellini, A., & Renzini, A. 2019, MNRAS, 485, 3076

Neumayer, N., & Walcher, C. J. 2012, Advances in Astronomy, 2012, 709038

Neumayer, N., Walcher, C. J., Andersen, D., Sánchez, S. F., Böker, T., & Rix, H.-W. 2011, MNRAS, 413, 1875

Newberg, H. J., Yanny, B., Rockosi, C., et al. 2002, ApJ, 569, 245

Nguyen, D. D., Seth, A. C., den Brok, M., Neumayer, N., Cappellari, M., Barth, A. J., Caldwell, N., Williams, B. F., & Binder, B. 2017, ApJ, 836, 237

Nguyen, D. D., Seth, A. C., Neumayer, N., Kamann, S., Voggel, K. T., Cappellari, M., Picotti, A., Nguyen, P. M., Böker, T., Debattista, V., Caldwell, N., McDermid, R., Bastian, N., Ahn, C. C., & Pechetti, R. 2018, ApJ, 858, 118

Niederhofer, F., Bastian, N., Kozhurina-Platais, V., et al. 2017a, MNRAS, 464, 94

—. 2017b, MNRAS, 465, 4159

Niederste-Ostholt, M., Belokurov, V., & Evans, N. W. 2012, MNRAS, 422, 207

Norris, M. A., Escudero, C. G., Faifer, F. R., Kannappan, S. J., Forte, J. C., & van den Bosch, R. C. E. 2015, MNRAS, 451, 3615

Norris, M. A., Kannappan, S. J., Forbes, D. A., et al. 2014, MNRAS, 443, 1151

Noyola, E., & Gebhardt, K. 2006, AJ, 132, 447

Noyola, E., Gebhardt, K., & Bergmann, M. 2008, ApJ, 676, 1008

Odenkirchen, M., Grebel, E. K., Rockosi, C. M., et al. 2001, The Astrophysical Journal, 548, L165

Ordenes-Briceño, Y., Puzia, T. H., Eigenthaler, P., et al. 2018, ApJ, 860, 4

Origlia, L., Mucciarelli, A., Fiorentino, G., Ferraro, F. R., Dalessandro, E., Lanzoni, B., Rich, R. M., Massari, D., Contreras Ramos, R., & Matsunaga, N. 2019, ApJ, 871, 114

Pancino, E., Romano, D., Tang, B., et al. 2017, A&A, 601, A112

Peñarrubia, J., Benson, A. J., Walker, M. G., Gilmore, G., McConnachie, A. W., & Mayer, L. 2010, MNRAS, 406, 1290

Peng, E. W., Jordán, A., Côté, P., Blakeslee, J. P., Ferrarese, L., Mei, S., West, M. J., Merritt, D., Milosavljević, M., & Tonry, J. L. 2006, ApJ, 639, 95

Pfeffer, J., & Baumgardt, H. 2013, MNRAS, 433, 1997

Pfeffer, J., Griffen, B. F., Baumgardt, H., & Hilker, M. 2014, MNRAS, 444, 3670

Pfeffer, J., Hilker, M., Baumgardt, H., & Griffen, B. F. 2016, MNRAS, 458, 2492

Phillips, A. C., Illingworth, G. D., MacKenty, J. W., & Franx, M. 1996, AJ, 111, 1566

Piotto, G., Milone, A. P., Bedin, L. R., et al. 2015, The Astronomical Journal, 149, 91

Plummer, H. C. 1911, MNRAS, 71, 460

Pont, F., & Eyer, L. 2004, MNRAS, 351, 487

Price, J., Phillipps, S., Huxor, A., et al. 2009, MNRAS, 397, 1816

Qu, Y., Di Matteo, P., Lehnert, M. D., van Driel, W., & Jog, C. J. 2011, A&A, 535, A5

Renaud, F., Bournaud, F., & Duc, P.-A. 2015, MNRAS, 446, 2038

Rix, H.-W., de Zeeuw, P. T., Cretton, N., van der Marel, R. P., & Carollo, C. M. 1997, ApJ, 488, 702

Roberts, Jr., W. W., Huntley, J. M., & van Albada, G. D. 1979, ApJ, 233, 67

Robin, A. C., Reylé, C., Derrière, S., & Picaud, S. 2003, A&A, 409, 523

Rossa, J., van der Marel, R. P., Böker, T., Gerssen, J., Ho, L. C., Rix, H.-W., Shields, J. C., & Walcher, C.-J. 2006, AJ, 132, 1074

Sakari, C. M., Venn, K. A., Mackey, D., Shetrone, M. D., Dotter, A., Ferguson, A. M. N., & Huxor, A. 2015, MNRAS, 448, 1314

Sánchez-Janssen, R., Côté, P., Ferrarese, L., et al. 2018, arXiv e-prints, arXiv:1812.01019

Sarajedini, A., Bedin, L. R., Chaboyer, B., Dotter, A., Siegel, M., Anderson, J., Aparicio, A., King, I., Majewski, S., Marín-Franch, A., Piotto, G., Reid, I. N., & Rosenberg, A. 2007, AJ, 133, 1658

Savorgnan, G. A. D., Graham, A. W., Marconi, A., & Sani, E. 2016, ApJ, 817, 21

Schlafly, E. F., & Finkbeiner, D. P. 2011, ApJ, 737, 103

Schlegel, D. J., Finkbeiner, D. P., & Davis, M. 1998, ApJ, 500, 525

Schödel, R., Feldmeier, A., Kunneriath, D., Stolovy, S., Neumayer, N., Amaro-Seoane, P., & Nishiyama, S. 2014a, A&A, 566, A47

Schödel, R., Feldmeier, A., Neumayer, N., Meyer, L., & Yelda, S. 2014b, Classical and Quantum Gravity, 31, 244007

Schödel, R., Merritt, D., & Eckart, A. 2009, A&A, 502, 91

Schödel, R., Eckart, A., Alexander, T., Merritt, D., Genzel, R., Sternberg, A., Meyer, L., Kul, F., Moultaka, J., Ott, T., & Straubmeier, C. 2007, A&A, 469, 125

Schwarzschild, M. 1979, ApJ, 232, 236

Scott, N., & Graham, A. W. 2013, ApJ, 763, 76

Seth, A., Agüeros, M., Lee, D., & Basu-Zych, A. 2008, ApJ, 678, 116

Seth, A. C., Dalcanton, J. J., Hodge, P. W., & Debattista, V. P. 2006, AJ, 132, 2539

Seth, A. C., van den Bosch, R., Mieske, S., Baumgardt, H., Brok, M. D., Strader, J., Neumayer, N., Chilingarian, I., Hilker, M., McDermid, R., Spitler, L., Brodie, J., Frank, M. J., & Walsh, J. L. 2014, Nature, 513, 398

Shipp, N., Drlica-Wagner, A., Balbinot, E., et al. 2018, ApJ, 862, 114

Siegel, M. H., Dotter, A., Majewski, S. R., Sarajedini, A., Chaboyer, B., Nidever, D. L., Anderson, J., Marín-Franch, A., Rosenberg, A., Bedin, L. R., Aparicio, A., King, I., Piotto, G., & Reid, I. N. 2007, ApJ, 667, L57

Siegel, M. H., Majewski, S. R., Law, D. R., et al. 2011, ApJ, 743, 20

Simon, J. D. 2019, arXiv e-prints, arXiv:1901.05465

Smith, R., Davies, J. I., & Nelson, A. H. 2010, MNRAS, 405, 1723

Sohn, S. T., van der Marel, R. P., Carlin, J. L., Majewski, S. R., Kallivayalil, N., Law, D. R., Anderson, J., & Siegel, M. H. 2015, ApJ, 803, 56

Sollima, A., Baumgardt, H., & Hilker, M. 2019, MNRAS, 485, 1460

Sollima, A., Baumgardt, H., Zocchi, A., Balbinot, E., Gieles, M., Hénault-Brunet, V., & Varri, A. L. 2015, MNRAS, 451, 2185

Sollima, A., Cacciari, C., Bellazzini, M., & Colucci, S. 2010, MNRAS, 406, 329

Springel, V., Di Matteo, T., & Hernquist, L. 2005, ApJ, 620, L79

Starkenburg, E., Hill, V., Tolstoy, E., González Hernández, J. I., Irwin, M., Helmi, A., Battaglia, G., Jablonka, P., Tafelmeyer, M., Shetrone, M., Venn, K., & de Boer, T. 2010, A&A, 513, A34

Tamura, N., Sharples, R. M., Arimoto, N., Onodera, M., Ohta, K., & Yamada, Y. 2006, MNRAS, 373, 588

Tepper-García, T., & Bland-Hawthorn, J. 2018, MNRAS, 478, 5263

Teuben, P. 1995, in Astronomical Society of the Pacific Conference Series, Vol. 77, Astronomical Data Analysis Software and Systems IV, ed. R. A. Shaw, H. E. Payne, & J. J. E. Hayes, 398

Tiongco, M. A., Vesperini, E., & Varri, A. L. 2016, MNRAS, 455, 3693

Tissera, P. B. 2000, ApJ, 534, 636

Tolstoy, E., Hill, V., & Tosi, M. 2009, Annual Review of Astronomy and Astrophysics, 47, 371

Torrealba, G., Koposov, S. E., Belokurov, V., Irwin, M., Collins, M., Spencer, M., Ibata, R., Mateo, M., Bonaca, A., & Jethwa, P. 2016, MNRAS, 463, 712

Torrealba, G., Belokurov, V., Koposov, S. E., et al. 2018a, MNRAS, 475, 5085

Torrealba, G., Belokurov, V., Koposov, S. E., Li, T. S., Walker, M. G., Sanders, J. L., Geringer-Sameth, A., Zucker, D. B., Kuehn, K., Evans, N. W., & Dehnen, W. 2018b, arXiv e-prints, arXiv:1811.04082

Totten, E. J., & Irwin, M. J. 1998, MNRAS, 294, 1

Tremaine, S. D., Ostriker, J. P., & Spitzer, Jr., L. 1975, ApJ, 196, 407

Tremonti, C. A., Heckman, T. M., Kauffmann, G., Brinchmann, J., Charlot, S., White, S. D. M., Seibert, M., Peng, E. W., Schlegel, D. J., Uomoto, A., Fukugita, M., & Brinkmann, J. 2004, ApJ, 613, 898

Tsatsi, A., Mastrobuono-Battisti, A., van de Ven, G., Perets, H. B., Bianchini, P., & Neumayer, N. 2017, MNRAS, 464, 3720

Turner, M. L., Côté, P., Ferrarese, L., Jordán, A., Blakeslee, J. P., Mei, S., Peng, E. W., & West, M. J. 2012, ApJ, 203, 5

van de Ven, G., van den Bosch, R. C. E., Verolme, E. K., & de Zeeuw, P. T. 2006, A&A, 445, 513

van der Marel, R. P., Cretton, N., de Zeeuw, P. T., & Rix, H.-W. 1998, ApJ, 493, 613

VandenBerg, D. A., Bergbusch, P. A., Dotter, A., Ferguson, J. W., Michaud, G., Richer, J., & Proffitt, C. R. 2012, ApJ, 755, 15

Varghese, A., Ibata, R., & Lewis, G. F. 2011, MNRAS, 417, 198

Vasiliev, E. 2019, MNRAS, 484, 2832

Verolme, E. K., Cappellari, M., Copin, Y., van der Marel, R. P., Bacon, R., Bureau, M., Davies, R. L., Miller, B. M., & de Zeeuw, P. T. 2002, MNRAS, 335, 517

Vesperini, E., Varri, A. L., McMillan, S. L. W., & Zepf, S. E. 2014, MNRAS, 443, L79

Villanova, S., Geisler, D., Gratton, R. G., & Cassisi, S. 2014, ApJ, 791, 107

Vincenzo, F., Matteucci, F., de Boer, T. J. L., Cignoni, M., & Tosi, M. 2016, MNRAS, 460, 2238

Voggel, K. T., Seth, A. C., Neumayer, N., Mieske, S., Chilingarian, I., Ahn, C., Baumgardt, H., Hilker, M., Nguyen, D. D., Romanowsky, A. J., Walsh, J. L., den Brok, M., & Strader, J. 2018, ApJ, 858, 20

Walcher, C. J., Böker, T., Charlot, S., Ho, L. C., Rix, H.-W., Rossa, J., Shields, J. C., & van der Marel, R. P. 2006, ApJ, 649, 692

Walcher, C. J., van der Marel, R. P., McLaughlin, D., Rix, H.-W., Böker, T., Häring, N., Ho, L. C., Sarzi, M., & Shields, J. C. 2005, ApJ, 618, 237

Walker, M. G., Mateo, M., Olszewski, E. W., Sen, B., & Woodroofe, M. 2009, AJ, 137, 3109

Walker, M. G., & Peñarrubia, J. 2011, ApJ, 742, 20

Watkins, L. L., van de Ven, G., den Brok, M., & van den Bosch, R. C. E. 2013, MNRAS, 436, 2598

Watkins, L. L., van der Marel, R. P., Bellini, A., & Anderson, J. 2015a, ApJ, 803, 29

—. 2015b, ApJ, 812, 149

Wehner, E. H., & Harris, W. E. 2006, ApJ, 644, L17

Weilbacher, P. M., Streicher, O., Urrutia, T., Pécontal-Rousset, A., Jarno, A., & Bacon, R. 2014, in Astronomical Society of the Pacific Conference Series, Vol. 485, Astronomical Data Analysis Software and Systems XXIII, ed. N. Manset & P. Forshay, 451

White, S. D. M., & Rees, M. J. 1978, MNRAS, 183, 341

Willman, B., & Strader, J. 2012, AJ, 144, 76

Wu, Y., Singh, H. P., Prugniel, P., Gupta, R., & Koleva, M. 2011, A&A, 525, A71

Zhu, L., van de Ven, G., Watkins, L. L., & Posti, L. 2016a, MNRAS, 463, 1117

Zhu, L., Romanowsky, A. J., van de Ven, G., Long, R. J., Watkins, L. L., Pota, V., Napolitano, N. R., Forbes, D. A., Brodie, J., & Foster, C. 2016b, MNRAS, 462, 4001

Zinnecker, H., Keable, C. J., Dunlop, J. S., Cannon, R. D., & Griffiths, W. K. 1988, in IAU Symposium, Vol. 126, The Harlow-Shapley Symposium on Globular Cluster Systems in Galaxies, ed. J. E. Grindlay & A. G. D. Philip, 603

Zocchi, A., Gieles, M., Hénault-Brunet, V., & Varri, A. L. 2016, MNRAS, 462, 696

Zucker, D. B., Kniazev, A. Y., Bell, E. F., et al. 2004, ApJ, 612, L117